UNIVERSITY OF CALIFORNIA

Los Angeles

Loss driven photonic materials

A dissertation submitted in partial satisfaction of the

requirements for the degree Doctor of Philosophy

in Materials Science and Engineering

by

Jin Xu

2021

ABSTRACT OF THE DISSERTATION

Loss driven photonic materials

By

Jin Xu

Doctor of Philosophy in Materials Science and Engineering

University of California, Los Angeles, 2021

Professor Aaswath Pattabhi Raman, Chair

Optical absorption driven by intrinsic material loss is often viewed as a challenge to be overcome in photonic and metamaterials-based systems. In the context of applications such as optical communication, reducing absorption remains a key goal to maximize optical transmission. However, for many other applications related to sensing and detection, as well as heat transfer and energy, absorption and emission are essential. The overarching goal of this thesis is about taking advantage and embracing the loss in materials. Sometimes we have to lose to "gain".

In Chapter 1, we leveraged the loss in the epsilon near zero (ENZ) materials to build a broadband directional thermal emitter for the first time. We introduced and experimentally realized gradient epsilon-near-zero (ENZ) materials that enable broad spectrum directional control of

thermal emission by supporting leaky electromagnetic modes that couple to free space at fixed angles over a broad bandwidth. We experimentally demonstrated two emitters consisting of multiple metal and semiconductor oxides in a photonic configuration that enable gradient ENZ behavior over long-wave infrared wavelengths. The structures exhibits high average emissivity (> 0.6 and > 0.7) in the p polarization between 7.7 and 11.5μm over an angular range of 70°-85°, and between 10.0 to 14.3μm over an angular range of 60°-75°, respectively. Outside these angular ranges, the emissivity reduces to 0.4 and lower for angles smaller than 50° and 40° respectively. The structures' broadband thermal beaming capability enables radiative heat transfer only at particular angles and is experimentally verified through direct measurements of thermal emission. By decoupling conventional limitations on angular and spectral response, our approach opens new capabilities for applications such as thermal camouflaging, solar heating, radiative cooling and waste heat recovery.

In Chapter 2, we further expanded our gradient ENZ thin film idea using doped III-V semiconductors to realize more continuous and precise control for the directional thermal radiation. Both experimentally and numerically we proved that, by increasing the total thickness of the gradient ENZ thin film made by Si-doped InAs, the high emissivity angle will move towards normal incidence. Also, by changing the doping level of the doped InAs film, we observed the functional bandwidth of the sample changes to a different range, which makes doped III-V semiconductors a more flexible directional thermal emitter candidate.

In Chapter 3, we explored the beauty of loss in photonic crystals: in particular non-Hermitian photonic crystal where two materials only have a difference in the imaginary part of the permittivity. We found counter-intuitive behavior in this under-studied class of system, including loss-driven reflection. We characterized the band structure as well as the reflection response in

both 1D and 2D non-Hermitian system. By introducing a lossy material in the crystal, a quasi-bandgap purely induced by loss opens up at the band edge. A sharp reflection peak is also observed within the quasi bandgap in both 1D and 2D non-Hermitian photonic crystals we proposed. In the end, we designed a selective reflector which consists a traditional 2D photonic crystal waveguide and a non-Hermitian photonic crystal. This selective reflector can guide light along the waveguide and have the light absorbed by the non-Hermitian part while only the light with certain wavelength can be reflected back, which distinguishes this selective reflector with the traditional reflectors such as a Bragg mirror.

Finally in Chapter 4, lossy materials such as conductive polymers can potentially enable a revolution in building energy efficiency by dynamically controlling their thermal emissivity. We proposed a mechanism to decouple the mean radiant temperature from actual temperatures of interior surfaces by dynamically tuning the thermal emissivity of interior building surfaces. We quantitatively evaluated how much impact it will have on building energy saving in a building scale thought out a whole year. We showed that in cold weather, setting the emissivity of interior surfaces to a low value (0.1) can decrease the setpoint as much as 6.5°C from a baseline of 23°C. Conversely, in warm weather, low emissivity interior surfaces result in a 4.5°C cooling setpoint decrease relative to high emissivity (0.9) surfaces. EnergyPlus calculation shows that by implementing the tunable emissivity interior, more than 30% of the cooling and heating energy can be saved year-round in different climates.

The dissertation of Jin Xu is approved.

Bruce Dunn

Qibing Pei

Chee Wei Wong

Aaswath Pattabhi Raman, Committee Chair

University of California, Los Angeles

2021

To my mom Yaoju Pei and my dad Guangyao Xu

TABLE OF CONTENTS

LIST OF FIGURES

Figure 1.4. Dispersion relation of the gradient ENZ thin films. The total thicknesses, for the red, green and blue curves, increases from 0.027 Λ to 0.15Λ and 0.45Λ respectively, where Λ is the dimensionless average wavelength. The broadband Berreman mode moves towards normal incidence as the total thickness of the gradient ENZ film increases, which agrees to the results in Figure 1.1. (d)-(f).

Figure 1.5. Real (solid) and imaginary (dashed) parts of the permittivities (a) SiO_2, SiO and Al_2O_3 in the first multilayer structure, (b) $Ta_2O_5/TiO_2/MgO$ in second, each of which shows a slowly-varying permittivity that crosses zero at complementary wavelengths in the long-wave infrared part of the spectrum.

Figure 1.6. Experimental results. (a) SEM images of the experimentally fabricated multilayer photonic film structures. (e) Polar plot of the measured average emissivity over broad wavelength ranges of operation (7.7-11.5μm and 10.0-14.3 μm respectively) varying with angle of incidence for p polarization in those two structures, with high emissivity only at angles of incidence of 70° to 85° and 60° to 75° for structure 1 and structure 2 (f) and (g) Measured emissivity of the two photonic structures varying with wavelength at 3 different angles for p-polarization. Both the photonic structures exhibit a strong contrast between emissive and reflective states as a function of angle of incidence.

Figure 1.7. Emissivity spectra varying with angle and wavelength of the two fabricated photonic structures for the s polarization. (**a**) and (**c**) Measured emissivity spectra for s-polarization, and (**b**) and (**d**) simulation results of emissivity in s-polarization using transfer matrix method. The results

show that in the s polarization, low emissivity is exhibited by both structures regardless of angle of incidence, and that experimental results match well with simulations

Figure 1.8. **Simulation and experiment results comparison.** (a) and (d) Measured emissivity spectra varying with angle and wavelength of the two fabricated photonic structures in p-polarization, and (b) and (e) simulation results of the emissivity of the two structures for p-polarization using transfer matrix method, both show a broadband angularly selective behavior in emissivity and match well with the experiment measurement. (c) and (f) Average emissivity of the two structures from both measurement and simulation varying with angle of incidence for p polarization over wavelength ranges of 7.7-11.5 μm and 10.0-14.3μm respectively.

Figure 1.9. Dispersion relation of (a) gradient ENZ structure 1 (SiO_2/SiO/Al_2O_3) and (b) structure 2 (Ta_2O_5/TiO_2/MgO)

Figure 1.10. Schematic demonstration of the radiometric measurement setup

Figure 1.11. Radiometric measurements (a) and (b) Thermal images of the fabricated SiO_2/SiO/Al_2O_3 and Ta_2O_5/TiO_2/MgO multilayer photonic thin film structure. At the angle of incidence equals 77.5° and 72.5° for the two structures respectively, the wafer appears warmer compared with the angle of incidence is at 10° and 45° even though the actual temperature of the wafers maintains the same. (c) Inferred average directional emittance by radiometrically derived

temperature measurements over the 7.5-13.5 μm detector wavelength range for the two thermal emitter structures, at different angles of incidence.

Figure 1.12. Thermal image of 5 identical fabricated wafers of structure 1 in an outdoor setting. The further the wafer is the larger the angle of incidence to the thermal camera is, which gives the farthest wafer the highest emissivity. The metal support, which is low emissivity and reflecting the sky, looks cold to the camera regardless of the angle of view

Figure 2.1. Wavelength-dependent (a) real and (b) imaginary parts of the permittivity of different doped InAs, calculated from the modeled fits of the experimental reflection data from the as-grown samples using the Drude model.

Figure 2.2 Calculated permittivity of the doped InAs: doping level range from 2.0e18 to 4.5e18cm^{-3}. (a) real part of the permittivity, (b) imaginary part of the permittivity

Figure 2.3 Schematic illustration of the gradient doped InAs film structure

Figure 2.4 Emissivity spectrum for p polarization varies with angle of incidence and wavelength of three different thickness stacks of Si doped InAs: (a) 50nm thick each layer, (b) 100nm thick each layer, (c) 150nm thick each layer.

Figure 2.11 Emissivity spectrum for p polarization varies with angle of incidence and wavelength of first stack of Si doped InAs: (a) experiment, (b) simulation.

Figure 2.12 Emissivity spectrum for p polarization varies with angle of incidence and wavelength of second stack of Si doped InAs: (a) experiment, (b) simulation.

Figure 2.13 Comparison between two different thickness InAs thin films: red curve is the averaged emissivity between 12.5 and 15μm of the first InAs film with a 50nm thickness for each doping level and the black curve is the averaged emissivity of the second film with a 150nm thickness for each doping level (both in p polarization)

Figure 2.14 Comparison of the emissivity in p polarization between two different doping level InAs thin films

Figure 2.15 Comparison of the emissivity spectrum in p polarization between two different doping level InAs thin films: (a) doping level varies from 4.5 to 2.0e18cm^{-3}, (b) doping level varies from 1.9 to 1.0e18cm^{-3}

Figure 3.1 Reflection of the 1D non-Hermitian Photonic Crystal system: (a) schematic diagram of the 1D non-Hermitian photonic crystal, (b) reflectivity for three different permittivities of the lossy layers. A reflectivity peak of 0.57 is observed at frequency = 0.35, (c) real part of the band-structure for the 1D photonic crystal calculated from assuming real wavevector (colored lines) and real frequency (thin black lines). Note the presence of bandgaps is only when the wavevector is purely real, (d) the zoomed in first and second band where we can see more clearly the presence of a quasi bandgap around frequency = 0.35, (e) Imaginary bandstructure for the 1D non-Hermitian photonic crystal assuming real wavevector, (f) Inverse group velocity which is also known as the density of states defined by $(d\omega/dRe[\kappa])^{-1}$ calculated from assuming the real frequency

Figure 3.2 Perturbation theory prediction for the quasi bandgap size (a) imaginary bandgap size between the first and second band from 1st order perturbation theory and (b) real bandgap size between the first and second band from 2nd order perturbation theory, (c) imaginary bandgap size between the second and third band from 1st order perturbation theory and (d) real bandgap size between the second and third band from 2nd order perturbation theory

Figure 3.3 2D non-Hermitian photonic crystal (a) schematic diagram of 2D non-Hermitian photonic crystal with square lattice lossy rods (r = 0.21a, where a is the lattice constant) which have $\epsilon_2 = 2 + 2i$ in a lossless background $\epsilon_1 = 2$, (b) TM bandstructure from $\Gamma - X - M - \Gamma$ (dashed blue lines are the bandstructure for the corresponding Hermitian or lossless crystal with homogeneous permittivity of 2), (c) real part of the bandstructure at all combinations of k_x and k_y, (d) imaginary part of the bandstructure at all combinations of k_x and k_y

Figure 3.4 Reflectivity of the 2D non-Hermitian photonic crystal for TM mode at normal incidence. The reflectivity has a sharp peak at frequency 0.35 and a weaker peak at 0.71, which is similar to what we observed in the 1D photonic crystal

Figure 3.5 A selectively reflective waveguide (a) schematic diagram of the reflector: this left part of the selective reflector is a 2D triangular air hole photonic crystal with a linear defect. The right part of this reflector is a non-Hermitian square lattice photonic crystal with square array of lossy pillars ($\epsilon = 13 + 6i$) embedded in the lossless substrate with the same real part of permittivty ($\epsilon = 13$), (b) reflectivity and transmission of the combined selective reflector from 0.9μm to 1.2μm, (c) and (d) out of plane electric field E_z distribution at two different wavelengths 1.13 μm and 1.077μm respectively

Figure 4.1: Conceptual schematic of tunable emissivity surfaces: Low-emissivity, high-reflectivity interior surface reflects radiative heat back to the body in cold weather conditions. By contrast, high emissivity and absorptivity interior walls absorb the radiative heat released from the occupant during warm-weather conditions

Figure 4.2. Validation model. Geometry of the model room: (a) the model use in the experimental study. (b) our computational model

Figure 4.3. Comparison between the measurement and the CFD prediction in Validation. The air temperatures in the room at different heights

Figure 4.4. Grid independence. Average velocity results of different horizontal planes for the two analyzed grid mesh (1) 245,284 cells and (2) 490,568 cells

Figure 4.5. Calculating the relationship between set point temperature and surface emissivity. Flow of determining the emissivity of interior walls and set point relation

Figure 4.6: Computational model (a)**:** 3D model built to simulate a standing person in a conditioned space, to assess the impact of tuning the thermal emissivity of the spaces that surround the human occupant. (b) Radiative heat loss of the occupant varies with the emissivity of their surroundings, and is shown for six different wall temperature scenarios from 13°C to 25°C. (c) The set point temperature varies as the emissivity of the interior surfaces surrounding the human occupant goes from 0.9 to 0.1

Figure 4.7. Temperature and velocity distribution in single occupant scenario (a) and (e) Temperature distribution on central x-z plane in winter (t_{wall}=13°C, ε=0.9) and summer (t_{wall}=25°C, ε=0.9), (b) and (f) Temperature distribution on central x-y plane in winter (t_{wall}=13°C, ε=0.9) and summer (t_{wall}=25°C, ε=0.9), (c) and (g) velocity distribution on central x-z plane in winter

(t_{wall}=13°C, ε=0.9) and summer (t_{wall}=25°C, ε=0.9), (d) and (h) velocity distribution on central x-y plane in winter (t_{wall}=13°C, ε=0.9) and summer (t_{wall}=25°C, ε=0.9)

Figure 4.8 Radiative and convective heat loss in six different wall temperature scenarios

Figure 4.9 Radiative heat loss calculated both from CFD model and Equation 4.2 in six different wall temperature scenarios

Figure 4.10. Coupling internal and external environment. (a) Schematic description of the settings in the model, (b) Wall temperature varies with emissivity for both summer and winter conditions, and (c) average air temperature (set point) varies with the emissivity of the walls as well

Figure 4.11. Effect of occupant location on CFD results. (a) Temperature distribution in the x = 0.5m plane when the wall temperature is 13°C and the occupant located 1 m off the center, (b) Temperature distribution in the z = 1.5m plane when the wall temperature is 13°C and the occupant located at 1m off the center, (c) Average air temperature in the room varies with the emissivity of the walls in the center located and off center located case respectively when the wall temperature is 13°C

Figure 4.12: Multiple occupant scenario: (a) Computational model for multiple occupants in a conditioned space. (b) Radiative heat loss as a function of emissivity in both cold weather (black line) and warm weather (red line) conditions (c) The heating set point decreases from 23° to 14.8°C when the emissivity varying from 0.9 to 0.1 (black line), while the cooling set point increases from 22.8°C to 26°C as the emissivity increases from 0.1 to 0.9

Figure 4.13. Temperature and velocity distribution in multiple occupants scenario. (a) and (e) Temperature distribution on central x-z plane in winter (t_{wall}=13°C, ε=0.9) and summer (t_{wall}=25°C, ε=0.9), (b) and (f) Temperature distribution on central x-y plane in winter (t_{wall}=13°C, ε=0.9) and summer (t_{wall}=25°C, ε=0.9), (c) and (g) velocity distribution on central x-z plane in winter (t_{wall}=13°C, ε=0.9) and summer (t_{wall}=25°C, ε=0.9), (d) and (h) velocity distribution on central x-y plane in winter (t_{wall}=13°C, ε=0.9) and summer (t_{wall}=25°C, ε=0.9)

Figure 4.14: Thermal comfort evaluation. (a) Mean radiant temperature t_r changes as the emissivity of the wall varies at different wall temperatures, (b) PMV for different wall temperatures with the emissivity of the building interiors varies from 0.9 to 0.1

Figure 4.15. PMV values at different relative humidity levels. (a) PMV values as a function of wall temperature and emissivity when the relative humidity is 30%, (b) PMV values as a function of wall temperature and emissivity when the relative humidity is 60%

Figure 4.16: Potential energy savings throughout the year due to modified setpoints made possible by specific interior surface emissivity values: Annual energy use from a preliminary analysis for (a) heating and cooling by using high emissivity ($\varepsilon = 0.9$) and low emissivity ($\varepsilon = 0.1$) interior in a small hotel reference building located in Minneapolis, USA (continental climate) and (b) in a small hotel reference building located in Ancona, Italy (humid subtropical climate)

LIST OF TABLES

ACKNOWLEDGMENTS

Still felt it was like yesterday that I waved at my parents at the airport and started my PhD in the United States. There are so many different emotions mixed at this stage and the acknowledgments became the hardest to write in this dissertation.

It is so hard for me to even have a start to thank my advisor Professor Raman. He simply is the best mentor and advisor I can ask for. I could not recall a single meeting that I came out of his office or zoom without a better understanding of the next step and a firmer feeling that I can figure that thing out. Encouragement, patience, support, and care from him are the things which I talked the most with my family, my friends and the prospective students in our department. Many among his curiosity to nature, sincerity to science, critical judgment to research and efficient communication skills have set a best role model for me over the years and will lead me through many other years in my next career stage. I will always be proud to say I'm the first PhD student come from our Raman Lab.

My sincere appreciation goes to my committee members Professor Bruce Dunn, Professor Qibing Pei and Professor Chee Wei Wong for their valuable and constructive input for this thesis. I also appreciate the help form their students very much: Patricia McNeil from Professor Dunn's group, for the FTIR measurement in the beginning of the thermal directional emitter project; and Dr. Yuan Meng from Professor Pei's group for the useful discussion we had; and Talha Yerebakan, Murat Can Sarıhan and James Mcmillan from Professor Wong's group for the discussion regarding the simulation.

During the experimental process, my special thanks go to Dr. Baolai Liang at CNSI for his great support and insights in the MBE process. His deep knowledge in III-V semiconductor is truly impressive. Mr. Hoc Ngo from Nanolab also gave me important help and training during the thin film deposition.

Friends and my lab mates are of course the precious seashells during this journey. My friends in Philadelphia (Dr. Yuejun Yan and Dr. Aoyi Luo especially, for their care for me as a junior student) and friends at Los Angeles (glad I made numerous good friends here and hard to make a full list hhh). You guys made my PhD life after research extremely joyful. Cannot say enough how happy I am when spending time with you.

My parents don't speak English. But I will write them a letter in Chinese after my defense to tell them how much I love them and how supportive they are as parents. As for exploring the world and myself, I never know there is a thing called boundary or limit set by them. They give me the best and let me fly like a free bird. And this bird has not been home for almost two years, I miss my parents and my brother. Yazhou, we are going to play hard when I come back.

VITA

2018–2021 Graduate student researcher, Materials Science and Engineering, University of California, Los Angeles

2017–2018 Graduate student researcher, Mechanical Engineering and Applied Mechanics, University of Pennsylvania

2010–2017 B.S. and M.Eng, Energy and Power Engineering, Xi'an Jiaotong University

PUBLICATIONS

[1] **Xu, Jin,** Jyotirmoy Mandal, and Aaswath P. Raman*. "Broadband directional control of thermal emission." Science 372.6540 (2021): 393-397.

[2] **Xu, Jin,** and Aaswath P. Raman*. "Controlling radiative heat flows in interior spaces to improve heating and cooling efficiency." iScience (2021): 102825.

[3] **Xu, Jin,** and Aaswath P. Raman*. "Quasi-bandgap behavior in non-Hermitian photonic crystals." Submitted.

Chapter 1 Broadband directional control of thermal emission

Controlling the directionality of emitted far-field thermal radiation is a fundamental challenge. While photonic strategies enable angular selectivity of thermal emission over narrow sets of bandwidths, thermal radiation is inherently a broadband phenomenon. We lack the ability to constrain emitted thermal radiation to fixed narrow angular ranges over broad bandwidths. We introduce gradient epsilon-near-zero (ENZ) materials that enable broad spectrum directional control of thermal emission.

1.1 Introduction

Thermally-generated light is a fundamental feature of nature[1–5]. The ubiquity of thermal emission makes its control of central importance to a broad range of technologies from energy conversion[6,7] to imaging[5,8] and sensing[9–11]. Thermal emitters are, in general, incoherent sources that lack directionality. However, high thermal emission at unwanted directions can lead to low efficiency and effectiveness for many thermal devices and applications[12]. Controlling the angular response of thermal emission has thus been investigated using a range of strategies[13], including surface plasmon polariton gratings and metasurfaces[14–17], phonon-polariton-based gratings[18], or photonic crystals[14]. While these past approaches have demonstrated anomalous angular control of thermal emission, they have been over narrow bandwidths, with the direction of emission varying as a function of wavelength. Thermal radiation, however, is intrinsically a broadband phenomenon. The ability to constrain broad spectrum thermal emission to a fixed, narrow set of directions would be a fundamentally enabling capability[19], as it would facilitate high radiance and heat transfer in terms of bandwidth while restricting this heat transfer to specific angular ranges. This capability is of particular relevance to a range of sensing and energy applications including thermal imaging

[20], thermophotovoltaics[21,22] and radiative cooling[23–25], where avoiding directional noise, and parasitic heat gain or loss, can result in substantial gains in device efficiency.

Broadband angular selectivity in the propagation and absorption of electromagnetic waves has proven to be a difficult task[13]. Advancements to enable angular selectivity in the transmission of light over optical wavelengths have been accomplished by exploiting a Brewster-angle-enabled effect[26,27]. Broadband angular control of thermal emission from a bulk or nanostructured material however remains challenging. Few theoretical proposals, however, examined the use of hyperbolic or plasmonic metamaterials that support a broad spectrum Brewster angle that could enable this capability[19,28].

1.2 Epsilon Near Zero (ENZ) materials

An alternate approach for absorption and emission angular control lies in using thin, subwavelength films of materials exhibiting epsilon near zero (ENZ) behavior[29,30] . These materials are known to support a leaky p-polarized electromagnetic mode near the material resonance pole, termed a Berreman mode[31–35]. This mode can couple to propagating free-space modes at a range of wave vectors and thus angles of incidence. Prior work has characterized the angular characteristics of this mode and its coupling to free space, both for absorption over near infrared (NIR) wavelengths[32,36–39] as well as for thermal emission and long-wave infrared (LWIR) absorption from a range of oxides[31,33,40]. This angular response, while intriguing, is however fundamentally narrow-band in nature, with no known mechanism for how it can be extended into a broadband response over the same sets of angles and thereby functioning as a broadband directional emitter or absorber.

To enable broadband directional thermal emission, we introduce the concept of gradient ENZ materials whose permittivity crosses zero at a range of frequencies that vary across a spatial gradient. We show that a gradient ENZ film along the depth dimension supports broad spectrum leaky modes that couple to free-space propagating modes at the nearly the same angles of incidence over that bandwidth, thus functioning as a broadband directional thermal emitter whose angular range of 'thermal beaming' can be controlled by total film thickness. We fabricated two deep-subwavelength photonic structures as experimental realizations of the conceptual gradient ENZ film. Each structure consists of three polaritonic oxide materials that collectively support gradient ENZ behavior at different and complementary parts of the long-wave infrared (LWIR) wavelength spectral range. We experimentally characterized the spectral and angular response of both photonic structures and demonstrate broadband thermal beaming in the p polarization from 7.7 to 11.5μm over an angular range of 70° to 85° for the first structure, and from 10.0 to 14.3μm over an angular range of 60° to 75° for the second structure. We performed direct emission measurements at fixed temperatures to verify the directional nature of thermal emission at different angles for each structure.

Consider a thermal emitter with low emissivity over all wavelength, $\varepsilon(\lambda,\theta) \sim 0$, at all polar angles of incidence θ except between a fixed, narrow set of angles $\theta_{emit} \in [\theta_1, \theta_2]$ where it exhibits higher emissivity, $\varepsilon_{high}(\lambda,\theta_{emit})$. Such a broadband directional thermal emitter or broadband thermal antenna (Figure 1.1 (a) and 1.1(b)), would then exhibit high radiance over a particular range of angles defined by θ_{emit}, but at all other angles appear as reflective, and low emissivity, as a mirror. This situation is in contrast to conventional bulk materials as well as finite-size nanostructures, where light typically couples to propagating free space modes at a particular wave vectors *k,* and thus angles of incidence θ, that vary as a function of frequency ω (including materials that support

the Berreman mode). While metals have a well-known polarization-dependent reduction in grazing angle reflection, which corresponds to an absorption and emission peak, this effect is only applicable at very large, grazing angles (~85°). Instead, we seek to enable optical structures whose electromagnetic modes couple to free-space modes at angles defined by θ_{emit} over a large bandwidth. Central to this broadband thermal beaming capability is the emitter's ability to present high emissivity over a broad range of wavelengths while maintaining the same angular selectivity and directionality throughout that wavelength range.

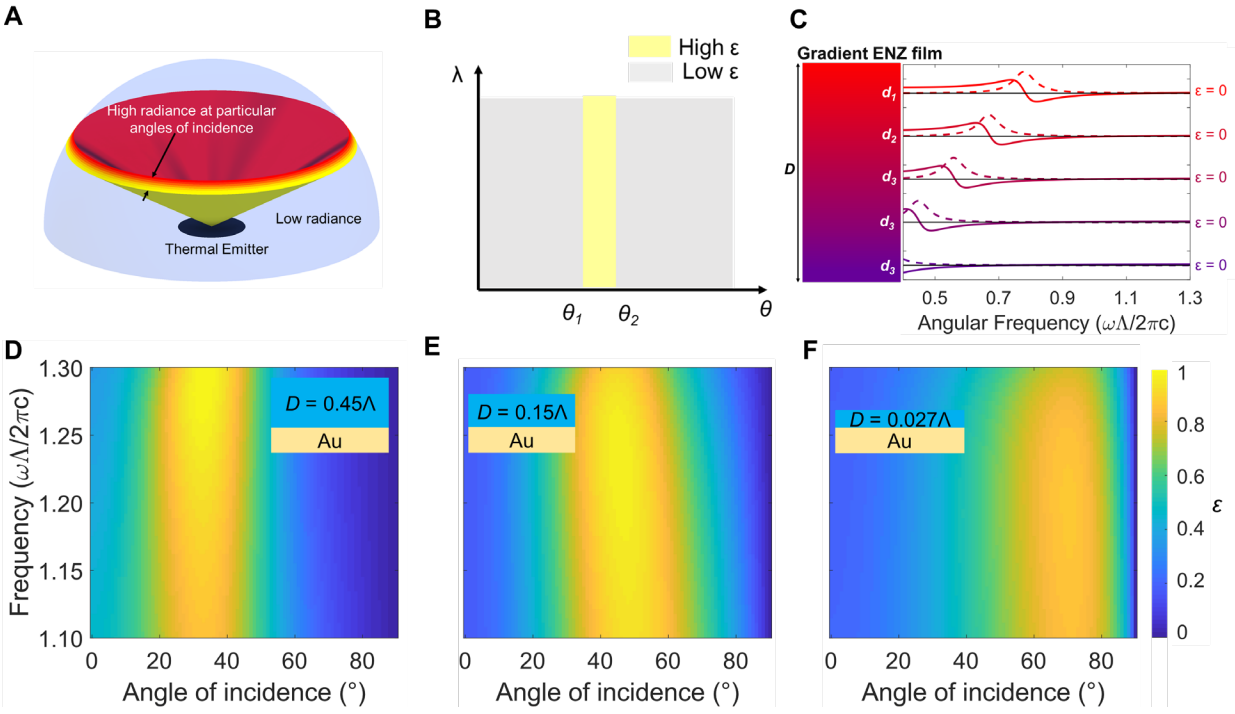

Figure 1.1. Illustration of the broadband thermal directional emitter (a) and (b) Schematic capability of a broadband thermal directional emitter: having low emissivity except at certain angles of incidence and emission, where it shows high emissivity across the entire thermal wavelength range of interest. (c) Schematic representation of the spatial gradient in the permittivity

of the gradient ENZ film, whose dielectric permittivity is effectively near to zero across a wide dimensionless frequency range from 1.1 to 1.3, (b-d) Emissivity of the gradient ENZ film varying with the total thickness in p polarization as a function of angle of incidence and angular frequency. As the total thickness of the gradient ENZ materials increases from 0.027Λ to 0.15Λ and 0.45Λ respectively where Λ is the mean wavelength of the whole wavelength range, the center of the high emissivity band moves from 70° to 50° and 30°.

1.2.1 Ideal ENZ materials

Conceptually, a material whose dielectric permittivity is near zero over a broad range of wavelengths can act as a broadband directional thermal emitter in the p polarization. We first consider an idealized ENZ thin film on a substrate of gold, with constant Re(ε) = 0.01 and Imag(ε) = 0.01i over a relevant thermal wavelength spectrum, from 8 to 12 μm corresponding to the peak regions of the blackbody spectral radiance of a 300 K object. We plot in Figure 1.2 (a) a transfer-matrix calculation of the emissivity and absorptivity of such a film of thickness d = 500 nm for p-polarization. The film displays the desired behavior schematically shown in Figure 1.1: it has high emissivity in the p polarization over a narrow range of angles centered around 10°, with low emissivity at other angles, for all wavelengths of interest. For s polarization, the film has near-zero emissivity at all wavelengths. Thus, the angular nature of its polarization-averaged emissivity is defined by the p polarization response.

Directional thermal beaming to different angular ranges can be achieved by changing the thickness of the ENZ film. As shown in Figure 1.2 (b) and (c) at 50 nm and 5 nm thickness, the angular band of high emissivity is centered at 30° and 70° respectively. To capture the relationship between thickness and angular response, Figure 1.2 (d) shows the emissivity spectrum of the ideal ENZ thin film as its thickness varies from 0 nm to 500 nm at a wavelength of 8 μm for the p-

polarization. As the film gets thicker, the emissivity peak moves from large angles of incidence to small angles.

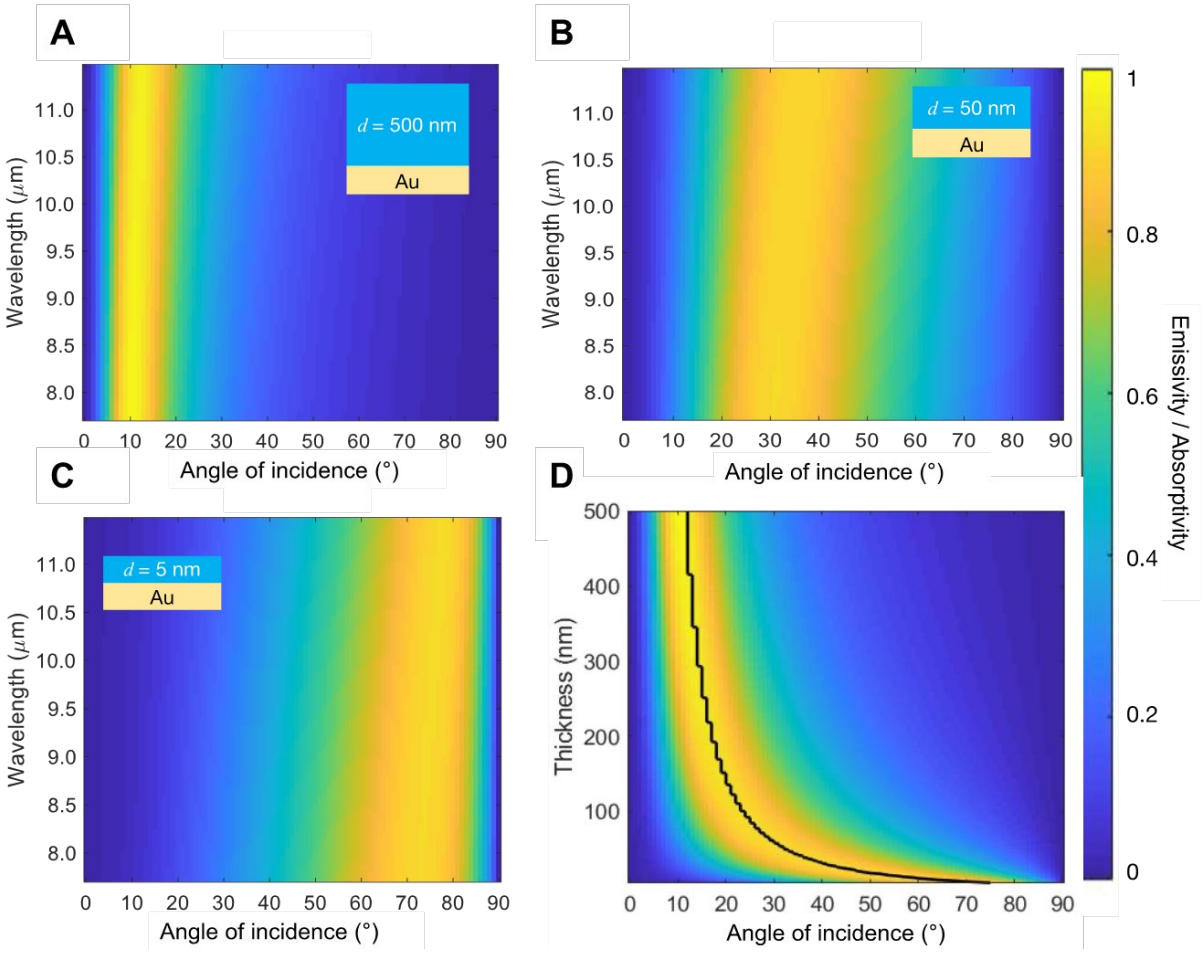

Figure 1.2. Emissivity spectrum of an ideal ENZ thin film for p-polarization. (a)-(c). The thickness of each ideal ENZ thin film is $d = 500$ nm, $d = 50$ nm, $d = 5$ nm, respectively. (d) Emissivity spectrum of the ideal ENZ thin film as the thickness varies from 0nm to 500nm at 8μm for p-polarization. As the thin film gets thicker, the emission peak moves from large to small angles.

1.2.2 Impact of permittivity values on broadband angular selectivity

Epsilon near zero (ENZ) materials can exhibit high absorption and emission of electromagnetic waves near their ENZ frequencies. For propagating modes in ENZ films, the absorption A can be defined as[31]:

$$A(r,\omega) = 0.5\omega Im[\varepsilon(\omega)]|E(r,\omega)|^2 \tag{1.1}$$

Due to the continuity of $\varepsilon E_\perp$ in the p polarization, the electric field $E_\perp$ is both enhanced and strongly confined in the ENZ films:

$$E(r,\omega) = \frac{E_0\,(r,\omega)}{Re(\varepsilon(\omega))} \tag{1.2}$$

Here E_0 is the electrical field free space. Substituting Eq. 1.2 to Eq. 1.1, the absorption is related to the Im[ε] and Re[ε] as

$$A(r,\omega) = 0.5\omega Im[\varepsilon(\omega)]|\frac{E_0\,(r,\omega)}{Re[\varepsilon(\omega)]}|^2 \tag{1.3}$$

From Eq. 1.3 we can see that when Re[ε] approaches zero, the absorption can be strongly enhanced. The absorption value however is also strongly influenced by Im[ε]. The strength of Im[ε] when Re[ε] approaches zero influences the overall angular width of absorption one will obtain at a particular frequency in a thin ENZ film. The larger Im[ε] is, the larger the angular width will be. This in turn can place limits on this approach to angular selectivity and broadband thermal beaming. To explore this relationship, we conduct a series of simulations for thin films which have a range of real and imaginary permittivities. We determine the optimal thickness for these thin films to support high absorption and emission at an angle of incidence near normal, with the results shown in Figure 1.3.

We can see that, given the same Im[ε], the larger Re[ε] is, the harder it is for the thin film to have an angle of incidence with high emissivity only near normal incidence. For the same Re[ε], for modes which can be coupled into the film from free space, the high emissivity angle of incidence is more likely to be constrained to near normal incidence when Im[ε] is smaller. This is driven in large part by the fact that, due to their dispersion relation, ENZ films that couple to free-space modes near-normal incidence need to have a larger thickness. If Im[ε] is substantially greater than zero, this can cause absorption to occur over a broader range of k values, and thus angles of incidence, due to the larger thickness of the film.

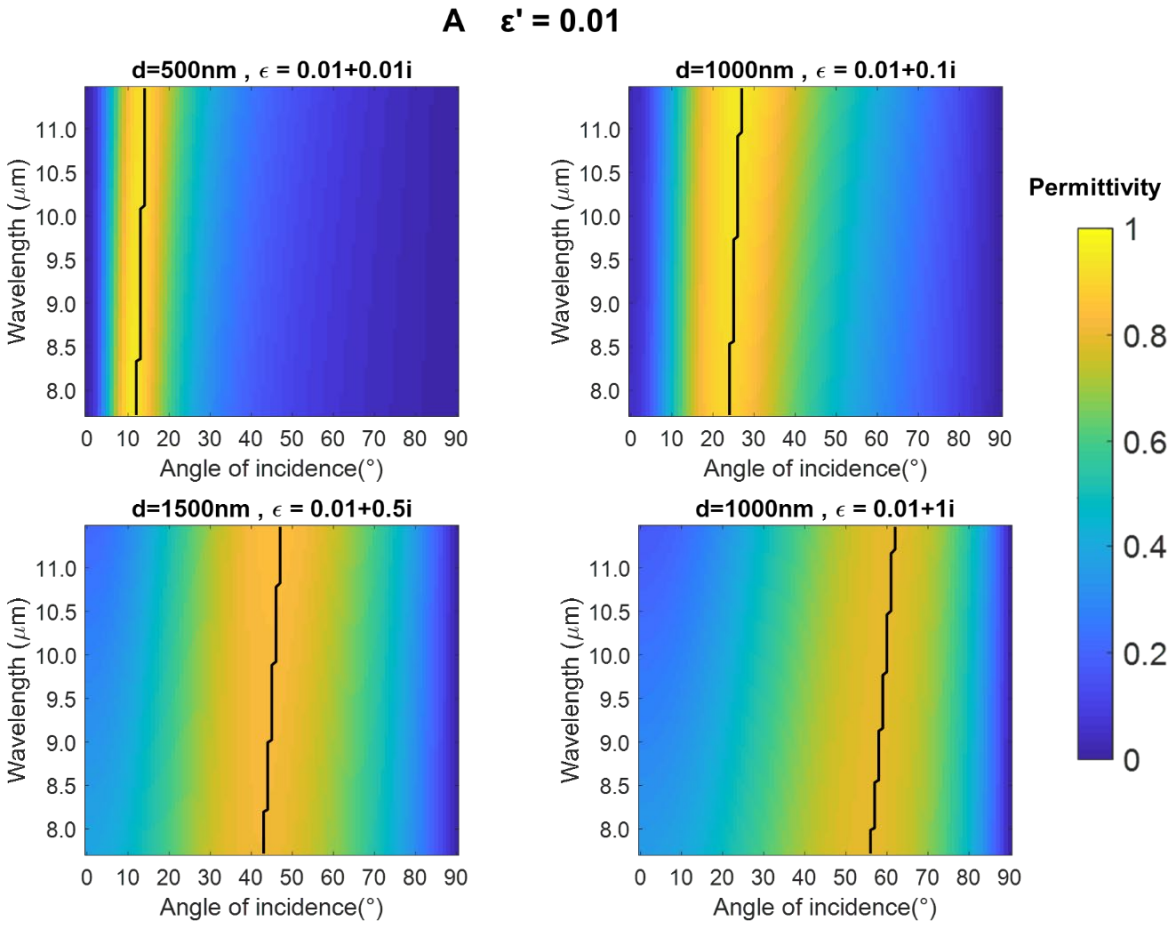

B ε' = 0.1

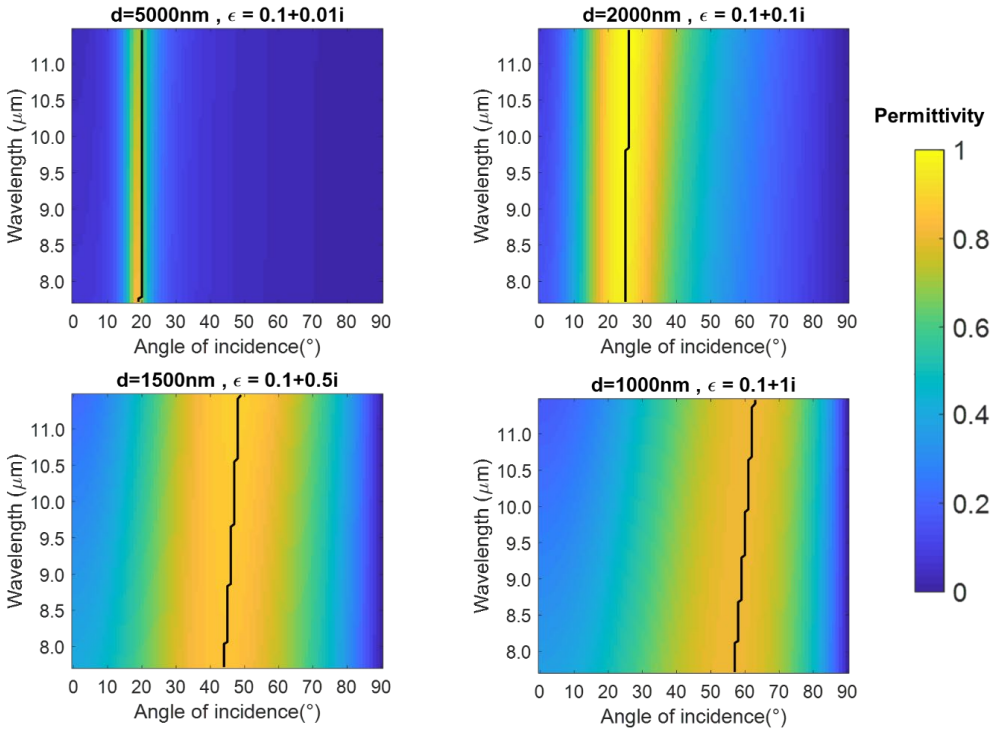
d=5000nm , ϵ = 0.1+0.01i
d=2000nm , ϵ = 0.1+0.1i
d=1500nm , ϵ = 0.1+0.5i
d=1000nm , ϵ = 0.1+1i
Wavelength (μm)
Angle of incidence(°)
Permittivity

C ε' = 0.5

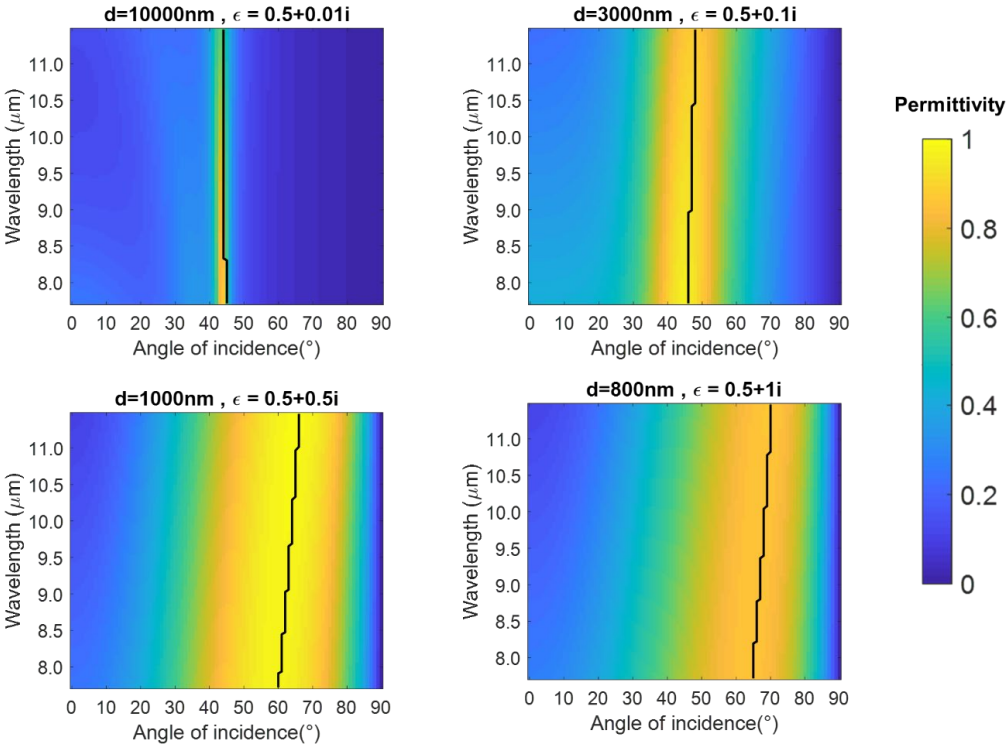
d=10000nm , ϵ = 0.5+0.01i
d=3000nm , ϵ = 0.5+0.1i
d=1000nm , ϵ = 0.5+0.5i
d=800nm , ϵ = 0.5+1i
Wavelength (μm)
Angle of incidence(°)
Permittivity

Figure 1.3. Emissivity spectra of thin films with varying real and imaginary permittivities near zero for p-polarization as a function of angle of incidence over a fixed wavelength range. Results are grouped by real permittivities (ε'): (a) $\varepsilon' = 0.01$, (b) $\varepsilon' = 0.1$, and (c) $\varepsilon' = 0.5$.

1.2.3 Gradient ENZ film

While intriguing theoretically, in real materials ENZ behavior is tied to material dispersion and a resonance (through either electron or phonon interactions), and is thus inherently narrowband, as has been observed with free-space coupling to the Berreman mode. To overcome this limitation, we introduce the concept of gradient ENZ materials whose permittivity is defined by a material resonance pole that changes its frequency across a spatial gradient. More specifically, we consider 1D gradient ENZ films whose permittivity we express by modifying the standard model for the dielectric function of a polaritonic material with loss:

$$\varepsilon(\omega, d) = \varepsilon_\infty \left(1 + \frac{{\omega_L}^2 - {\omega_T}^2}{{\omega_T}^2 - (\omega - (\frac{d}{D})\omega_{range})^2 - i\gamma(\omega - (\frac{d}{D})\omega_{range})}\right), 0 \leq d \leq D$$

$$\omega_{range} = \omega_L - \omega_T \tag{1.4}$$

Here ω_T and ω_L are phonon frequencies correspond to out-of-phase atomic lattice vibrations with wave vectors aligned parallel (L, longitudinal) and perpendicular (T, transverse) to the incident field, ε_∞ is the permittivity at infinite frequency, γ is the damping rate, d is the depth in the gradient ENZ film and is bounded by 0 and D where D is the film's total thickness. At each point along the depth dimension (in Figure 1.2 (c), d_1, d_2, d_3, d_4 and d_5 for example), we thus have the permittivity crossing zero at different frequencies, establishing a range of ENZ frequencies that vary spatially. As the depth increases, this crossing point moves to smaller frequencies. This

gradient ENZ film exhibits ENZ values across a wide dimensionless frequency range from 1.1 to 1.3, a range that can be tuned by altering the overall spatial gradient of the material pole response.

To show that gradient ENZ materials can enable broadband directionality in absorption and emission, we characterized the spectral and angular response of three different total thicknesses of gradient ENZ film in the p-polarization, using transfer-matrix simulations (Figure 1.1(d)-(f)). The thinnest film (Figure 1.1(f)) displays the desired behavior shown schematically (Figure 1.1(b)) as it has high emissivity in the p polarization over a narrow range of angles, centered at 70°, with low emissivity at other angles, in the dimensionless frequency range from 1.1 to 1.3 where the entire gradient ENZ film supports near zero permittivity at across its depth. As the total thickness of the gradient ENZ materials increases, the angular range of high emissivity moves towards normal incidence (up to ~25° in our example here) but consistently over the entire bandwidth (Figure 1.1(d), (e)), indicating the ability of gradient ENZ films to 'beam' their thermal radiation at a range of angles in the p-polarization.

1.2.4 Theoretical model of photonic structures' electromagnetic modes

To better understand the source of this behavior, we calculated the dispersion relations of the gradient ENZ films with different thicknesses in the p-polarization. We calculate the photonic film's dispersion relation by finding the wavevector which presents minimum reflectivity for a given frequency ω and perform this search iteratively throughout our frequency range of interest[33]. The reflectivity is calculated by the transfer matrix method for p polarization. The transfer matrix for the *j*th film in a multilayer film in the p polarization is given by

$$M_j = \begin{pmatrix} cos(k_j a_j) & isin(k_j a_j)\frac{\varepsilon_j \omega}{ck_j} \\ isin(k_j a_j)\frac{ck_j}{\varepsilon_j \omega} & cos(k_j a_j) \end{pmatrix} \tag{1.5}$$

where $k_j = \sqrt{\varepsilon_j \frac{\omega^2}{c^2} - k_x^2}$, ε_j is the permittivity, ω is the free space frequency of the light, c is the speed of light and a_j is the thickness of the jth layer. The transfer matrix for the whole film consisting of N layers is then given by the product of the respective transfer matrices for the individual layers.

$$M = \prod_{i=1}^{N} M_j = \begin{pmatrix} m_{11} & m_{12} \\ m_{21} & m_{22} \end{pmatrix} \tag{1.6}$$

The reflectivity R of the overall film is then calculated as:

$$R = r^2 = \left(\frac{m_{21}}{m_{11}}\right)^2 \tag{1.7}$$

Figure 1.4 shows the dispersion relation of the gradient ENZ thin film described in Figure 1.1. As we vary the total thicknesses of the film, from the red curve (0.027 Λ) to green (0.15Λ) and blue curve (0. 45Λ), where Λ is the mean wavelength of the interested wavelength range, the broadband Berreman mode moves towards normal incidence, which is corresponding to the results in the Figure 1.1(d)-(f).

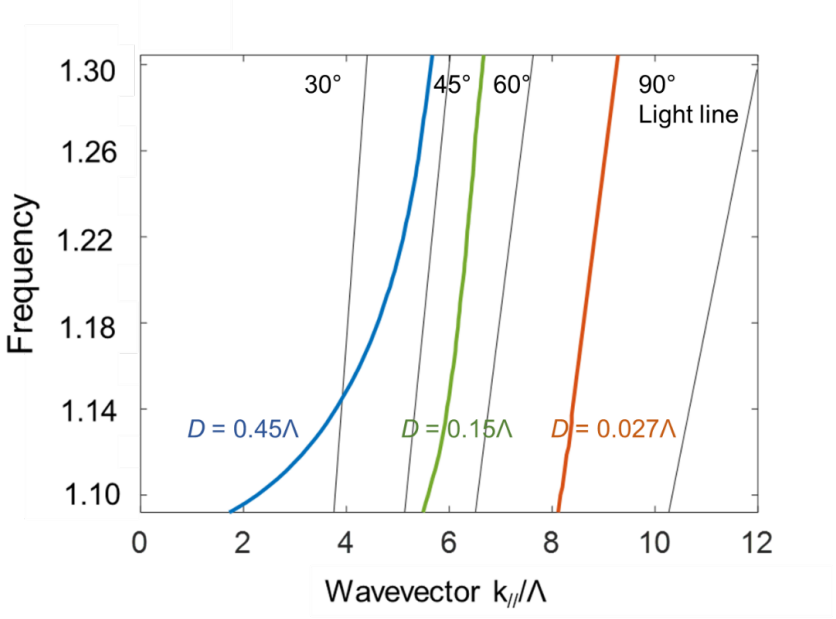

Figure 1.4. Dispersion relation of the gradient ENZ thin films. The total thicknesses, for the red, green and blue curves, increases from 0.027 Λ to 0.15Λ and 0.45Λ respectively, where Λ is the dimensionless average wavelength. The broadband Berreman mode moves towards normal incidence as the total thickness of the gradient ENZ film increases, which agrees to the results in Figure 1.1. (d)-(f).

We observed that gradient ENZ films support unique, broadband Berreman modes to the left of the light line which couple to free space modes of nearly the same angle of incidence over the entire frequency range (1.1-1.3). In particular, as a function of thickness, the gradient ENZ film's supported mode is nearly parallel to the corresponding propagating free-space mode for a fixed angle of incidence over the entire frequency range, a different and unexpected behavior in conventional materials as well as photonic structures. Moreover, we again observed that as the film's thickness increases, the mode moves to smaller *k* vectors, nearly parallel to the propagating free-space modes at near-normal angles of incidence. Finally, the ideal ENZ material for

broadband directional control should also have a slowly varying permittivity function around the ENZ frequency ($\frac{\partial \varepsilon}{\partial \omega}(\omega_{ENZ}) \longrightarrow 0$) and a small imaginary part of the permittivity at the ENZ frequency $\mathrm{Im}[\varepsilon(\omega_{ENZ})] \longrightarrow 0$ to enable maximal directional contrast and tunability to near-normal angles of incidence.

1.3 Experiment realization of broadband direction thermal emitter

We experimentally realized two gradient ENZ structures targeting the long-wave infrared (LWIR) wavelength range that corresponds to the blackbody spectral radiance of room-temperature range objects (300 K). For both structures, we exploited the phonon polariton response of a range of semiconductor and metal oxides throughout this spectral range that in turn yield ENZ frequencies.

1.3.1 Fabrication of the gradient ENZ film

The two ENZ photonic structures (whose SEM images are shown in Figure 2A) were both coated on the 4-inch prime silicon wafers via electrical beam evaporation method using a CHA industries MARK 40 evaporator. The start evaporating pressure is at 7.7E-7 torr. First, a 5 nm adhesion layer of Ti was evaporated with a deposition rate of 0.7Å/s, followed by a 100 nm Al layer (deposition rate of 2.0 Å/s), 200nm of Al_2O_3 (deposition rate of 2.0 Å/s), 300nm of SiO (deposition rate of 2.5 Å/s) and 100nm of SiO_2 (deposition rate of 2.0 Å/s) for the first multilayer thin film structure and 180 nm of MgO(deposition rate of 1.3 Å/s), 450 nm of TiO_2 (deposition rate of 1.8 Å/s) and 450nm of Ta_2O_5 (deposition rate of 2.0 Å/s)for the second structure.

1.3.2 Characterization of the gradient ENZ film

By Kirchhoff's law, the absorptivity of an object is equal to its emissivity or each frequency and angle of incidence when in thermal equilibrium. Since our structures were deposited on an

optically thick metal layer, the transmissivity (T) is equal to 0. Thus, to infer emissivity (ε), we measure reflectivity (R) as a function of polar angle of incidence, and plot it as $\varepsilon = 1 - R$.

Deposited samples were characterized by a Bruker Invenio-R Fourier-transform infrared spectrometer (FTIR) with a Harrick Seagull variable angle reflection accessory. An inserted wire-grid polarizer is used to selectively transmit linearly polarized light (p and s polarization namely) to the sample for measurements. Our measurements are made by establishing background reflectance from a well-calibrated reference mirror first for each measurement. The reflectivity spectra were measured for different incidence of angles from 4° to 84° at 2° increments.

The first structure was composed of silicon dioxide (SiO_2), silicon monoxide (SiO) and aluminum oxide (Al_2O_3) which presented ENZ wavelengths of 8.0 µm, 8.7 µm, and 10.7 µm, respectively. We plotted the permittivity of the three oxides based on tabulated values[41,42] (Figure 1.5 (a)). Layering them results in a gradient ENZ thin film because of their complementary resonances in the long-wave infrared part of the spectrum. For the second structure, we used tantalum pentoxide (TaO_5) [43], titanium oxide (TiO_2) [41], and magnesium oxide (MgO) [44] which presented ENZ wavelengths at 10.7 µm, 12.0 µm, and 13.5 µm, respectively (Figure 1.5 (b)). The thicknesses of both structures were optimized prior to fabrication through numerical simulations.

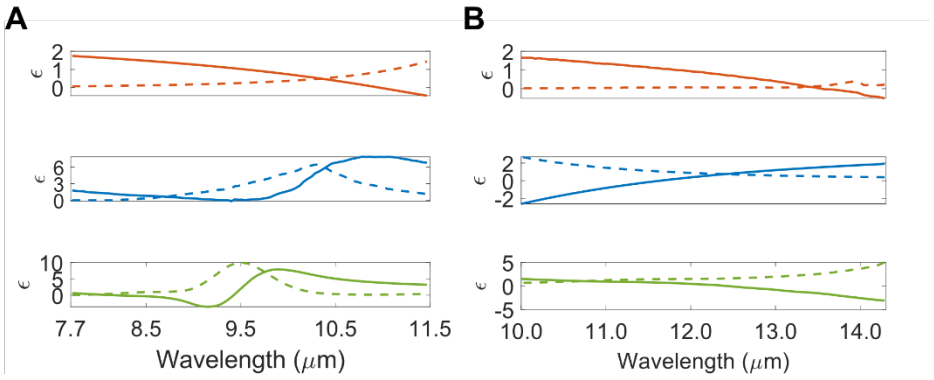

Figure 1.5. Real (solid) and imaginary (dashed) parts of the permittivities (a) SiO_2, SiO and Al_2O_3 in the first multilayer structure, (b) $Ta_2O_5/TiO_2/MgO$ in second, each of which shows a slowly-varying permittivity that crosses zero at complementary wavelengths in the long-wave infrared part of the spectrum.

We collected Scanning Electron Microscope (SEM) images of the fabricated gradient ENZ structures and the layer thicknesses (Figure 1.6), with both structures deposited atop a base layer of aluminum, on a 4-inch silicon wafer. We measured an average emissivity in the p-polarization for the first structure > 0.6 over its wavelength range of operation (7.7-11.5μm) within the angular range from 70° to 85° (green curve, Figure 1.6(b)). Outside this angular range, average emissivity is less than 0.3. This high emissivity wavelength range accounts for ~35% of the radiative heat flux of an object at 300 K, and also overlaps with the atmospheric window responsible for radiative cooling. We measured average emissivity of the second gradient ENZ structure over its wavelength range of operation (10.0-14.3μm) for p polarization above 0.7 between 60° and 75° (blue line, Figure 1.6(b)). Outside this angular range, the emissivity drops dramatically to 0.4 at 40°.

To better characterize the beaming effect, we plotted the spectral emissivity in the p polarization for angles of incidence of 10°, 30° and 74° (Figure 1.6(c)). We observed a clear and consistent emissivity difference between different angles of incidence over the spectral range from 8.0 - 11.5 μm, with as much as a 76.6% contrast obtained near 8 μm. We show the spectral nature of the angular selectivity of structure 2 in Figure 1.6(d). We observed consistent, broadband (from 10.5 - 14.3 μm) contrast between the measured emissivity at angles of incidence of 10° and 30°, and 64°, for p-polarization (for all angles, p and s polarization, see Figure 1.7). The fabricated structures present very low emissivity at all angles in the s-polarization (Figure 1.7) due to their

deep subwavelength nature. Thus, while the polarization-averaged emissivity is lower than the measured p-polarization emissivity, the angular contrast and thermal beaming effect is maintained as it is the photonic structure's p polarization response that determines its angular response. Furthermore, we observed that, as we sought, structure 1 and the structure 2 have differing peak angles of emission, at 82° and 72° respectively, with the overall angular range of high emissivity also shifting from 70°-85° to 60°-75°. These results, in addition to demonstrating the core capability of broadband directional thermal emission, also highlight that through deliberate material choice and control of physical dimensions, gradient ENZ films can deliver directional control at a range of angles of incidence with materials easily accessible today.

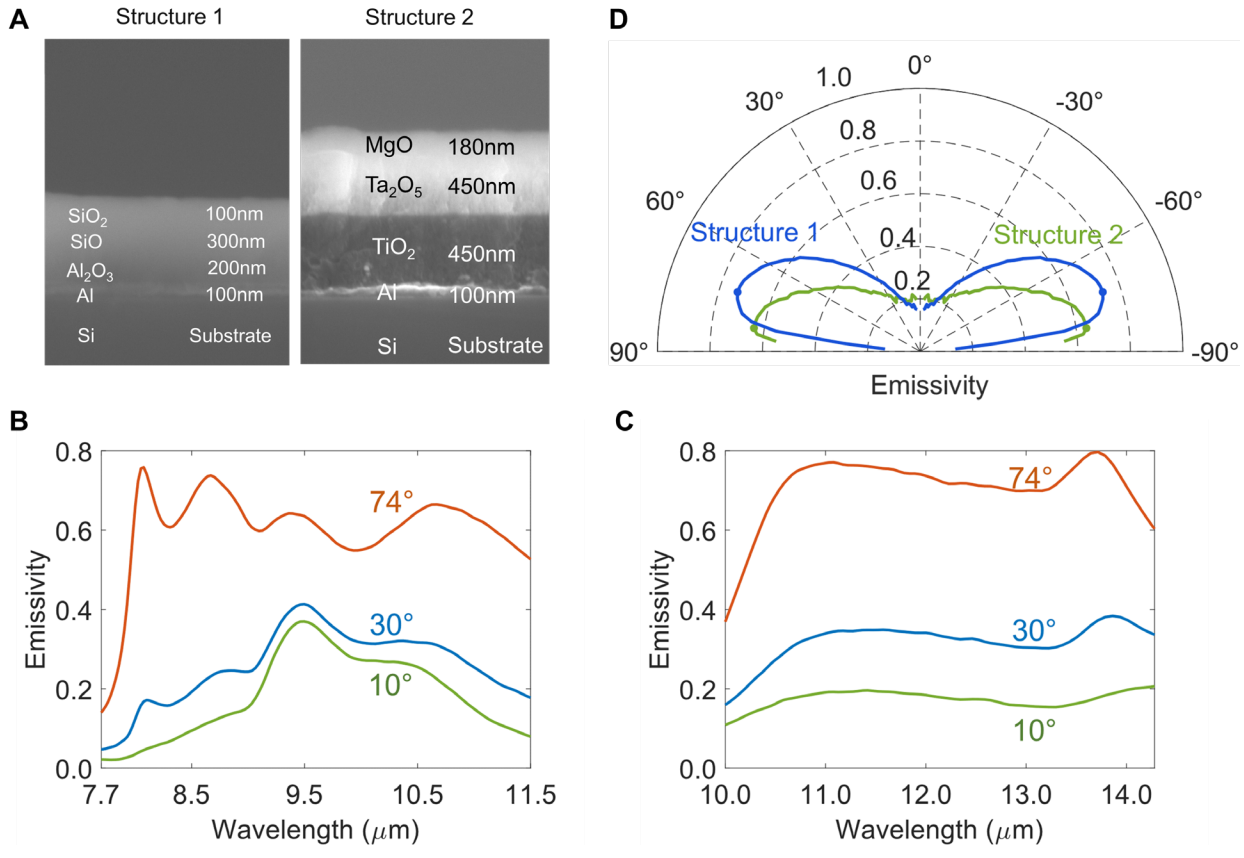

Figure 1.6. Experimental results. (a) SEM images of the experimentally fabricated multilayer photonic film structures. (e) Polar plot of the measured average emissivity over broad wavelength ranges of operation (7.7-11.5μm and 10.0-14.3 μm respectively) varying with angle of incidence for p polarization in those two structures, with high emissivity only at angles of incidence of 70° to 85° and 60° to 75° for structure 1 and structure 2 (f) and (g) Measured emissivity of the two photonic structures varying with wavelength at 3 different angles for p-polarization. Both the photonic structures exhibit a strong contrast between emissive and reflective states as a function of angle of incidence.

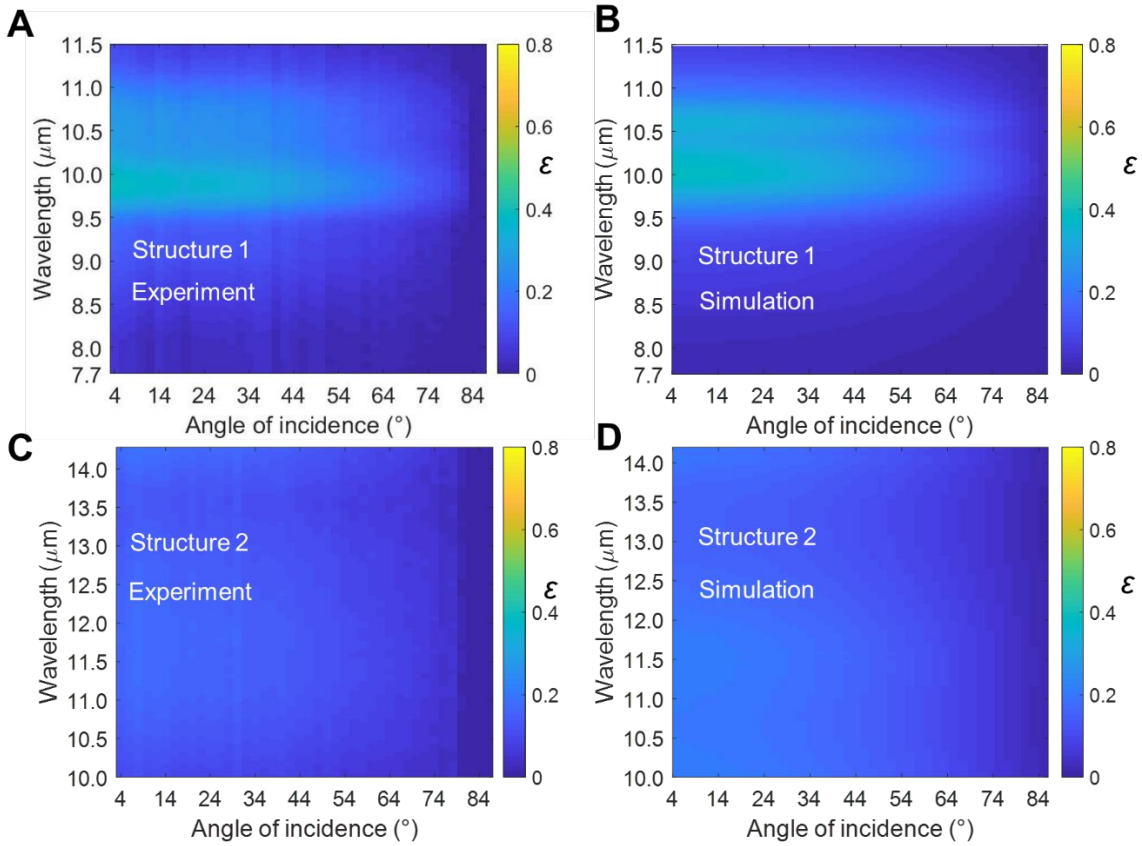

Figure 1.7. Emissivity spectra varying with angle and wavelength of the two fabricated photonic structures for the s polarization. (**a**) and (**c**) Measured emissivity spectra for s-

polarization, and (**b**) and (**d**) simulation results of emissivity in s-polarization using transfer matrix method. The results show that in the s polarization, low emissivity is exhibited by both structures regardless of angle of incidence, and that experimental results match well with simulations.

1.4 Theoretical study of broadband direction thermal emitter

1.4.1 Comparison between the simulation and experimental measurements

To validate our experimental results, we show the measured as well as simulated emissivity spectra of both structures for the p-polarization varying with wavelength and angle of incidence (Figure 1.8). For structure 1, the spectrum exhibits strong peaks at 8.0 μm, 8.7 μm and 10.7 μm respectively, which correspond to the ENZ wavelengths of SiO_2, SiO, and Al_2O_3 respectively. The overall p-polarized emissivity throughout the 7.7-11.5 μm range, within the angular range from 70° to 85°, is above 0.6 (Figure 1.8 (c)).Transfer matrix simulations of the fabricated structure (Figure 1.8 (b)) agree well with the experimental results and highlight clear angular regions of high and low emissivity that persist throughout the broad spectral range of operation. We plot the average emissivity of structure 1 over the wavelength range of operation (7.7-11.5μm) from both measured and simulated data in polar coordinates (Figure 1.8 (c)). Though the measured emissivity is lower than we expected from simulated data, the angles of operation and peak angle of incidence agree well. Similarly, we compared the measured and simulated emissivity spectra of structure 2 (Figure 1.8 (d), (e))for the p-polarization varying with wavelength and angle of incidence. Both measured and simulated spectrum exhibit continuous strong directional emission across the

wavelength range from 10.5 µm to 11.3 µm owing to the slowly varying permittivity of Ta_2O_5, TiO_2, and MgO (Figure 1.4 (b)), which makes it a good gradient ENZ film. We again note a 10° shift in peak angle of incidence between structure 1 and 2, which we verified in the numerical modeling. We show good agreement in the average emissivity of structure 2 from both measured and simulated data in polar coordinates over the wavelength range of operation (10.0 - 14.3µm) (Figure 1.8 (f)).

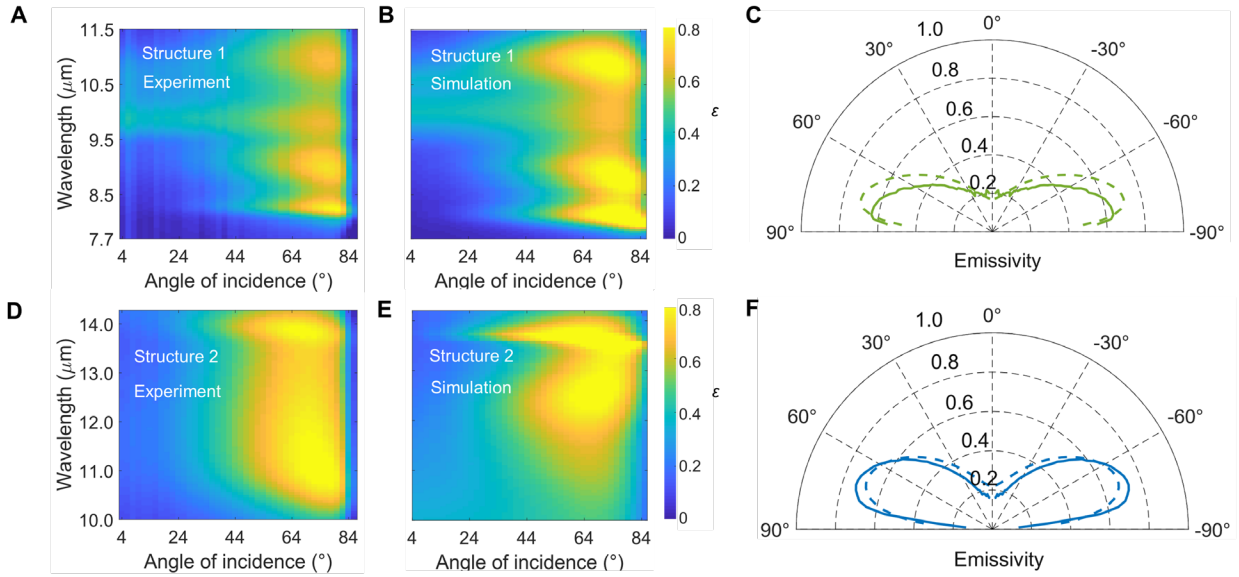

Figure 1.8. **Simulation and experiment results comparison.** (a) and (d) Measured emissivity spectra varying with angle and wavelength of the two fabricated photonic structures in p-polarization, and (b) and (e) simulation results of the emissivity of the two structures for p-polarization using transfer matrix method, both show a broadband angularly selective behavior in emissivity and match well with the experiment measurement. (c) and (f) Average emissivity of the two structures from both measurement and simulation varying with angle of incidence for p polarization over wavelength ranges of 7.7-11.5 µm and 10.0-14.3µm respectively.

1.4.2 Dispersion relation of the two gradient ENZ films

In order to understand the physical origin of the broadband thermal beaming effect we observed that was enabled by the fabricated gradient ENZ structures, we numerically calculated the dispersion relation for the two photonic structures. We calculated the dispersion relation of the two fabricated nanostructures, as well as alternative structures with differing thicknesses (Figure 1.9).

Figure 1.9 shows the calculated dispersion relation of the two fabricated gradient ENZ structures, as well as structures of alternative thicknesses with the same materials. For structure 1 (SiO_2/SiO/Al_2O_3), we observe three frequency ranges above the light line which correspond to the three ENZ wavelength ranges of SiO_2, SiO and Al_2O_3. Other frequency ranges lying to the right of the light line cannot be coupled to from free space. Importantly, we see that as the total thickness increases, the supported electromagnetic modes move to the left, and thus will couple to propagating free space modes that are closer to normal incidence, agreeing well with the theoretical analysis of the gradient ENZ structure, and indicating that angular response can be tuned by the thickness of each layer's material. Similar behavior is observed in the dispersion relation of structure 2 (Ta_2O_5/TiO_2/MgO). Owing to the gradual spectral variation in the emissivities of the three materials in structure 2, we observe a near-continuous broadband Berreman mode located to the left of the light line. This is in good agreement with what we see in both the experimental measurement and simulation in Figure 1.8. For both structures, we observed frequency ranges above the light line which correspond to the ENZ wavelength ranges of SiO_2, SiO, and Al_2O_3 in structure 1 and Ta_2O_5, TiO_2 and MgO in structure 2. Other frequency ranges lying to the right of the light line cannot be coupled to from free space. As the total thickness increases, the dispersion curve moves to the left, and thus will couple to modes from angles of incidence which are closer

to normal incidence, agreeing well with the theoretical analysis of the conceptual gradient ENZ film (Figure S6), and indicating that angular response can be straightforwardly tuned to smaller angles of incidence by increasing the thickness of each layer.

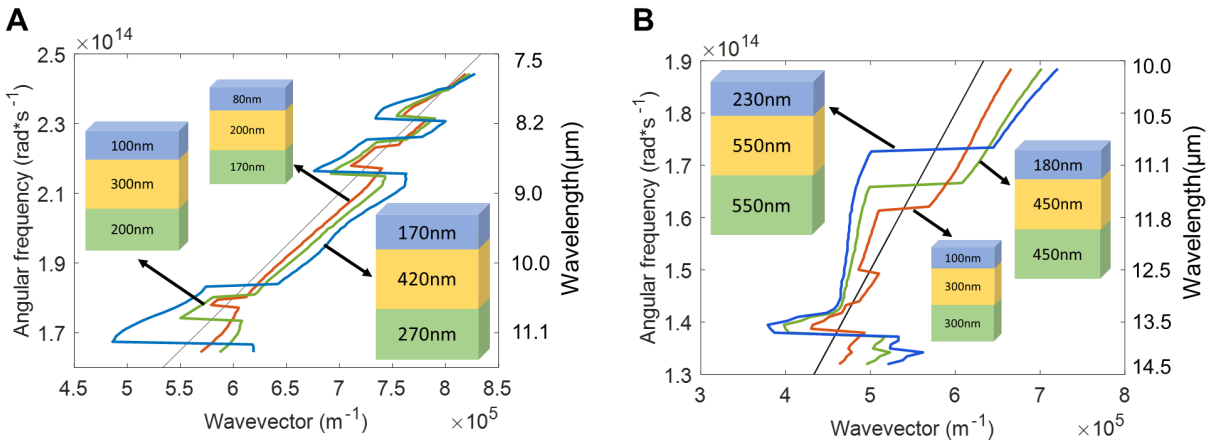

Figure 1.9. Dispersion relation of (a) gradient ENZ structure 1 (SiO_2/SiO/Al_2O_3) and (b) structure 2 (Ta_2O_5/TiO_2/MgO)

1.4 Radiometric measurement of directional emissivity

One interesting capability of the broadband nature of the directional thermal emitters we demonstrated is their ability to emit a substantial amount of heat radiatively at tailored angles of incidence. We experimentally probed this behavior through direct radiometric measurements of their directional thermal emission. Both structures, deposited on 4 inch silicon wafers, were heated to 100°C for structure 1, and 110°C for structure 2, and emitted thermal radiation detected at fixed angles with a high-resolution microbolometer array.

The emissivity ε of the two structures were radiometrically measured using a thermal camera with an uncooled microbolometer array (FLIR Boson 640). The set up for the

thermography is shown in Figure S8. The wafer was mounted on a metal block heated by a heater to a set temperature ($T_{emitter}$~100˚C for structure 1 and ~110˚C for structure 2) and placed on the center of an arc on which the microbolometer array was set facing the emitter at different angles of incidence (Figure 1.10). The emitter also had an aluminum tape with known angular emissivity placed on it as a reference. Temperatures of the emitter, tape and the air in the laboratory setting were separately measured using thermocouples. Since the apparent temperature of an emitter is also a function of the background temperature T_{bckgd} partially reflected by the emitter (1.10), a metal plate coated with a high emittance coating (ε ~0.97) in thermal contact with dry ice was used as the cold background.

For the measurements, the camera was placed at an angle θ from the surface normal to the emitter, and the plate providing the cold background was placed at $-\theta$. The apparent temperature T_{rad} of the emitter near the aluminum tape, the aluminum tape itself, and the cold background (T_{bckgd}, when in direct view of the camera) was then measured using the thermal camera assuming an emittance of 1. When not in direct view, the temperature of the cold background was calculated using Eq. 1.8 but using the apparent temperature and known emittance of the aluminum tape. With both T_{rad}, T_{emiter} and T_{bckgd} thus known by calculation or measurement, Eq. 1.8 was used to calculate the emissivity of the emitter.

$$T_{rad}^4 = \varepsilon T_{emitter}^4 + (1-\varepsilon) T_{bckgd}^4 \tag{1.8}$$

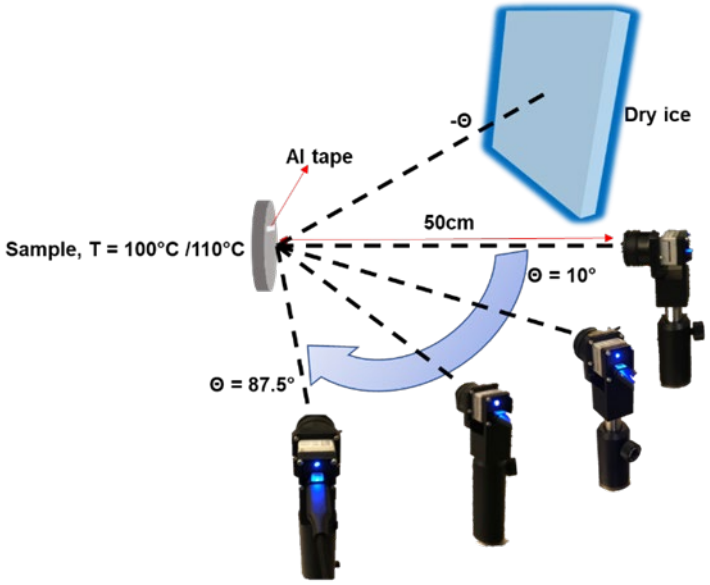

Figure 1.10. Schematic demonstration of the radiometric measurement setup

Thermographs of both structures are shown at a range of angles (Figure 1.11 (a), (b)). We observed that at angles of incidence equaling 77.5° and 72.5° for structure 1 and 2 respectively, the wafer appears dramatically warmer compared with smaller angles of incidence (10° and 45°), even though the actual temperature of the wafer is unchanged.

We plotted the measured directional emissivity for the two structures over the wavelength range between 7.5 µm and 13.5 µm as obtained through radiometry (Figure 1.11 (c),). Even though the measured emission by the detector is polarization averaged, the directionality of the thermal emission is clear. In agreement with the measurements, we observed that the emissivity is high between 70° and 82° for structure 1, and between 60° and 75° for structure 2, with a peak emissivity value of 0.28 for both structures. The peak directional emissivity is smaller relative to the p polarization directional emissivity data because the measurement is polarization-averagedit determines average emissivity over the entire 7.5µm - 13.5µm range of the detector. The detector's

range is 1.5 times larger than the designed wavelength range of operation of each structure. Despite this, a nearly 2:1 emissivity contrast was observed between normal and peak angles of incidence for both structures at 100°C and 110°C, respectively. Thus, even though the enabled directional control is in the p polarization, it enables a marked, and anomalous, contrast in the polarization-averaged thermal emission as a function of angle because the emissivity is minimal at all angles in the s polarization over the relevant broadband spectrum (Figure 1.4). This capability highlights immediate applications for near-normal incidence heat signature minimization while maintaining substantial radiative heat transfer at other angles of incidence.

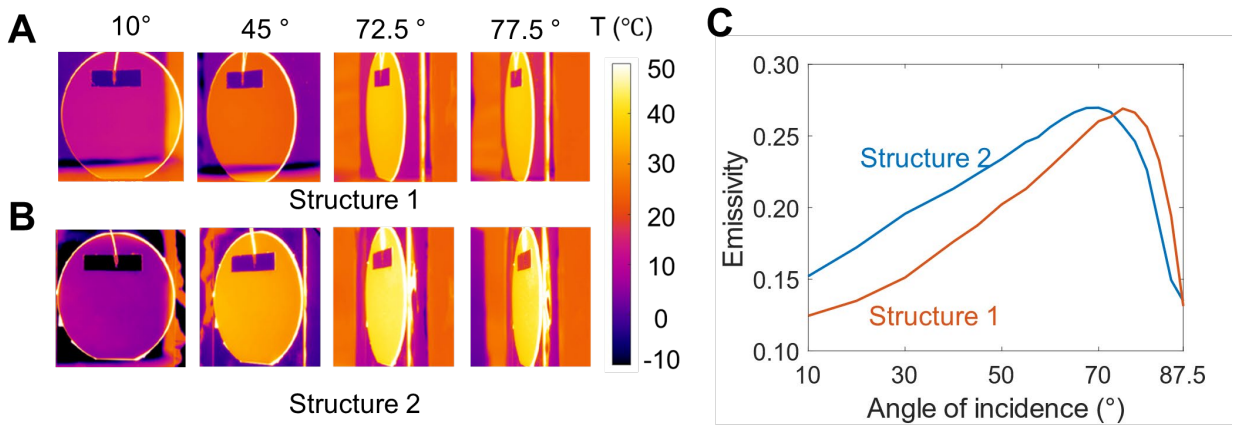

Figure 1.11. Radiometric measurements.(a) and (b) Thermal images of the fabricated $SiO_2/SiO/Al_2O_3$ and $Ta_2O_5/TiO_2/MgO$ multilayer photonic thin film structure. At the angle of incidence equals 77.5° and 72.5° for the two structures respectively, the wafer appears warmer compared with the angle of incidence is at 10° and 45° even though the actual temperature of the wafers maintains the same. (c) Inferred average directional emittance by radiometrically derived temperature measurements over the 7.5-13.5 μm detector wavelength range for the two thermal emitter structures, at different angles of incidence.

In Figure 1.12 we show an image of five identical wafers of our structure 1 ($SiO_2/SiO/Al_2O_3$) lying atop a low-emissivity metal support outdoors. We observe a strong angular contrast between reflective and emissive modes. The closer the wafer is to the camera the smaller the angle of incidence is, and thus these wafers appear colder to the thermal camera, and appear similar to the background support, a low-emissivity metal. The wafer which is the farthest away from the camera has the largest angle of incidence relative to the camera, and thus shows a warmer temperature due to its higher angular emissivity, and contrasts strongly with the low-emissivity metal support, which reflects the sky and thus appears cold. This capability highlights immediate applications of the developed material for near-normal incidence heat signature control while maintaining significant radiative heat transfer at large angles.

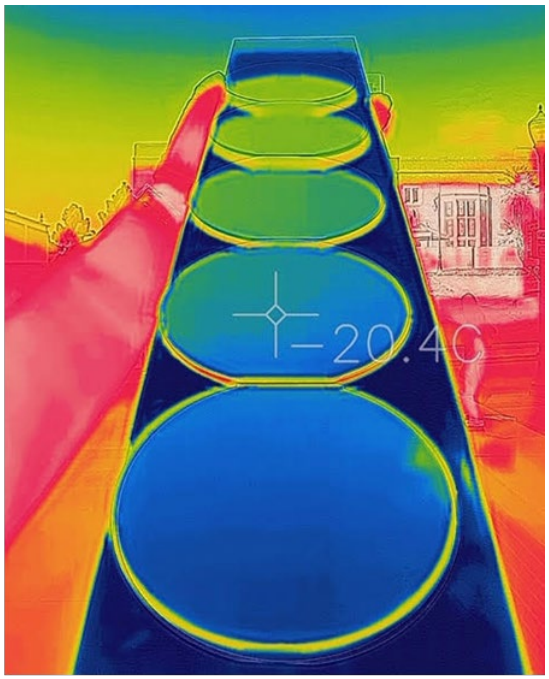

Figure 1.12. Thermal image of 5 identical fabricated wafers of structure 1 in an outdoor setting. The further the wafer is the larger the angle of incidence to the thermal camera is, which

gives the farthest wafer the highest emissivity. The metal support, which is low emissivity and reflecting the sky, looks cold to the camera regardless of the angle of view

1.5 Summary

We have proposed and experimentally demonstrated that gradient ENZ materials enable broadband directional control of thermal emission and absorption. Our utilization of conventional oxides in fabricating our gradient ENZ films makes this approach immediately useful for large-area heat transfer applications for near-room temperature applications, because they are low-cost and amenable to well-established manufacturing processes. We emphasize that the temperature and wavelength ranges of operation can be tailored by material choice, for instance using indium tin oxide (ITO) [32,36] at near-infrared wavelengths, but needs careful examination of the temperature dependence of the material's permittivity. While our approach enables angular selectivity in the p polarization, higher total radiance can be achieved through simultaneous broadband angular selectivity in the s-polarization using effective epsilon- and mu-near-zero (MNZ) materials [45,46] which might be developed using a metamaterial approach. Alternatively, using gradient ENZ materials alone already delivers broad spectrum, directional polarized light, a distinct capability which may itself be useful for a range of sensing and device applications. Our results suggest different opportunities to leverage the capabilities of gradient ENZ materials and the optical modes they support for broadband applications. In particular, we believe that these effects may have near-term impact on heat transfer and energy applications, including directionality control for radiative cooling [24], thermophotovoltaics [47], and nascent approaches to waste heat recovery from radiative sources [48]. More broadly, these results highlight that by decoupling angular and spectral response in photonic nanostructures, and different capabilities can emerge for how materials emit and absorb light.

Chapter 2 Realizing broadband directional thermal emitters using gradient doped III-V semiconductors

From Chapter 1 we already learned how to leverage polariton-supporting materials such as the metal or semiconductor oxides to realize gradient ENZ materials for broadband directional thermal emitter. However, limited by the materials choice and the non-continuous permittivity variations between those different polariton materials, we hypothesized that more continuous and better control over emitted thermal radiation can be achieved by using doped III-V semiconductors where we can more precisely control their permittivity and ENZ frequency by doping at different levels.

2.1 Introduction

Doped semiconductors have been explored in the context of thermal emitters. In fact, decades ago, infrared quantum cascade lasers have utilized highly doped semiconductors for surface plasmon polariton-based mode confinement[49]. Surface plasmon polariton mediated selective thermal emission from patterned doped silicon with $\varepsilon<0$ has been observed[50], and further studies of highly doped silicon have demonstrated surface plasmon polariton excitation across a wide range of the mid-IR[51,52].

Highly doped III-V semiconductors have also been used to demonstrate epsilon-near-zero behaviors. The first electrical modulation of thermal emission in far-IR was demonstrated by tuning the epsilon-near-zero (ENZ) mode in a single AlGaAs/GaAs/AlGaAs quantum well[53]. This study coupled an inter-sub-band transition and a surface phonon-polariton resonance, and thus, the ENZ effect is limited to a narrow wavelength range[54]. Thermal emission ranging from 3.5 to 8.0 micron from thin epitaxially grown In(Ga)Sb layers in InAs(Sb) matrices was demonstrated by

optically pumping this material with 980-nm pulse laser[55]. More recently, electrical modulation of thermal emission is realized by controlling the plasma frequency of the doped III-V semiconductor under applied bias[56–58]. However, those applications are rather narrow banded and functioning only around the plasma frequency of those doped semiconductors leaving the broadband application unexplored.

Here in Chapter 2, we employ the doped InAs to realize the theoretical gradient ENZ film framework we put forward in Chapter 1, to achieve a broadband directional thermal emitter.

2.2 Drude model and carrier concentration

The optical response of a doped semiconductor can be modeled using the Drude formalism:

$$\varepsilon(\omega) = \varepsilon_s\left(1 - \frac{\omega_p^2}{\omega^2 + i\omega\Gamma}\right),\ \omega_p^2 = \frac{ne^2}{\varepsilon_s\varepsilon_0 m^*} \tag{2.1}$$

where Γ is the scattering rate for carriers in the semiconductor, ω_p is the plasma frequency of the doped material, determined by m^*, the effective mass of the free carriers in the semiconductor, n the free carrier concentration of the semiconductor, and ε_o and ε_s, the permittivity of free space and the relative permittivity of the bulk, undoped semiconductor, respectively. For traditional semiconductors, the transition from positive to negative real part of the permittivity can be pushed to wavelengths as short as ~4μm by combining high doping and small effective mass, while highly-doped transparent conducting oxides have been demonstrated to behave as plasmonic metals across the telecom wavelength range (~1.5μm)[59] .

We extract the measured permittivity of Si doped InAs from the literature[60], and fit the variables in the Drude model according to the experimental data, shown below:

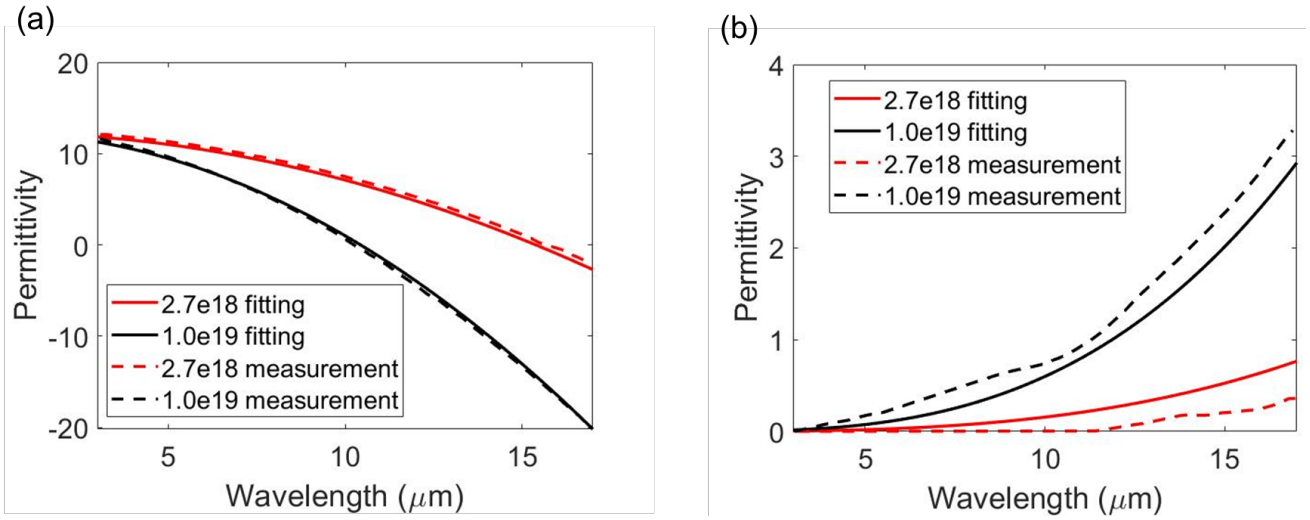

Figure 2.1. Wavelength-dependent (a) real and (b) imaginary parts of the permittivity of different doped InAs, calculated from the modeled fits of the experimental reflection data from the as-grown samples using the Drude model.

In the Figure 2.1, we plotted the permittivity of the Si doped InAs predicted by our fitting and the experimental measurement. We can see the fitted Drude model agrees well with the measurement. In the next sessions, we will use this model to calculate the permittivity of the doped InAs we used in this study.

2.3 Numerical study of gradient doped InAs

In this session, we numerically study the emissivity spectrum varying with angle of incidence and wavelength of the different gradient doped InAs. We investigate the total thickness effect of the InAs film on the emissivity angle and the doping level range of the film on the emissivity wavelength range.

2.3.1 Film thickness vs. high emissivity angle

In Figure 2.2, we plotted the permittivity of different Si doped InAs films: doping varies from 2.0 to 4.5e18cm^{-3}. We can see the ENZ wavelength of those InAs film changes across from 12.5 to 15 μm as the doping level changes (Figure 2.2(a)). The imaginary part of the permittivity is all below unity at different doping levels and wavelengths (Figure 2.2(b)), which together with the real part of the permittivity, will make a good gradient ENZ film structure if we combine those films together and make it a grade doped InAs.

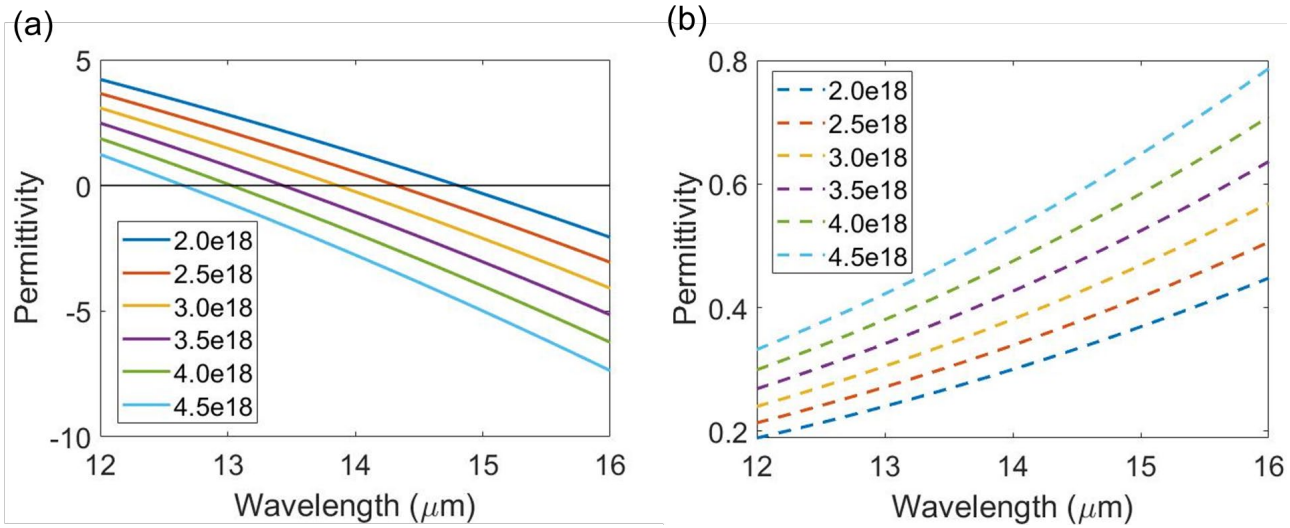

Figure 2.2 Calculated permittivity of the doped InAs: doping level range from 2.0e18 to 4.5e18cm^{-3}. (a) real part of the permittivity, (b) imaginary part of the permittivity

We propose a thin film stack as shown in Figure 2.3(a), from top to bottom the doping concentration of the InAs varies from 4.5 to 2.0e18cm^{-3} with an increment of 0.5e18cm^{-3}. Each doping layer has a same thickness, and we investigate three different thicknesses for those layers of the gradient thin film stack. There is a heavily doped InAs with a doping concentration of

5.0e19cm^{-3} with a 300nm thickness is underneath those layers. This heavily doped InAs layer will serve as a reflective mirror.

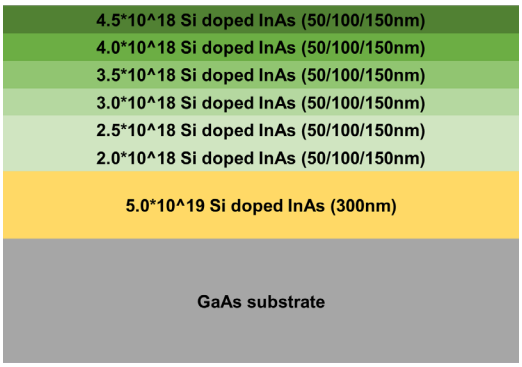

Figure 2.3 Schematic illustration of the gradient doped InAs film structure

Figure 2.4 shows the emissivity spectrum for p polarization varies with angle of incidence and wavelength of three different thickness stacks of Si doped InAs we proposed. We can clearly see the high emissivity angle is moved towards normal incidence as the thickness of the thin film increases.

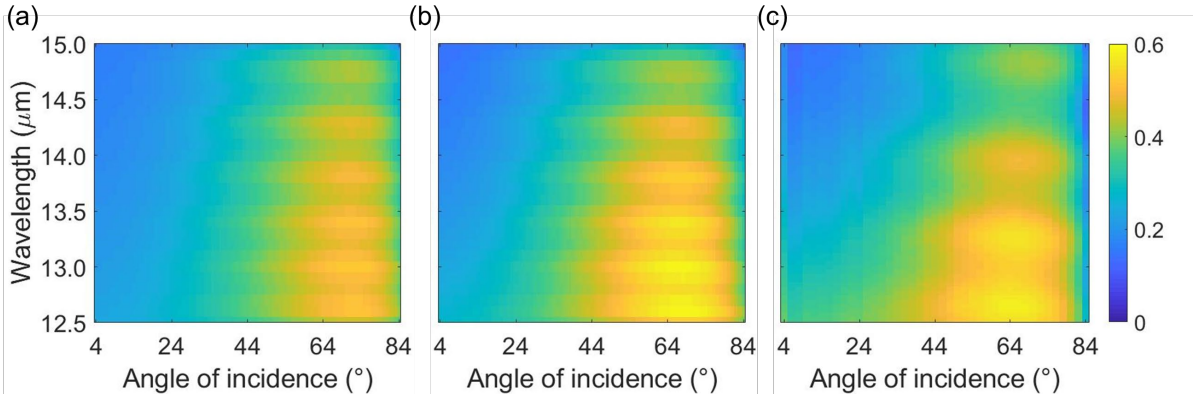

Figure 2.4 Emissivity spectrum for p polarization varies with angle of incidence and wavelength of three different thickness stacks of Si doped InAs: (a) 50nm thick each layer, (b) 100nm thick each layer, (c) 150nm thick each layer.

2.3.2 Doping range vs. high emissivity wavelength range

Then we studied another gradient doped InAs film with a completely different doping level range from 1.0e18 to 1.9e18cm^{-3}. Figure 2.5 shows the permittivity of different Si doped InAs films: doping varies from 1.0 to 1.9e18cm^{-3}. We can see the ENZ wavelength of those InAs film changes across from 18.5 to 19.5 μm as the doping level changes (Figure 2.5(a)). The imaginary part of the permittivity is all below unity at different doping levels and wavelengths (Figure 2.5(b)).

We make a grade doped InAs as shown in Figure 2.6 from top to bottom the doping concentration of the InAs varies from 1.9 to 1.0e18cm^{-3} with an increment of 0.1e18cm^{-3}. Each doping layer has a same thickness of 30nm making the total thickness of the gradient film 300nm. This way we can compare this directional emitter's working wavelength range with the film whose doping level varies from 4.5 to 2.0e18cm^{-3} with a thickness of each layer 50nm (same total thickness). There is also a heavily doped InAs with a doping concentration of 5.0e19cm^{-3} with a 300nm thickness underneath serving as a reflective mirror. The schematic demonstration of this film is shown in Figure 2.6.

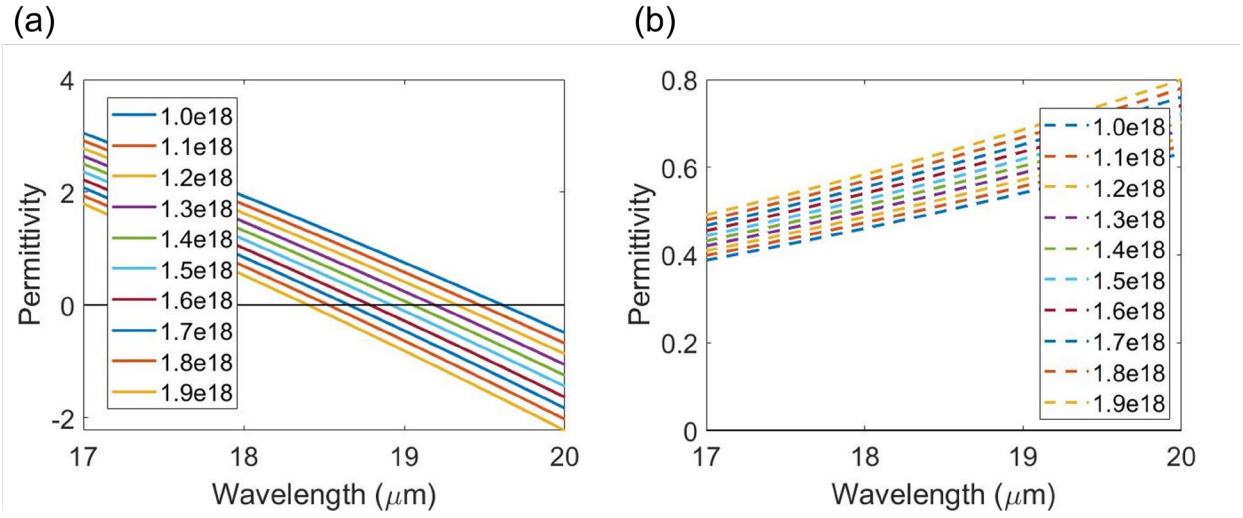

Figure 2.5 Calculated permittivity of the doped InAs: doping level range from 1.0e18 to 1.9e18cm^{-3}. (a) real part of the permittivity, (b) imaginary part of the permittivity

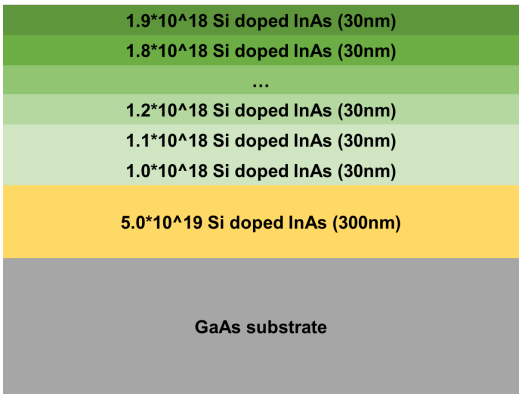

Figure 2.6 Schematic demonstration of the gradient ENZ film where the doping level varies from 1.9 to 1.0e18cm^{-3}

Figure 2.7 shows the emissivity spectrum for p polarization varies with angle of incidence and wavelength of the two different gradient doped semiconductor stacks. We can see the first film with a doping level varies from 4.5 to 2.0e18cm^{-3} shows a high emissivity from 12.5 to 15μm while the second film with a doping level varies from 1.9 to 1.0e18cm^{-3} exhibits high emissivity from 17.5 to 19.5μm. From these results, we can see by just changing the doping level of the semiconductor, we can tune the thermal emitter's working wavelength to a completely different region without seeking for new materials sets as what we did in Chapter 1.

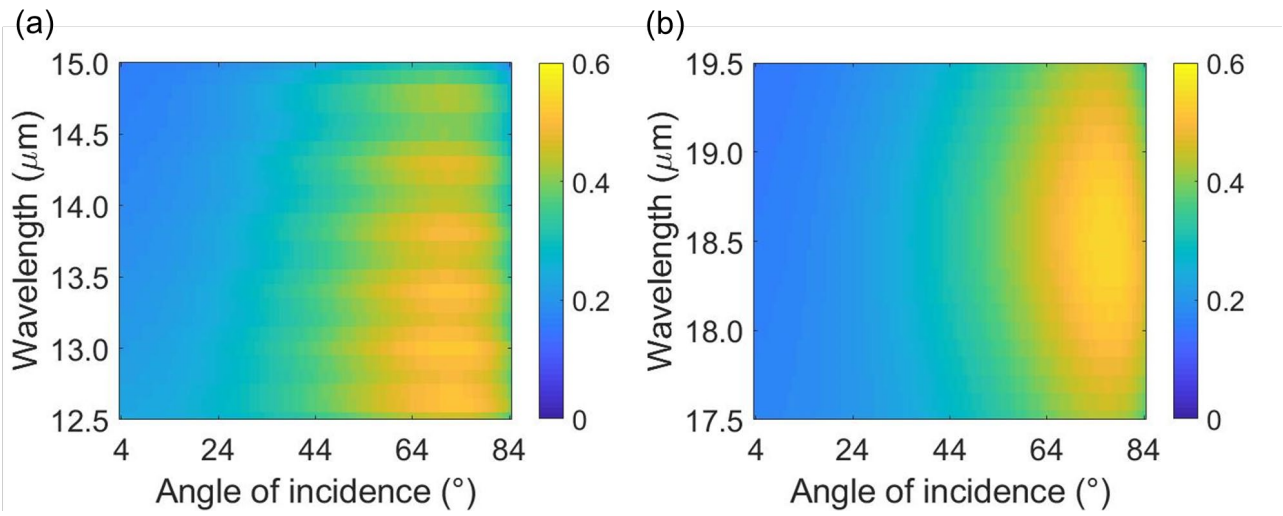

Figure 2.7 Emissivity spectrum for p polarization varies with angle of incidence and wavelength of two stacks of Si doped InAs: (a) doping level varies from 4.5 to 2.0e18cm^{-3}, (b) doping level varies from 1.9 to 1.0e18cm^{-3}

2.4 Experimental realization of gradient ENZ using InAs

In this session, we experimentally fabricate three gradient doped InAs film grown by Molecular Beam Epitaxy (MBE) and we characterized the fabricated films by a FTIR mapping the emissivity of those films varying with the angle of incidence and wavelength.

2.4.1 MBE growth of the gradient doped InAs film

Molecular beam epitaxy (MBE) is a term used to denote the epitaxial growth of compound semiconductor films by a process involving the reaction of one or more thermal molecular beams with a crystalline surface under ultra-high vacuum conditions. MBE is related to vacuum evaporation but offers much improved control over the incident atomic or molecular fluxes so that

sticking coefficient differences may be taken into account and allows rapid changing of beam species[61].

Molecular beam epitaxy (MBE) technique was developed by Cho and Arthur in early 1970s[61,62]. Figure 2.8 shows the cross section of a typical MBE system[58]. This technique involves interaction of one or several molecular or atomic beams on a surface of a heated crystalline substrate. MBE system consists of effusion cells with each cell containing one ultra-pure element. Each cell is covered with a shutter. For growing a film, effusion cells are heated to evaporate the source material and the shutters are utilized to control the thickness of the films. Further details about an MBE system can be found in reference[63].

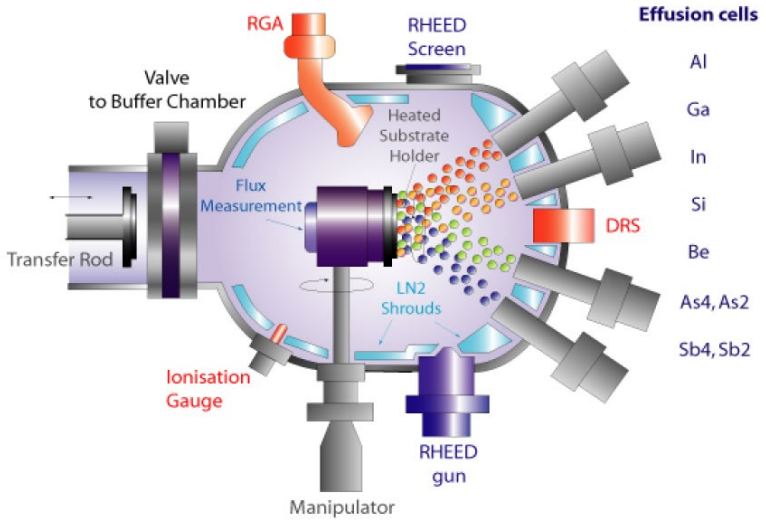

Figure 2.8: Schematic of a molecular beam epitaxy system[58]

The designed InAs structures with different n-type (si) doping layers were grown by a solid-source VEECO Gen-930 molecular beam epitaxy (MBE) (shown in Figure 2.9), in which a valve-controlled arsenic cracker is equipped to provide As_2 flux and a 400cc SUMO cell for indium was operated with a higher tip temperature to reduce defect density caused by indium spitting. All

the InAs layers are grown on epi-ready semi-insulating GaAs (100) substrates. Single-side polished GaAs wafers are used to prevent the Fabry-Perot interference seen in double-side polished substrates.

Prior to the InAs growth, the oxide desorption process for the GaAs (100) substrates was carried out under an As_2 flux of 5×10^6 Torr at a substrate temperature of 600 °C. The substrates were then decreased to 580 ºC for 50 nm GaAs buffer layer growth at a GaAs growth rate of 0.33mL/s. After buffer growth, the GaAs substrate was maintained at 600 °C for 10 minutes under As_2 flux to smooth the surface. Subsequently, the substrate temperature was decrease to 410 ºC for the growth of InAs layers. The InAs growth rate was fixed at 0.5mL/s and the As/In flux ratio was controlled to be 1.2~1.5. After the growth of InAs, the same As_2 flux on the surface was continued until the substrates cooled down to 325 °C. Then As_2 flux was stopped and the sample was taken out from the MBE growth chamber at about 275 ºC. During the wafer growth, the reflection high energy electron diffraction (RHEED) was utilized to calibrate the GaAs and InAs deposition rates, as well as to calibrate the As/In flux ratio.

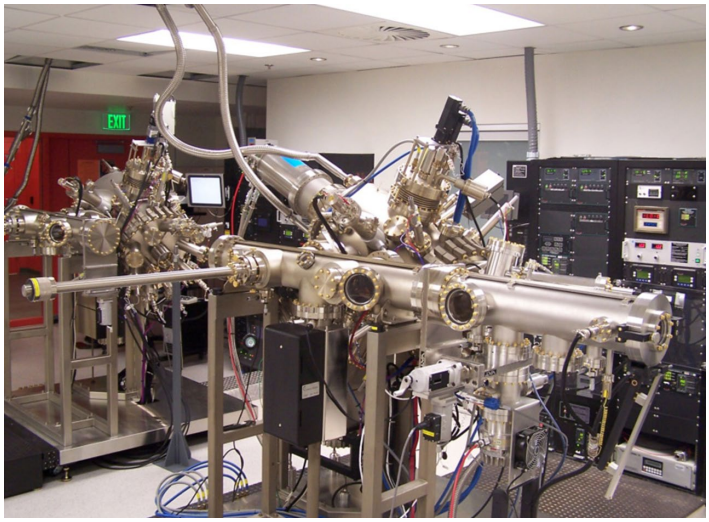

Figure 2.9 Veeco GEN -930 MBE systems used in this study

2.4.2 Optical characterization of the doped InAs film

The optical characterization is realized by FTIR as we use in Chapter 1. By Kirchhoff's law, the absorptivity of an object is equal to its emissivity or each frequency and angle of incidence when in thermal equilibrium. Since our structures were deposited on an optically thick metal layer, the transmissivity (T) is equal to 0. Thus, to infer emissivity (ε), we measure reflectivity (R) as a function of polar angle of incidence, and plot it as $\varepsilon = 1 - R$.

Fabricated samples were characterized by a Bruker Invenio-R Fourier-transform infrared spectrometer (FTIR) with a Harrick Seagull variable angle reflection accessory. An inserted wire-grid polarizer is used to selectively transmit linearly polarized light (p and s polarization namely) to the sample for measurements. Our measurements are made by establishing background reflectance from a well-calibrated reference mirror first for each measurement. The reflectivity spectra were measured for different incidence of angles from 4° to 84° at 2° increments.

2.4.3 Comparison between numerical results and experimental measurement

We fabricated three InAs thin film samples. First one has a doping level range from 2.0 to 4.5e18cm^{-3} with a thickness of 50nm each layer, and second one has a doping level range from 2.0 to 4.5e18cm^{-3} with a thickness of 150nm each layer, and a third one with doping level range from 1.9 to 1.0e18cm^{-3} with a thickness of 30nm each layer. Figure 2.10 shows one of the fabricated InAs thin film on a 2 inch GaAs wafer (the one which has a doping range from 1.9 to 1.0e18cm^{-3} with a thickness of 30nm).

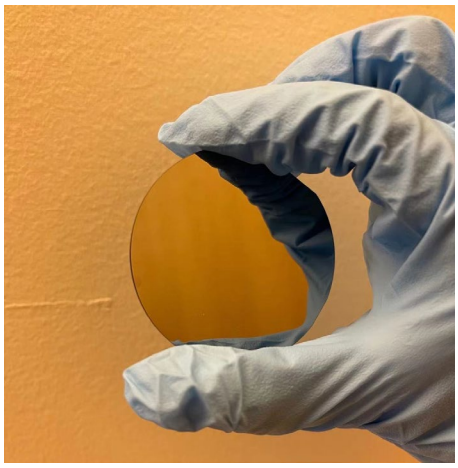

Figure 2.10 Fabricated InAs thin film on a 2 inch GaAs wafer (doping range from 1.9 to 1.0e18cm^{-3} with a thickness of 30nm each layer)

By comparing the first and second sample, we can observe the thickness effect on the high emissivity angle of those thermal emitters, while comparing the first and the third sample, we can see by changing the doping concertation range, the high emissivity wavelength range will change (first sample and third sample have the same total thickness).

First, we look at the comparison between the experiment and the simulation results for the first sample (Figure 2.11). We can see the experimental result show the emissivity spectrum is more continuous than the simulation. The reason can be during the MBE growth, the doping concentration change is more gradual and the diffusion between different doping layers can happen. We can also see by having grade doped semiconductor to realize broadband thermal emitter, we get smoother and more continuous high emissivity compared with using the combination of different polariton materials. Figure 4.12 shows the comparison between the experiment and the simulation results for the second sample.

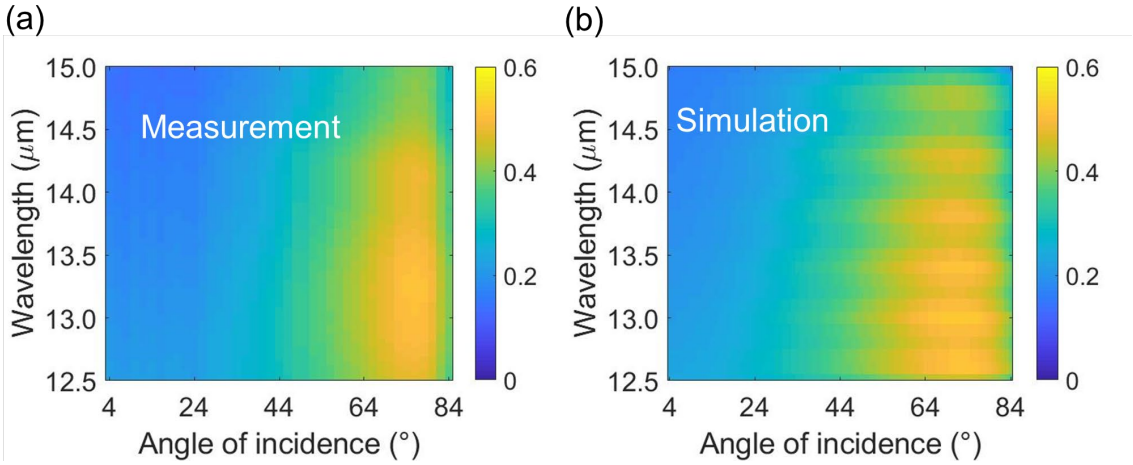

Figure 2.11 Emissivity spectrum for p polarization varies with angle of incidence and wavelength of first stack of Si doped InAs: (a) experiment, (b) simulation.

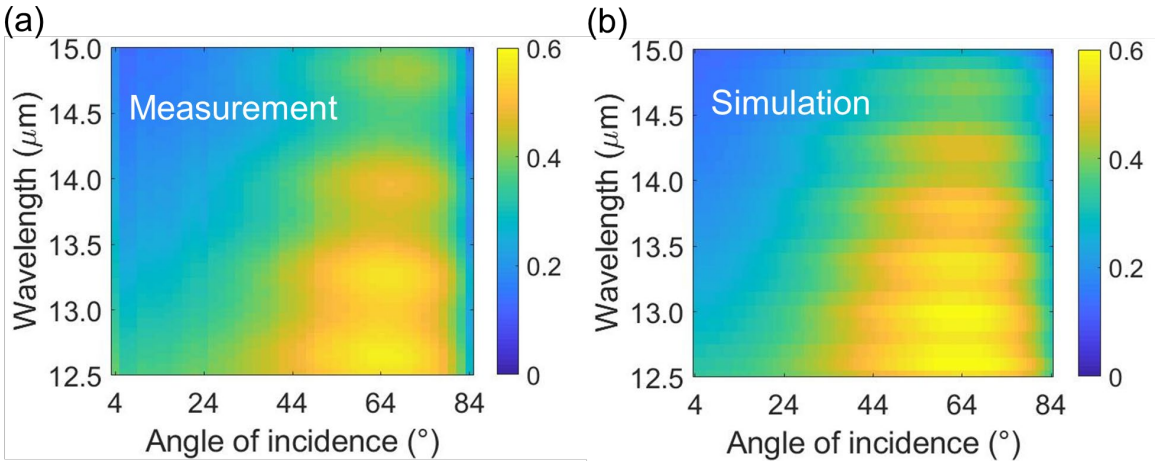

Figure 2.12 Emissivity spectrum for p polarization varies with angle of incidence and wavelength of second stack of Si doped InAs: (a) experiment, (b) simulation.

Then we plot the polar plot (Figure 2.13) of the averaged emissivity over 12.5-15μm of the two InAs thin films with different thickness (first sample 50nm each layer, and second sample 150nm each layer). The red curve is the averaged emissivity between 12.5 and 15μm of the InAs film with a 50nm thickness for each doping level and the black curve is the averaged emissivity of

the film with a 150nm thickness for each doping level (both in p polarization). We can see the highest average emissivity of the 50nm thickness sample happens around 75°, while the highest emissivity angle is 68° for the 150nm thickness sample. This is in corresponding to what we observed in Chapter 1 that as the total thickness of the gradient ENZ film increases, the high emissivity angle also moves towards the normal incidence.

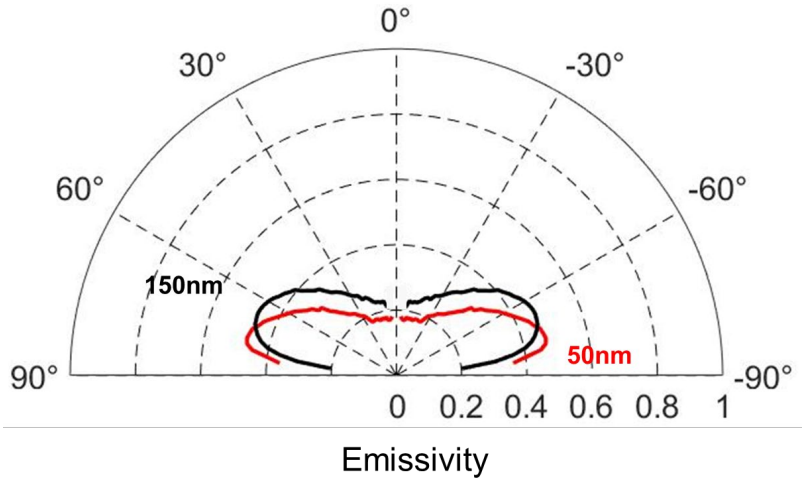

Figure 2.13 Comparison between two different thickness InAs thin films: red curve is the averaged emissivity between 12.5 and 15μm of the first InAs film with a 50nm thickness for each doping level and the black curve is the averaged emissivity of the second film with a 150nm thickness for each doping level (both in p polarization)

In order to show the different high emissivity wavelength range of two InAs samples (sample 1 and sample 3) with different doping lever range, we plot the emissivity across 10-20μm at the 76° angle of incidence. Figure 2.14 shows the emissivity of the two InAs thin films with different doping levels. The red curve is the emissivity across 10-20μm for the InAs film with a doping level from 4.5 to 2.0e18cm^{-3} and the blue curve is the emissivity of the film with a doping level from 1.9 to 1.0e18cm^{-3} both at the 76° angle of incidence. We can see the high emissivity

wavelength range of sample 1 is between 12.5 to 15μm, while the high emissivity wavelength range for sample 3 is between 17.5 to 19.5μm. We again verify using the experimental results that by changing the doping level of the semiconductor, we can tune the directional thermal emitter's functional wavelength to a different range without seeking for different new materials. Figure 2.15 shows the measured emissivity spectrum in p polarization for the sample 1 and sample 3.

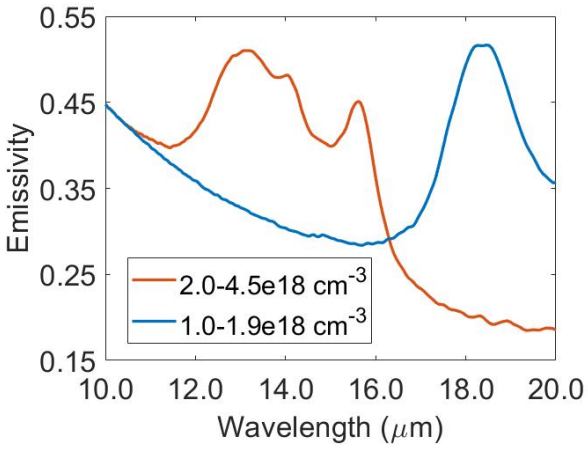

Figure 2.14 Comparison of the emissivity in p polarization between two different doping level InAs thin films

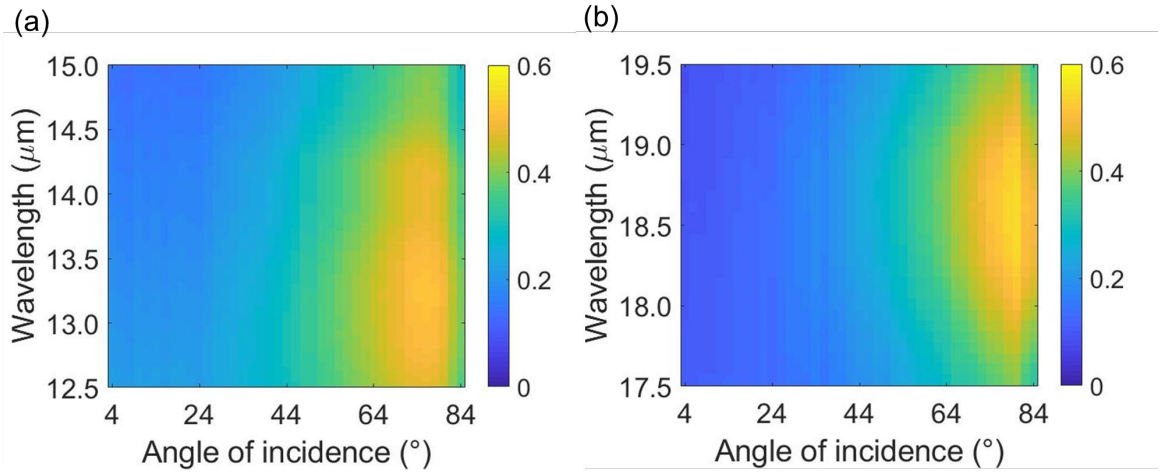

Figure 2.15 Comparison of the emissivity spectrum in p polarization between two different doping level InAs thin films: (a) doping level varies from 4.5 to 2.0e18cm^{-3}, (b) doping level varies from 1.9 to 1.0e18cm^{-3}

2.5 Summary

In this Chapter we use Si-doped InAs to realize broadband directional thermal emitters in the infrared wavelength range using the gradient ENZ thin film framework we put forward in Chapter 1. We first used the Drude model fitted the permittivity of the InAs at different doping levels. We then conducted simulation using transfer matrix method characterizing the emissivity of the different InAs films. It is found that the gradient doped InAs film doped from 2.0 to 4.5e18cm^{-3} with 0.5e18 cm^{-3} increment and a thickness of 50nm each doping lever, has high emissivity >0.5 between 64° and 84° across the wavelength range of 12.5-15μm. When we increase the thickness of each doping level layer to 150nm, the high emissivity angle moved to 50°-70°, which agrees with what we observed in Chapter 1 that increasing the total thickness of the gradient ENZ thin film the high emissivity angle will move towards normal incidence. Finally, we fabricated another InAs film which has totally different doping level (1.0 to 1.9e18cm^{-3}) and observe this sample has a different functional wavelength of 17.5 to 19.5um. The measurement results agree well with the simulation data.

Future work may investigate the dynamic tunability of the emissivity of the doped semiconductors using electrical bias. More specifically, by leveraging the rectification property of a Schottky contact between the metal and the semiconductor, carrier accumulation and depletion can happen which will lead to a plasma frequency change and eventually a permittivity variation.

Chapter 3 Quasi-bandgap behavior in non-Hermitian photonic crystals

Non-Hermitian photonic crystal system has increasingly drawn the attention of researchers, while majority systems of those are parity-time ($\mathcal{PT}$) symmetric systems which require balanced presence of gain and loss. Here, we investigate another type of non-Hermitian photonic crystal which only contains loss and the lossy material has the same real part of permittivity as the lossless material. We characterize the band structure as well as the reflection response in both 1D and 2D non-Hermitian system. We discover that by introducing a small amount of loss in the crystal while maintaining the real part of permittivity of the lossy material equals to the permittivity of lossless material, a quasi-bandgap purely induced by loss opens up at the band edge. An ultra-sharp reflection peak within the quasi bandgap in both 1D and 2D non-Hermitian photonic crystals we proposed. Furthermore, we put forward a design of selective reflector which consists a traditional 2D photonic crystal waveguide and a non-Hermitian photonic crystal. This selective reflector can guide light along the waveguide and have the light absorbed by the non-Hermitian part while only the light with certain wavelength can be reflected back.

3.1 Introduction

Decades of research in photonic crystals has resulted in a rich understand of the physical mechanisms and unique behaviors they make possible for controlling the propagation of light[64–67]. Due to these capabilities have become an indispensable technology across the entire field of optical physics, especially in fiber optics and waveguides[68–71].

The paraxial equation of electromagnetic wave propagation in a photonic crystal is defined by[72]

$$i\frac{\partial E(x,z)}{\partial z} = \left[-\frac{1}{2k_0 n_0}\frac{\partial^2}{\partial x^2} + V(x)\right]E(x,z) \equiv HE(x,z) \tag{3.1}$$

where the propagation distance z along the optical axis plays the role of time, $E(x,z)$ is the transverse component of the electric field, $\mathrm{k_0}$ is the free-space wavevector and $\mathrm{V(x)} \simeq \mathrm{n_s} - \mathrm{n(x)}$ is the optical potential, with background index of $\mathrm{n_0}$. A Hermitian Hamiltonian $\mathcal{H}$ corresponds to a real potential $V(x)$, while a non-Hermitian Hamiltonian $\mathcal{H}$ corresponds to a complex potential $V(x)$, i.e., to a complex refractive index distribution $n(x)$. As is well known, the imaginary part of the refractive index corresponds to optical gain or loss of the dielectric medium.

While majority applications of photonic crystals demand no loss or ultralow loss in the crystal which means a Hermitian system, there is now significant interest in studying the non-Hermitian photonic crystal systems for applications in laser and signal[73,74]. Hermitian operators can only describe ideal systems. However, non-conservative elements (e.g., radiation losses, material absorption) are ubiquitous in the realistic world. For example, when light propagates in media with a complex refractive index, the system is non-Hermitian[75,76].

The most studied non-Hermitian system is the parity-time[77–92]. The Hamiltonian $\mathcal{H}$ is said to be $\mathcal{PT}$ symmetric if it commutes with the $\mathcal{PT}$ operator, i.e., $[\mathcal{H}, \mathcal{PT}] = 0$. For Eq. 3.1, $\mathcal{PT}$ symmetry implies $\mathrm{V(-x)} = \mathrm{V^*(x)}$, i.e., the real (imaginary) part of the potential should be an even (odd) function under space reflection $\mathrm{x} \rightarrow -\mathrm{x}$. This means that a $\mathcal{PT}$ symmetric optical potential requires a balanced distribution of gain and loss in the medium. While conceptually appealing, the experimentally realized $\mathcal{PT}$ symmetric system is only limited in 1D waveguide system[93–100] or deliberately designed 2D systems[73,101,102]. In general, non-Hermitian system with the presence of only loss is a more common scenario and has not received enough attention.

Previous studies about polaritonic photonic crystals or lossy photonic crystals[103–105] are essentially systems contain two materials with completely different permittivity.

In this paper, we investigate both 1D and 2D non-Hermitian photonic crystal system with the lossless material and the lossy material have the same real part of permittivity ($\epsilon_1 = \epsilon', \epsilon_2 = \epsilon' + \epsilon''$) and characterized their band structure as well as reflection response. One note to be made here is, the lossy and lossless materials are not assumed to be derived from the same materials. According to the Kramers–Kronig relations[106], one cannot change a material's imaginary permittivity without changing the real part permittivity. Thus, the lossy and lossless material referred here are two different materials which happen to have the same real permittivity over a wavelength range of interest but different imaginary permittivity values such as AlSb[107] and InSb[108]. They both have the real part permittivity equal 15 at 0.63 μm while AlSb is transparent and lossless, while InAs has an imaginary permittivity of 3.5i.

We discovered that by just having a small imaginary permittivity part in the lossy material while maintaining the real permittivity part equals to the permittivity of the lossless material, a quasi bandgap emerges. Within this quasi bandgap, a ultra-sharp reflection peak is obtained in both 1D and 2D non-Hermitian photonic crystal we proposed. The occurrence of this reflection peak is counter-intuitive as it is purely induced by the adding small amount of loss in a lossless bulk material in a photonic crystal setting. In the end, we designed a selective reflector which is made of a lossless 2D photonic crystal waveguide and a non-Hermitian photonic crystal. This selective reflector can guide light along the waveguide and only reflect light at certain wavelengths while the rest of the light is absorbed via the non-Hermitian part. This type of waveguide will be inspiring for some imaging and sensing applications[90,109–114].

3.2 1D reflection

We first consider the behavior of the 1D non-Hermitian photonic crystal shown in Figure 3.1 (a). This multi-layer thin film consists of alternating layers of materials (orange and green) with different permittivities ($\epsilon_1 = 2, \epsilon_2 = 2 + 2i$), with a spatial period of a and $d_1 = 0.8a, d_2 = 0.2a$. Each layer is uniform and extends to infinity along x and y direction.

Figure 3.1 (b) shows the reflectivity of the 1D non-Hermitian photonic crystal when $\epsilon_1 = 2$, $\epsilon_2 = 2 + 0.5i$, $2 + 1i$ and $2 + 2i$ respectively. A reflectivity peak of 0.57 is observed at frequency equals 0.35, and a weaker reflectivity peak of 0.27 at frequency equals to 0.71 for all three curves of different ϵ_2. We see the reflectivity peak value is not reduced with the decrease of Im[ϵ_2]of the lossy layers. In contrast, as Im[ϵ_2] becomes smaller, the peak gets sharper.

We then calculated the bandstructure of this 1D non-Hermitian photonic crystal by solving the following equation:

$$cos(ka) = cos\left(\frac{n_2\omega}{c}d_2\right)cos\left(\frac{n_1\omega}{c}d_1\right) - \left(\frac{n_1^2+n_2^2}{2n_1n_2}\right)sin\left(\frac{n_2\omega}{c}d_2\right)sin\left(\frac{n_1\omega}{c}d_1\right) \qquad 3.2$$

Eq. 3.2 is solvable through inversion for wavevector k if frequency ω is given and for ω if k is given. If the frequency is assumed to be real, the resulting wavevector is complex and the wave decays in space, while when the wavevector is assumed to be real the resulting frequency is complex and the real wavevector excitation decays away in time.

The two solutions are only identical when ϵ is real. We plot the real component of the solutions assuming either real frequency or real wavevector in Figure 3.2 (c). The colored curves are the

solution for real wavevector and the black thinner lines are the solutions for real frequency. We can see near the band edges, the two methods produce different results. When k is real, We can clearly observe two bandgaps where no solution for Eq. 3.2 exists within these frequency ranges: one is around frequency at 0.35 and the other one around frequency at 0.71 which correspond to the two reflectivity peaks we see in Figure 3.1 (b). However, the band structure solved by assuming real frequency is a continuous line, with a solution lying somewhere within the Brillouin zone for all frequencies. Nevertheless, the real wavevector and real frequency bands show excellent agreement in the middle of the Brillouin zone.

Figure 3.1 (d) shows the zoomed-in first and second bands. Here we can see more clearly that there is a quasi bandgap between the first and second band solved by real wavevector. The reason we are calling it a quasi bandgap is because the band structure solved by assuming real frequency is continuous without any gap.

The imaginary part of the first three bands solved by assuming real wavevector has low and high values at the band edge (in Figure 3.1 (e)). This means the wave experiences either high loss or low loss at different orders of eigenfrequency. To show the slow light at the band edges, the inverse group velocity $(\mathrm{d}\omega/\mathrm{dRe[k]})^{-1}$ obtained from the real frequency solutions is shown in Figure 3.1(f). We can see the inverse group velocity increases significantly as near the quasi bandgap region.

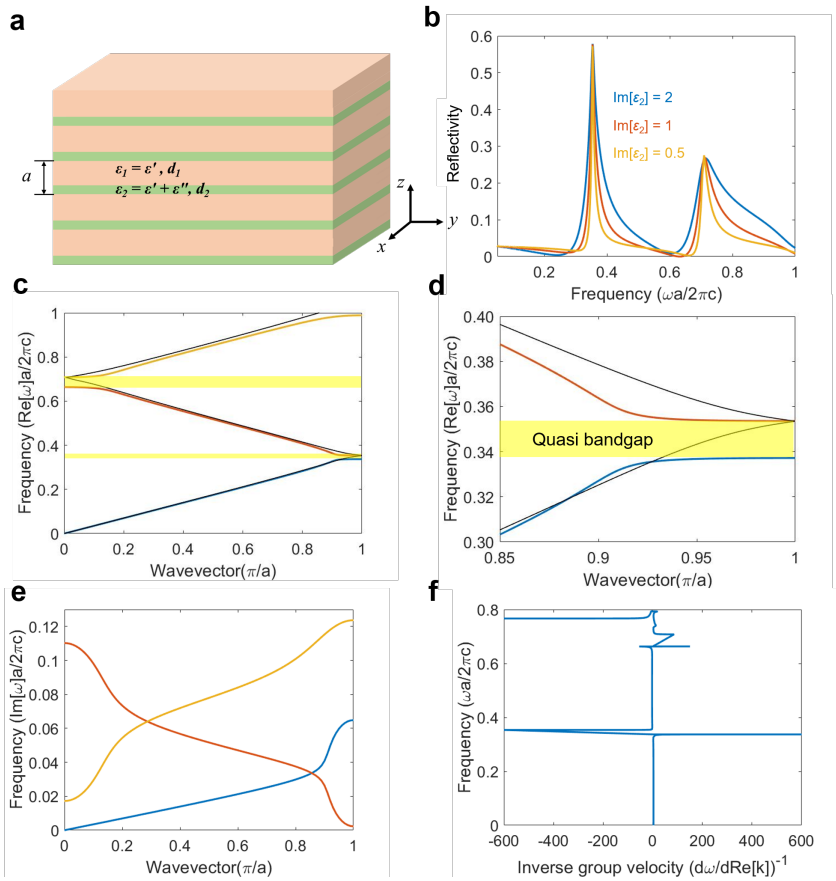

Figure 3.1 Reflection of the 1D non-Hermitian Photonic Crystal system: (a) schematic diagram of the 1D non-Hermitian photonic crystal, (b) reflectivity for three different permittivities of the lossy layers. A reflectivity peak of 0.57 is observed at frequency = 0.35, (c) real part of the band-structure for the 1D photonic crystal calculated from assuming real wavevector (colored lines) and real frequency (thin black lines). Note the presence of bandgaps is only when the wavevector is purely real, (d) the zoomed in first and second band where we can see more clearly the presence of a quasi bandgap around frequency = 0.35, (e) Imaginary bandstructure for the 1D non-Hermitian photonic crystal assuming real wavevector, (f) Inverse group velocity which is also known as the density of states defined by $(\mathrm{d}\omega/\mathrm{dRe}[\kappa])^{-1}$ calculated from assuming the real frequency.

3.3 Perturbation theory

After seeing the quasi bandgaps purely induced by loss in the 1D non-Hermitian photonic crystal, we seek the explanation to the emergency of those quasi bandgaps by perturbation theory. Perturbation theory, a class of techniques to find the effect of small changes on known solutions to a set of equations, is as important a tool for classical electromagnetism as it is for quantum mechanics and other fields[114]. Not only does it allow one to apply the computational efficiency of idealized systems to more realistic problems, or to study effects too small and weak to be easily characterized numerically, but it also provides a window of analytical insight into complex systems otherwise accessible only via opaque numerical experiments. First order perturbation theory has been readily used in low loss perturbed photonic crystal systems to predict the imaginary eigenvalue change from lossless unperturbed systems[64]. Surprisingly, the higher order of perturbation theory for electromagnetism has rarely remarked upon the real part change of the eigenvalue for a loss perturbed photonic system. In this section, we will employ both first and second order of perturbation theory for the generalized electromagnetic wave eigenvalue problem to predict both the imaginary and real bandgap size for the 1D non-Hermitian photonic crystal we proposed in Section 2. There are a number of ways in which Maxwell's equations can be written as a generalized eigenproblem, for the electric field with time dependence $e^{-i\omega}$ in a source-free linear dielectric $\epsilon(r)$:

$$\nabla \times \nabla \times E(r) = \left(\frac{\omega}{c}\right)^2 \epsilon(r) E(r) \tag{3.3}$$

where we use the Dirac notation of basis-independent state. Assuming that $\epsilon(r)$ is purely real and lossless and positive, then this eigenproblem is Hermitian and positive semidefinite,

leading to real ω solutions. Since it is a generalized eigenproblem, the eigenstates are orthogonal under the inner product.

To apply perturbation theory, one must have some small parameter δ characterizing the perturbation, in our case it will be the $\Delta\epsilon$ (an imaginary permittivity change). The new eigensolutions are expanded in powers of $\Delta\epsilon$ (See Supplementary Materials). The first-order correction from a perturbation $\Delta\epsilon$ is then easily found to be:

$$\Delta\omega^{(1)} = -\frac{\omega^{(0)}}{2}\frac{\langle \boldsymbol{E_n^{(0)}}|\Delta\epsilon|\boldsymbol{E_n^{(0)}}\rangle}{\langle \boldsymbol{E_n^{(0)}}|\epsilon_0|\boldsymbol{E_n^{(0)}}\rangle} + O(\gamma^2) \qquad 3.4$$

Where $\Delta\omega^{(1)}$ is the first order correction for the perturbed eigenvalue, $\omega^{(0)}$and $\mathrm{E_n^{(0)}}$ are the unperturbed eigenvalue (eigenfrequency) and eigensolution (electric field).

Similarly, second order perturbation theory can be recast as exact expressions for 2^{nd}order derivatives of the eigenvalue. Eq. 3.5 is the second order correction to the perturbed eigenvalue of the 1D non-Hermitian photonic crystal (See Supplementary Materials):

$$\Delta\omega^{(2)} = \frac{\omega^{(0)}}{2}\left[-\frac{\langle \boldsymbol{E_n^{(0)}}|\Delta\epsilon|\boldsymbol{E_n^{(0)}}\rangle}{\langle \boldsymbol{E_n^{(0)}}|\epsilon_0|\boldsymbol{E_n^{(0)}}\rangle} + \left(\frac{\langle \boldsymbol{E_n^{(0)}}|\Delta\epsilon|\boldsymbol{E_n^{(0)}}\rangle}{\langle \boldsymbol{E_n^{(0)}}|\epsilon_0|\boldsymbol{E_n^{(0)}}\rangle}\right)^2 + \sum_{\substack{j=1 \\ j\neq n}}^{N} \frac{\lambda_n^{(0)}}{\lambda_n^{(0)}-\lambda_j^{(0)}} \frac{\langle \boldsymbol{E_j^{(0)}}|\Delta\epsilon|\boldsymbol{E_n^{(0)}}\rangle}{\langle \boldsymbol{E_j^{(0)}}|\epsilon_0|\boldsymbol{E_j^{(0)}}\rangle} \frac{\langle \boldsymbol{E_n^{(0)}}|\Delta\epsilon|\boldsymbol{E_j^{(0)}}\rangle}{\langle \boldsymbol{E_n^{(0)}}|\epsilon_0|\boldsymbol{E_n^{(0)}}\rangle}\right] \qquad 3.5$$

Then we assume the electric field is $E^{(0)} = cos(\pi x/a)$ and $E^{(0)} = sin(\pi x/a)$ for any two sequential bands and we plug those expressions in to Eq. 3.4 and 3.5, to calculate the bandgap size at the the band edges:

The imaginary bandgap size is calculated from the first order (see Supplementary Materials):

$$\Delta\omega^{(1)} = -\frac{\omega^{(0)}}{2}\frac{\Delta\epsilon}{\epsilon_0}\left[\frac{1}{\pi}sin\left(\frac{2\pi d}{a}\right)\right] \quad 3.6$$

The real bandgap size is calculated from second order perturbation (see Supplementary Materials):

$$\Delta\omega^{(2)} = \frac{\omega^{(0)}}{2}\left[\frac{\Delta\epsilon}{\epsilon_0}\left(\frac{2d}{\pi a}sin\left(\frac{2\pi d}{a}\right)\right)\right]^2 \quad 3.7$$

We plot the bandgap size between the first and second band and the second and third band in Figure Perturbation (a) shows the imaginary bandgap size between the first and second band and (c) between the second band and third from 1st order perturbation theory. Both the perturbation theory and the simulation results show that the imaginary bandgap size grows linearly with the perturbation $\Delta\epsilon = \mathrm{Im}[\epsilon]$. Figure 3.2 (b) is the real bandgap size between the first and second band and (d) between the second and third band from 2nd order perturbation theory. We see the real bandgap rises when we introduce the perturbation (loss in the photonic crystal) and it has a parabolic growth with $\mathrm{Im}[\epsilon]$. The real bandgap size gets larger as $\mathrm{Im}[\epsilon]$ increases, which explains why the reflection peak gets less sharp at larger $\mathrm{Im}[\epsilon]$ in Figure 3.1 (b). In addition, in Figure 3.2, all perturbation theory prediction of the bandgap size agrees well with the simulation results and starts to derive as the $\mathrm{Im}[\epsilon]$ gets larger.

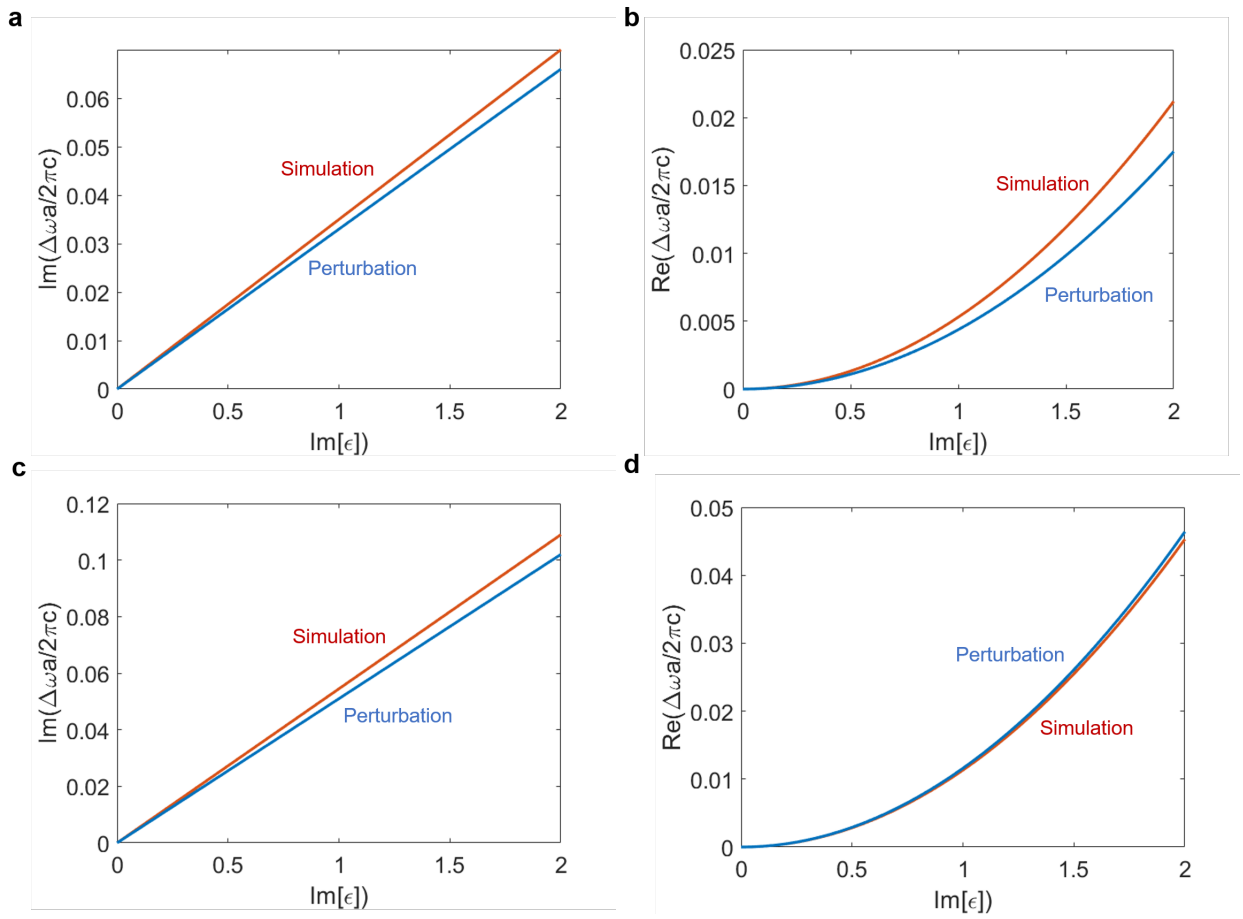

Figure 3.2 Perturbation theory prediction for the quasi bandgap size (a) imaginary bandgap size between the first and second band from 1st order perturbation theory and (b) real bandgap size between the first and second band from 2nd order perturbation theory, (c) imaginary bandgap size between the second and third band from 1st order perturbation theory and (d) real bandgap size between the second and third band from 2nd order perturbation theory

3.4 2D non-Hermitian photonic crystal

We can apply the insights we get from 1D non-Hermitian photonic crystal to a two-dimensional system. We consider a 2D non-Hermitian photonic crystal of lossy rods (r = 0.21a)

which have $\epsilon_2 = 2 + 2\mathrm{i}$ embedded in a lossless background $\epsilon_1 = 2$ in a square lattice (lattice constant a)as shown in Figure 3.3 (a).

In Figure 3.3 (b), we plot the TM bandstructure from $\Gamma - \mathrm{X} - \mathrm{M} - \Gamma$. We overlay with the dashed blue lines which are the bandstructure for the corresponding Hermitian or lossless photonic crystal (essentially a bulk material with homogeneous permittivity ϵ of 2). Compared with the bandstructure of the lossless crystal, the bands of the non-Hermitian photonic crystal are more complex where we see bands tend to split and merge more frequently at those vertices in the first reduced Brillion zone. To better characterize the bandstructure features of the non-Hermitian photonic crystal, we plot the first two bands at all combinations of $\mathrm{k_x}$ and $\mathrm{k_y}$ in Figure 3.3 (c) - real part of the bands and (d) imaginary part of the bands. As we can see from the Figure 3.3 (c), the first band and second band tend to merge at the band edge but there is still a gap at the end. On the other hand, different bands experience low loss or high loss at same k points shown in Figure 3.3 (d).

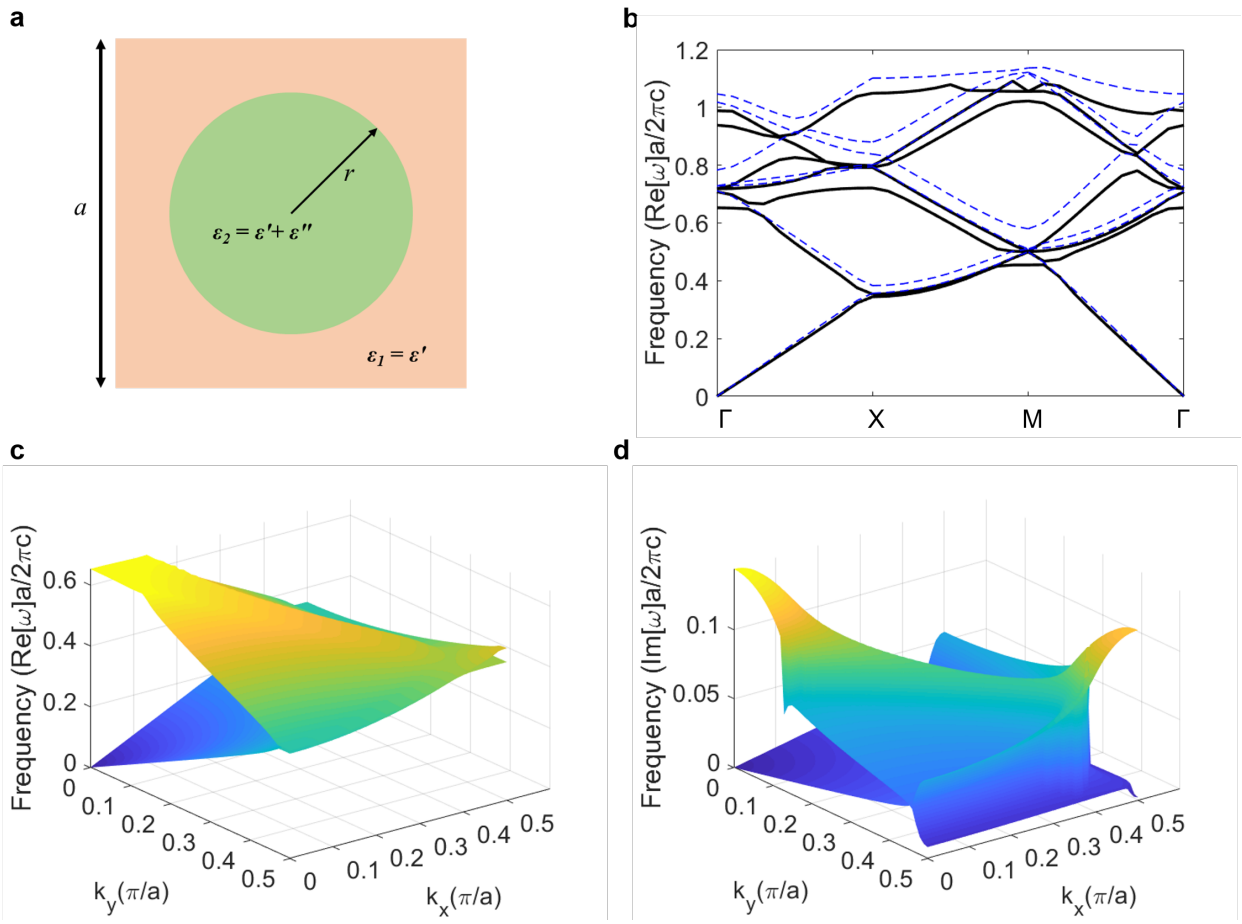

Figure 3.3 2D non-Hermitian photonic crystal (a) schematic diagram of 2D non-Hermitian photonic crystal with square lattice lossy rods (r = 0.21a, where a is the lattice constant) which have $\epsilon_2 = 2 + 2i$ in a lossless background $\epsilon_1 = 2$, (b) TM bandstructure from $\Gamma - X - M - \Gamma$ (dashed blue lines are the bandstructure for the corresponding Hermitian or lossless crystal with homogeneous permittivity of 2), (c) real part of the bandstructure at all combinations of k_x and k_y, (d) imaginary part of the bandstructure at all combinations of k_x and k_y

In Figure 3.4, we calculate the reflectivity of the 2D non-Hermitian photonic crystal for TM mode. The reflectivity has an astonishing sharp peak at frequency 0.35. The reflectivity is purely induced by the loss in the pillars and increases with the growth of the imaginary permittivity

Im[ϵ_2] of the lossy pillars and stabilizes when Im[ϵ_2] is greater than 0.5, which is similar to what we observed in the 1D photonic crystal. This peak is also located within the gap at the band edge between the first and the second band as we observed in Figure 3.3 (c). There is also a weaker peak around frequency 0.71.

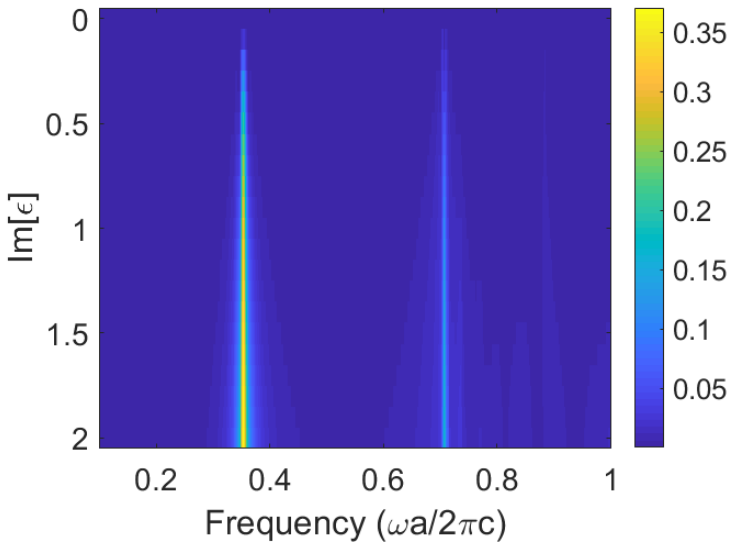

Figure 3.4 Reflectivity of the 2D non-Hermitian photonic crystal for TM mode at normal incidence. The reflectivity has a sharp peak at frequency 0.35 and a weaker peak at 0.71, which is similar to what we observed in the 1D photonic crystal

3.4 Waveguide application

We design a selectively reflective waveguide (Figure 3.5 (a)), which can allow a broad wavelength range of light passes through in the left part and gets absorbed in the right half while only light with a certain wavelength will be reflected back to the left. The left part of the selective reflector is a 2D photonic crystal with triangular array of air holes in a dielectric substrate ($\epsilon = 13$) with a relative radius r_1/a_1 of 0.48, where a_1 is the lattice constant of the photonic crystal. This photonic crystal has a linear defect (one row of air holes are removed from the crystal). The 2D

photonic crystal without the linear defect has a complete band gap with a midgap ratio being 16.3 %, which allows this waveguide to guide a wide range of light along the linear defect.

The right part of this reflector is a non-Hermitian square lattice photonic crystal with square array of lossy pillars ($\epsilon = 13 + 6i$) embedded in the lossless substrate with the same real part of permittivity as the lossy pillars' as well as the background of the left waveguide part ($\epsilon = 13$). The relative radius r_2/a_2 is 0.1, where a_2 is the lattice constant of the non-Hermitian photonic crystal. The non-Hermitian photonic crystal on the right is carefully designed so that it has a reflection peak (similar to what we observed in Figure 3.4) within the guided wavelength range of the waveguide on the left.

As shown in Figure 3.5 (b), the reflectivity of the combined selective reflector is ultra-low ($\ll 0.1$) at all wavelengths that passes through the waveguide on the left, except at the wavelength 1.077μm. The reflectivity dramatically reaches 0.43 at 1.077 μm. A 20-fold contrast is achieved compared with the reflectivity of the light far away from 1.077 μm. The transmission throughout the wavelength range from 0.9 μm to 1.2 μm is below 0.025. With absorption = 1 - reflectivity - transmission, we have majority of the light absorbed if not reflected by the non-Hermitian photonic crystal part, making it distinctive to a bragger mirror which can achieve selective reflecting while rest of the light passes through the mirror.

We show the out of plane electric field E_z distribution in Figure 3.5 (c) and (d) at two different wavelengths (1.13μm and 1.077μm respectively). At 1.13μm (Figure 3.5 (c)), the light is nicely guided along the 2D photonic crystal waveguide on the left and then penetrates into the non-Hermitian photonic crystal region where it experiences strong absorption within the first few columns of lossy pillars embedded in the substrate. While in Figure 3.5 (d) at the reflection peak

wavelength 1.077μm, we can see after the light passing though the left waveguide, it gets reflected immediately as it touches the non-Hermitian region and barely enters it. This is exactly what the light will behave (gets blocked and cannot propagate through) within a photonic crystal's bandgap. This observation further proves the presence of the quasi bandgap purely induced by loss in the non-Hermitian photonic crystal.

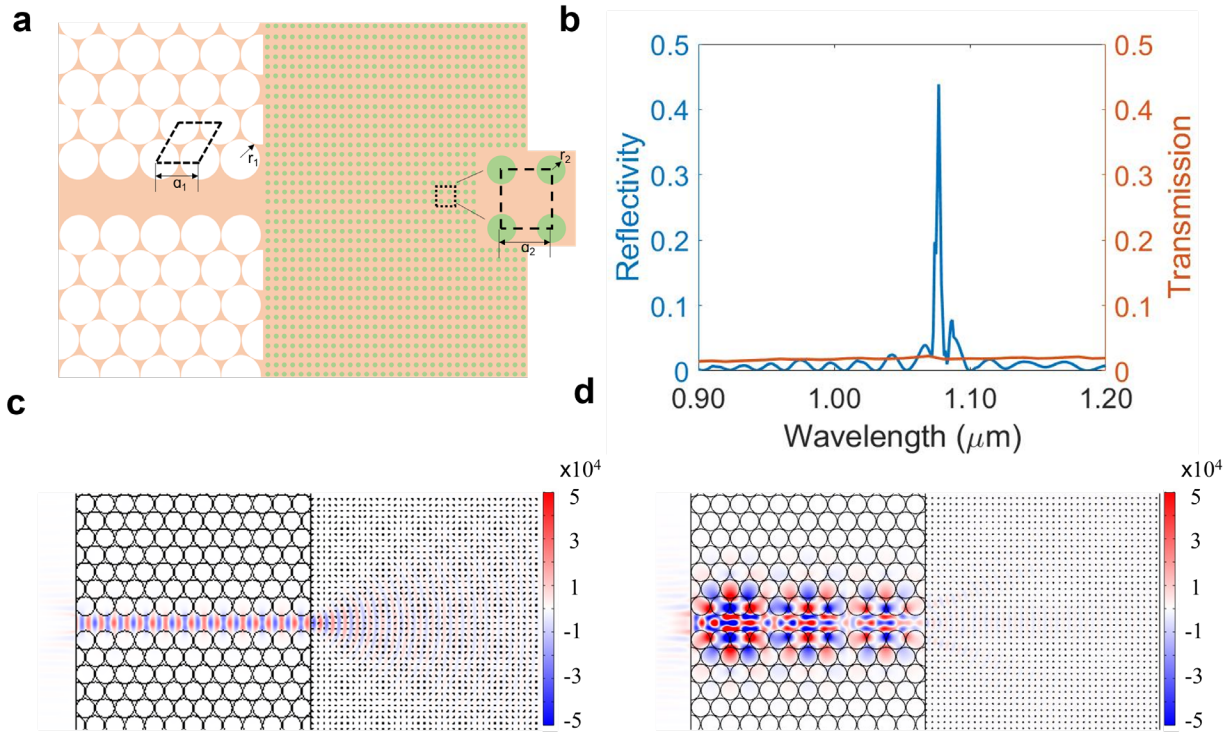

Figure 3.5 A selectively reflective waveguide (a) schematic diagram of the reflector: this left part of the selective reflector is a 2D triangular air hole photonic crystal with a linear defect. The right part of this reflector is a non-Hermitian square lattice photonic crystal with square array of lossy pillars ($\epsilon = 13 + 6i$) embedded in the lossless substrate with the same real part of permittivty ($\epsilon = 13$), (b) reflectivity and transmission of the combined selective reflector from 0.9μm to 1.2μm, (c) and (d) out of plane electric field E_z distribution at two different wavelengths 1.13 μm and 1.077μm respectively

3.5 Summary

In conclusion, we investigated a type of non-Hermitian photonic system where only contains loss and the lossy material has the same real part of permittivity as the lossless material. We discovered an quasi bandgap purely induce by introducing a small amount of loss in a lossless photonic crystal in both 1D and 2D systems. We also presented a formalism based on perturbation theory to understand the nature of this quasi bandgap.

Within the quasi bandgap, a sharp reflection peak is observed both in 1D and 2D non-Hermitian photonic crystals, which is counter-intuitive as this reflection is completely driven by small amount of loss in the photonic crystal. Leveraging this phenomenon, we designed a selective reflector which not only can reflect light of certain wavelength but also can absorb the rest. Ultimately, our analysis opens an distinctive area of non-Hermitian photonic crystal system.

Chapter 4 Controlling radiative heat flows in interior spaces to improve heating and cooling efficiency

Space heating and cooling in buildings account for nearly 20% of energy use globally with the goal of maintaining the thermal comfort of a building's human occupants. Currently, this is primarily achieved by keeping the interior air temperature at a setpoint. However, if one could maintain the occupant's thermal comfort while changing the setpoint, large energy savings are possible. Here we propose a mechanism to achieve these savings by dynamically tuning the thermal emissivity of interior building surfaces, thereby decoupling the mean radiant temperature from actual temperatures of interior surfaces. We show that in cold weather, setting the emissivity of interior surfaces to a low value (0.1) can decrease the setpoint as much as 6.5°C from a baseline of 23°C. Conversely, in warm weather, low emissivity interior surfaces result in a 4.5°C cooling setpoint decrease relative to high emissivity (0.9) surfaces, highlighting the need for tunability for maximal year-round efficiency.

4.1 Introduction

Energy consumption in residential and commercial buildings contributes to 30% of total greenhouse gas emissions worldwide [115]. In the United States, the buildings sector accounts for 41% of primary energy consumption, of which heating and cooling alone is responsible for over 35% [116]. Heating in particular poses a profound challenge for broader decarbonisation goals in temperate and cool climates [117]. With energy consumption for heating and cooling expected to grow dramatically worldwide in coming decades [118], improving the efficiency of these systems is a key part of mitigating climate change this century.

The goal of heating and cooling in buildings with human occupants is to maintain their thermal comfort [119]. Thermal comfort is both a quantitative and qualitative judgment that connects an individual's physiological and emotional perceptions of being in a thermally comfortable state [119,120]. While thermal comfort is typically assumed to be directly linked to the air temperature set point in a conditioned space, a human occupant's perception of comfort is subject to a range of other factors. These include material properties, metabolic heat production, heat transfer coefficients and radiative heat losses to external surfaces [121,122]. Human skin temperature is typically 33°C [123,124] in comfortable conditions, while the average heat generation rate of a standing adult is 70 W/m^2 [125,126]. Previous work has examined how temperature, air velocity and humidity affect thermal comfort [127–129]. Given the complex array of factors that influence the perception of comfort, and the pressing need for reducing energy use for heating and cooling, it is intriguing to note that an increase in the set point temperature for cooling, or a decrease in the set point for heating, by just 4°C can reduce energy use by up to 45 and 35% respectively[130].

In an indoor environment, where most people stay in a sedentary state, more than 50% of the heat generated by the human body is released through thermal radiation in the long-wave infrared part of the spectrum [131]. A recent experimental study used a membrane-assisted radiant cooling system to show that radiation and convection can be separated for comfort conditioning and, relying on radiation alone, thermal comfort can be maintained based on existing metrics even in unusually high ambient air conditions [132]. Radiative heat transfer between human occupants and their environment largely depends on the radiative properties of clothing, the walls and other surroundings. While significant progress has been made on insulation materials for walls, prior studies have primarily examined thermal conductivity, specific heat capacity and density[133–135].The effect of radiative heat transfer on thermal comfort has also been explored [136,137] but

remains a comparatively untapped mechanism for efficiency gains. One approach that has attracted considerable interest in recent years is tuning the radiative properties of clothing through photonic and materials-based strategies, making the clothing fabric more or less transparent to thermal radiation emitted from the human wearer, depending on weather conditions[138–145]. While conceptually attractive, this approach poses practical challenges, as it requires the human occupants of a conditioned space to wear specialized clothing depending on weather conditions. Thus, it is more practical to tune the radiative properties of the interior surroundings than to seek to alter the dressing habits of people who happen to be present in a particular building. In winter months, it has previously been noted that having a low emissivity wall could reduce the heat loss of a radiator in a room with no human occupant [146]. However, to the best of our knowledge, no study has examined how changing the long-wave infrared radiative properties of interior surfaces could reduce energy use for heating and cooling e, while maintaining the same thermal comfort level for human occupants. Here we propose and evaluate a untapped approach that seeks to make the environment *surrounding* the human occupants responsive to their radiative heat flows, to enable dramatically improved heating and cooling efficiency.

In cold weather conditions, lower radiative heat loss from the human occupant is desirable, as the air temperature could then be maintained at a lower temperature for the same level of thermal comfort. In these conditions it would thus be preferable to have low emissivity (high reflectivity) materials in the floor, ceiling and walls surrounding an occupant. By contrast, in summer or warm weather conditions, the heat generated by a human should be dissipated to interior surfaces, as these surfaces are typically colder than the clothing surface temperature. Thus, high emissivity (and low reflectivity) materials in the surroundings would be desirable. The desired radiative properties changing dramatically from low to high emissivity depending on weather conditions

and the heat load, will necessitate a different approach to enable maximal heating and cooling efficiency year-round. On the other hand, a small body of work over the past two decades has identified materials whose emissivity can be tuned in the long-wave infrared part of the spectrum relevant to room-temperature blackbody radiation, including by electrochromic control [147,148]. Most encouragingly, recent progress has yielded the first metal-free flexible IR electrochromic devices, based on conducting polymers that act as both the electrochromic material and electrodes [149–151], with good emissivity contrast, fast switching and durability demonstrated. Given these promising materials capabilities, here we investigate the concept of tunable emissivity surfaces for interior spaces in the built environment.

To evaluate the possible set point change and thus energy savings, we implemented computational fluid dynamics (CFD) simulations of an office environment with human occupants. In the simulations, we assume the emissivity of the inner walls can be tuned from that of a near blackbody to a very low value. We show that in cold weather conditions a decrease in the set point of 6.5°C is achievable if low emissivity (0.1) surfaces are used, relative to a baseline set point of 23°C when using conventional materials with a high emissivity (0.9). When multiple occupants are in the conditioned space a decrease of 8.2°C in the set point is possible. Conversely, in hot weather conditions, we show that a decrease in the set point of 2.3°C relative to a typical room set point of 26°C occurs if a low emissivity surface is used, highlighting the need for tunable emissivity surfaces. Following the CFD simulations, we conducted a detailed thermal comfort analysis for six different wall temperature scenarios. The mean radiant temperature (MRT) changes when we tune the emissivity of the walls, enabling lower or higher set points for heating and cooling respectively. A predicted mean vote (PMV) index further indicates that the set point change will not compromise the thermal comfort of human occupants in all six scenarios. We

extended our analysis to the building scale by using EnergyPlus [152–154] to evaluate the impact of the changed setpoints made possible by tunable emissivity surfaces on energy use on a typical summer and winter day in a temperate climate. In our preliminary analysis, we estimated that the lower setpoints made possible by low-emissivity interior surfaces in cold weather conditions can result in up to 36.8% (in Minneapolis, USA) and 34.1% (in Ancona, Italy) heating energy savings relative to conventional materials. In warm weather conditions however low emissivity interior surfaces are no longer appropriate and would result in a 34.7% (in Minneapolis) and 33.5% (in Ancona) energy penalty relative to high emissivity interior surfaces. Thus, tuning the interior surface's thermal emissivity enables maximal energy efficiency throughout the year, and in response to varying heat loads and conditions.

4.2 Concept of tunable emissivity interiors through the year in the building

The human body loses more than half of its heat through thermal radiation[136] in typical indoor environments. In cold weather conditions, finding a means to reduce this radiative heat loss in interior spaces is potentially an effective way to keep occupants comfortable at lower air temperatures than is typically maintained by heating. Most building materials, such as typical paints, wood or brick have high emissivity (and therefore absorptivity) in the long-wave infrared. Thus, interior surfaces typically absorb the thermal radiation from the human occupant and emit back a smaller amount of thermal radiation corresponding to the lower temperature of the walls, ceilings, and floors. Our goal for cold-weather conditions, schematically shown in Figure 1, is thus to have low emissivity, high reflectivity, interior surfaces. By virtue of this property, the surfaces will send back a larger fraction of the radiative heat lost by the human occupant back to them, allowing us to set the air temperature lower, thereby reducing the need for heating energy while

maintaining the same level of thermal comfort (which in our study is assessed by the maintenance of constant skin temperature and fixed amount of body heat released by the human occupant).

By contrast, in summer and warm-weather conditions more generally, it is desirable to maximize the net heat rejected by the human occupant to their environment (Figure 4.1). Thus, high emissivity (high absorptivity) materials in the interior of the building should be used to absorb the heat radiated by the occupant. By doing so one can maintain the same level of thermal comfort while using less cooling energy than it would be needed if the walls were low emissivity or high reflectivity. This qualitative introduction to our concept highlights a key result of our analysis: the need for tunability in the emissivity of the surfaces surrounding the human occupant, depending on weather conditions and overall heat loads.

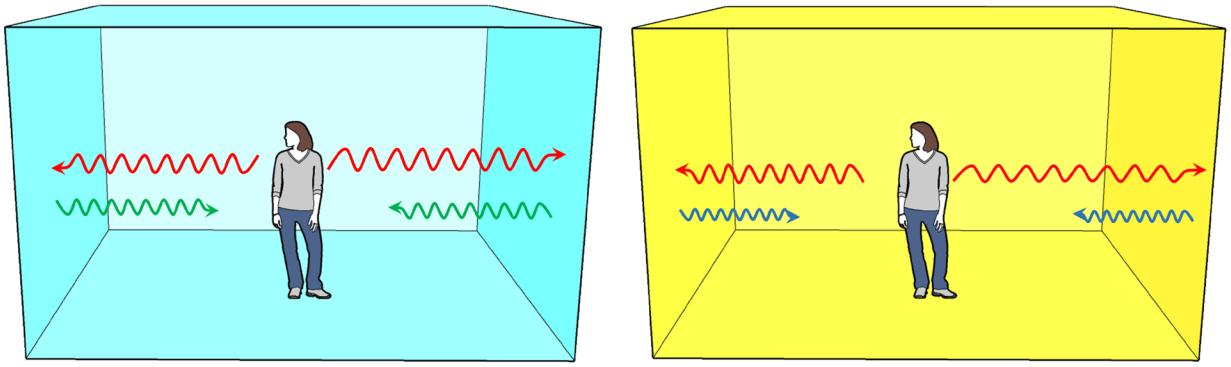

Figure 4.1: Conceptual schematic of tunable emissivity surfaces: Low-emissivity, high-reflectivity interior surface reflects radiative heat back to the body in cold weather conditions. By contrast, high emissivity and absorptivity interior walls absorb the radiative heat released from the occupant during warm-weather conditions

4.3 Computational Fluid Dynamics (CFD) study of tunable emissivity interiors in different scenarios in the building

4.3.1 Computational Fluid Dynamics (CFD) Modeling

ANSYS workbench mesh (v19.0) is used to generate the hexahedral dominated cutcell mesh for the whole domain, with a total number of 245284. The simulations are performed using ANSYS Fluent (v19.0). Steady state simulations for incompressible flows are implemented. The realizable k-ε model with standard wall functions is adopted to deal with turbulence. The DO (discrete ordinates) radiation model is used to calculate radiative heat transfer between the occupants and the wall, and the SIMPLE algorithm is adopted to deal with the coupling of the pressure and the velocity. The discretization of the convection term in all equations is the second order upwind scheme and for the diffusion term, the second order central scheme is used. We maintain the constant temperature of the occupants' skin and fixed heat released from them by changing the set point temperature of the room.

Coupled wall temperature model

In practice, the wall temperature can change due to indoor air temperature variation. We assume an outside air temperature of 5℃ in winter and 27℃ in summer and the wall temperature is both determined by the external and internal environment (walls have the thickness of 0.37m and the conductivity of 0.77W/(m·K) [155,156] and the external surfaces have a mixed boundary taking both convection (heat transfer coefficient of 21.6W/(m^2·K) [156] and free stream temperature of 5℃ and 27℃ respectively) and radiation (radiation temperature of 5℃ and 27℃ respectively and external emissivity of 0.9) into consideration as schematically shown in Figure S3 (a)). We

can see in winter as the indoor temperature decreases, the interior wall temperature also decreases from 14.4℃ to 12.3℃ (2.1℃ drop in winter as the emissivity varies), the set point change in winter can reach 3.6℃ when the emissivity of the wall changes to 0.1 from 0.9. 3.6℃ is a smaller change compared with our initial calculation which is meant to be a guidance of the highest potential set point change. However, a 3.6℃ set point change is still meaningful in terms of building energy saving. In summer, the temperature change is smaller due to the smaller difference between indoor and outdoor temperature.

Validation of the CFD model

We validate the numerical method implemented in this paper by comparing its results against experimental data previously. In their analysis, Chafi and Hallé built a model room equipped with ventilation system in the laboratory [157]. The room measures 4.88 m × 3.66 m and has a height of 3 m. Constant wall temperatures are maintained by flowing warm or cold through them in the experiment. There are 21 thermocouples installed in different horizon planes of 0.1m, 0.6m, 1.1m, 1,7m and 2.3m. The geometry of the model room is shown in Figure 4.2. All the boundary conditions in our numerical simulation are corresponding to the measurement data. The boundary conditions are shown in the Table 4.1.

Table 4.1. Boundary conditions in Validation. Velocity and temperature boundary conditions used in the validation.

Name	Boundary conditions
Grille1	Velocity inlet, v=1.02m/s, t=25.4℃
Grille2	Velocity inlet, v=1.38m/s, t=25.4℃
Radiant wall	t=12℃

Other walls	t=19℃
Floor and ceiling	t=19℃

Figure 4.3 shows the comparison between the experimental measurements and the CFD results in different positions. While there are measurable differences between the measurements and CFD predictions, they are below 5.3% at all positions. In summary, the numerical prediction from our CFD model agrees reasonably well with the published experimental measurements.

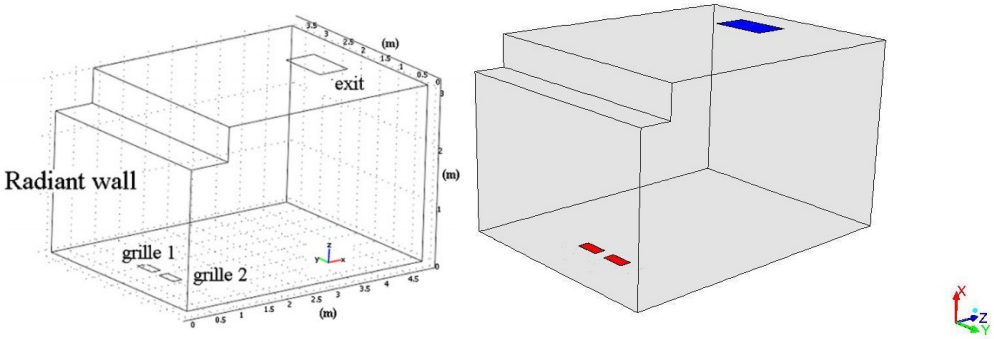

Figure 4.2. Validation model. Geometry of the model room: (a) the model use in the experimental study. (b) our computational model.

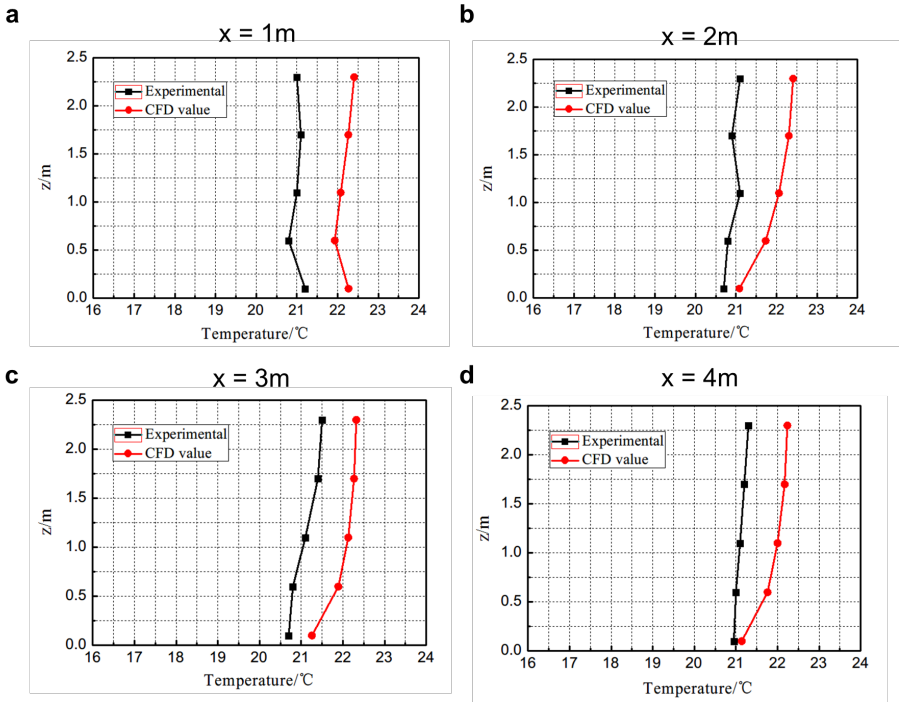

Figure 4.3. Comparison between the measurement and the CFD prediction in Validation. The air temperatures in the room at different heights.

Figure 4.4 shows the grid independence check for this numerical study. We refined the grid by doubling the grid number and compared the calculated average velocity results at different horizontal planes for the two grid systems (1) 245,284 cells and (2) 490,568 cells. The results showed that the grid density chosen was sufficient, as no significant difference was observed between the two grid systems.

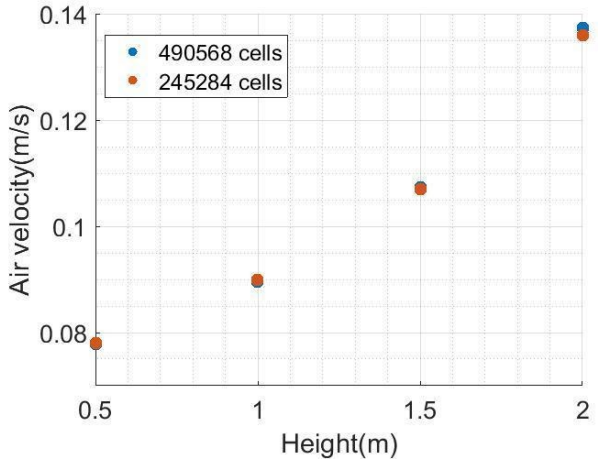

Figure 4.4. Grid independence. Average velocity results of different horizontal planes for the two analyzed grid mesh (1) 245,284 cells and (2) 490,568 cells.

4.3.2 Set-point change for the single occupant scenario

The indoor set point is the average air temperature in the room. Our goal is to assess how the set point will change in an air conditioned or heated room when we change the emissivity of the walls, floor and ceiling. We use the air inlet to deliver cooling or heating air in the room to

keep the human in a thermally comfortable state in a manner similar to what occurs in real indoor conditions. In our case we use the skin temperature staying at 33°C as a criteria for determining the air temperature that maintains the human occupant in a state of thermal comfort, given a particular set of radiative properties for the interior surfaces.

When we change the emissivity of the interior surfaces, the mean radiant temperature and the radiative heat transfer between the human and surrounding changes. In winter conditions, if we decrease the emissivity, the radiative heat loss is reduced, so it allows us to lower the air temperature and tolerate larger convective loss while maintaining the same skin temperature. In this way, we can have a lower heating air temperature from the air inlet to reduce heating energy input. If we don't introduce the heating or cooling air inlet and outlet to facilitate air flow into and out of the space, it is impossible to maintain the human's thermal comfort in different emissivity conditions. The average indoor air temperature change is not directly caused by the change in the emissivity of the walls. Rather, it is because when the emissivity of the walls is changed, the radiative heat loss from the human occupant is also changed, which gives us greater flexibility in changing the air temperature inside the room while maintaining ideal skin temperature. The amount of heat emitted by the human body is not large enough to significantly increase the room's temperature. The set point (air temperature) change in the room is thus mostly due to the change of the heating/ cooling air temperature from the inlet.

We now describe in detail the CFD simulation and analysis steps we take. Figure 4.5 schematically shows the process. We have six different scenarios (six different wall temperatures) to represent different weather conditions. The detailed CFD calculation boundary conditions including the air inlet velocity and temperatures in different scenarios have also been added in the Appendix B.

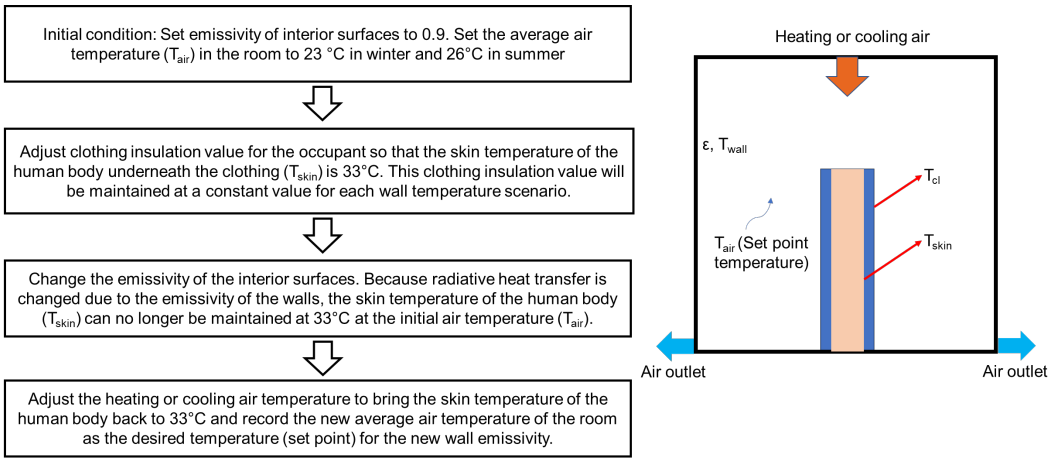

Figure 4.5. Calculating the relationship between set point temperature and surface emissivity. Flow of determining the emissivity of interior walls and set point relation.

To numerically analyze the impact of emissivity on the interior air temperature set point, we developed a 3D computational model (Figure 4.6 (a)) to simulate a standing person in a proto-typical conditioned space. The room, whose dimensions are 3 m × 3 m × 3 m, has an air inlet where heating or cooling air is supplied, and multiple outlets (shown in red) to ensure adequate distribution and flow of air in the space. The pathlines in Figure 4.6 (a) indicate the heating/cooling air enters from the inlet and the calculated mean air velocity in the room is 0.11 m/s (see Figure 4.7 for temperature and velocity distribution at different planes). We simulated different scenarios with the wall temperatures of the room (including side walls, ceiling, and floor) ranging from 13℃ to 25℃ to represent conditions one typically encounters from cold to warm weather scenarios.

The non-sensible heat loss by the human occupants includes the heat loss by respiratory and evaporation from skin, is calculated at 50% relative air humidity for all scenarios[41]. The metabolic rate of the standing adult in the room is 70W/m^2 [136]. When the emissivity of the walls is 0.9, a fixed set point of 26℃ in summer and 23℃ in winter is applied to the six different wall

temperature scenarios and the occupant's clothing insulation (enabled by the shell conduction function) is adjusted to have a skin temperature of 33℃ [158,159]. Then, the same clothing insulation is used throughout the same wall temperature scenario. As the emissivity of the interior wall changes, we adjust the air temperature to maintain a skin temperature of 33°C (with the same clothing insulation) to evaluate the effect of the emissivity on the set point. In the thermal comfort analysis section that follows, we also determine how the change in air temperature set point affects the human occupant's thermal comfort.

Figure 4.6 (b) shows the total radiative heat loss from the human occupant to the environment. The radiation between the occupant and the interior is suppressed as the emissivity of the walls is decreased at six different wall temperatures. In cold weather, reducing the radiative heat transfer is beneficial for keeping the human warm while in warm weather it sabotages the occupant getting rid of the heat. The radiative heat loss can be reduced by 23.7% and 24.2% respectively at the wall temperature of 13℃ and 15℃ when the emissivity decreases from 0.9 to 0.1. In contrast, reducing the emissivity from 0.9 to 0.1 suppresses more than 14% of heat releasing radiatively in warm weathers (when the wall temperature is equal to 23℃ or 25℃) (see Figure 4.8 for radiative and convective heat loss).

Figure 4.6 (c) shows the set point change as the emissivity of the interior varies in different wall temperature scenarios (for wall temperature coupled to external and internal environment scenario, see Figure 4.9 and see Figure 4.10 for the set point change results of an off-center positioned human occupant). We can see all the set point temperatures are at 26℃ in summer and 23℃ in winter when the emissivity is 0.9 in the six different wall temperature scenarios. As the emissivity starts to decrease, the set point must decrease to maintain the same skin temperature for the human occupant. The set point decreases when the emissivity is reduced because the occupant

tends to lose less heat radiatively as shown in Figure 4.6 (b), thereby allowing for more heat loss convectively to colder air. When the wall temperature is set to 13℃, a decrease of set point as large as 6.5℃ can be realized, which could yield meaningful energy savings (see the energy analysis session). In contrast when the weather is warm (wall temperatures at 23°C and 25℃), it is not favorable to have the emissivity of the walls low, because the cooling set point must be 3.6℃ and 2.3℃ lower respectively than it is when the emissivity of the walls is 0.9. These results highlight the need for tunability in the emissivity of interiors surrounding the occupant, depending on weather conditions.

A common trend we observed in Figure 4.6 (b) and Figure 4.6 (c) is that the rate of change of both the radiative heat loss and set point temperature reduction accelerates when the emissivity approaches 0. To understand why, we consider a simplified radiative heat transfer model for a human occupant and their surroundings that can be analytically evaluated. For a closed system consisted of two gray and diffuse surfaces, the radiative heat flux of the two surfaces can be analytically described as[160]:

$$Q_{1,2} = \frac{(E_{b1} - E_{b2})}{\frac{1-\varepsilon_1}{\varepsilon_1 A_1} + \frac{1}{X_{1,2} A_1} + \frac{1-\varepsilon_2}{\varepsilon_2 A_2}} \tag{4.1}$$

In the above equations, $Q_{1,2}$ is the heat flux, A_1 is the area of the hot surface, in this case is the surface of the human cloth and A_2 is the sum of the cold surfaces area, in this case is the surface of the interiors, E_{b1} and E_{b2} are the black body emission at the temperature of hot surface and cold surface respectively where $E_{b1} = \sigma T_1^4$, $E_{b2} = \sigma T_2^4$, σ is the Stephan-Boltzmann constant, T_1 is the hot surface temperature, T_2 is the cold surface temperature, ε_1 and ε_2 are the emissivity of the hot surface and the cold surface, X is the view factor.

When surface 1 is a plane or convex Eq. (4.2) can be simplified as [160]

$$Q = \frac{A_1(E_{b1} - E_{b2})}{\frac{1}{\varepsilon_1} + \frac{A_1}{A_2}(\frac{1}{\varepsilon_2} - 1)} \tag{4.2}$$

Eq. (4.2) can be used as a simplified way to calculate the radiative heat transfer between the occupant and their surroundings. From Eq. (4.2), we can further see when we decrease the emissivity of the cold surface the heat flux will be decreased as well. Eq. (4.2) also shows that as ε_2 approaches zero the impact of the denominator increases sharply, agreeing with previous observations about the impact of emissivity [146], which explains why we see an accelerated decrease of both radiative heat loss and set point temperature when the emissivity approaches 0.

In the CFD model we use the DO (discrete ordinates) radiation model to calculate the radiative heat transfer between the occupants and the walls. The DO radiation model solves the radiative heat transfer equation for a finite number of discrete solid angles, each associated with a vector direction fixed in the global Cartesian system. Radiative heat loss calculated from both CFD model and Equation (4.2) in six different wall temperature scenarios are shown in Figure 4.9. We can see that while the CFD model uses an effective numerical method to simulate the radiative heat transfer between the occupant and the surrounding, Eq. (4.2) still provides a good approximation for the radiative heat loss that is analytically tractable. The reason for this can be understood by the view factor calculation: $F_{1\text{-}2}A_1=F_{2\text{-}1}A_2$. Since the walls are all assumed to have the same temperature and $F_{1\text{-}2} = 1$, the view factor from the occupant to the surroundings is only associated with the ratio of the area of the two objects regardless of the position.

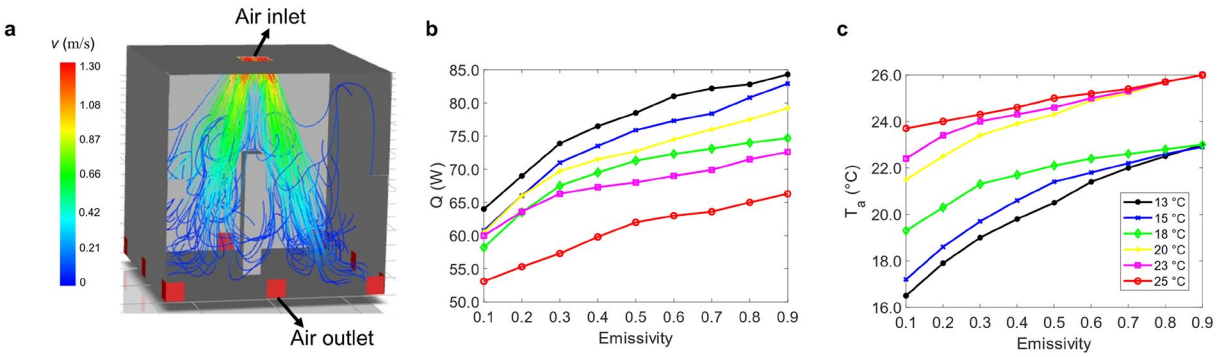

Figure 4.6: Computational model (a)**:** 3D model built to simulate a standing person in a conditioned space, to assess the impact of tuning the thermal emissivity of the spaces that surround the human occupant. (b) Radiative heat loss of the occupant varies with the emissivity of their surroundings, and is shown for six different wall temperature scenarios from 13°C to 25°C. (c) The set point temperature varies as the emissivity of the interior surfaces surrounding the human occupant goes from 0.9 to 0.1

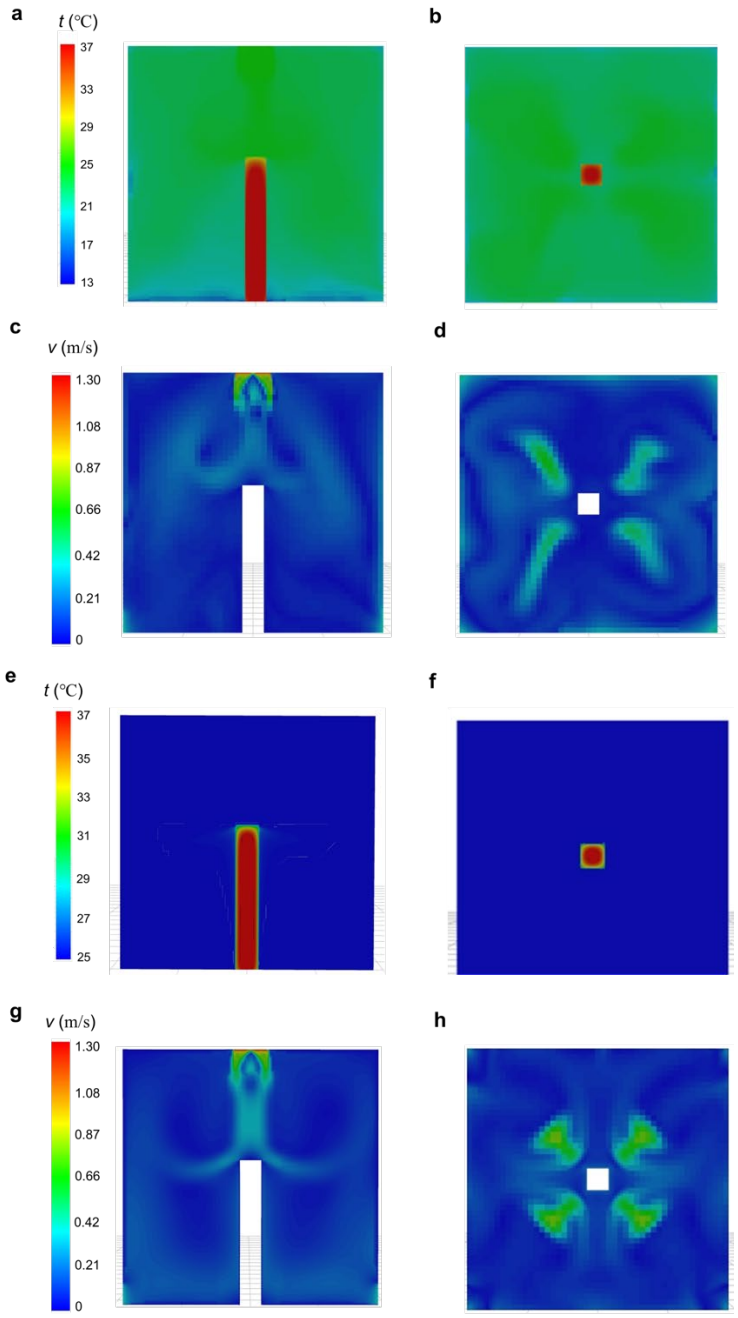

Figure 4.7. Temperature and velocity distribution in single occupant scenario (a) and (e) Temperature distribution on central x-z plane in winter (t_{wall}=13°C, ε=0.9) and summer (t_{wall}=25°C, ε=0.9), (b) and (f) Temperature distribution on central x-y plane in winter (t_{wall}=13°C, ε=0.9) and summer (t_{wall}=25°C, ε=0.9), (c) and (g) velocity distribution on central x-z plane in winter

(t_{wall}=13°C, ε=0.9) and summer (t_{wall}=25°C, ε=0.9), (d) and (h) velocity distribution on central x-y plane in winter (t_{wall}=13°C, ε=0.9) and summer (t_{wall}=25°C, ε=0.9)

Figure 4.8 shows both radiative loss and the convective loss, we can see by decreasing the emissivity of the walls, the increase of the mean radiant temperature and decrease of radiative heat loss compensates the increase in the convective heat loss.

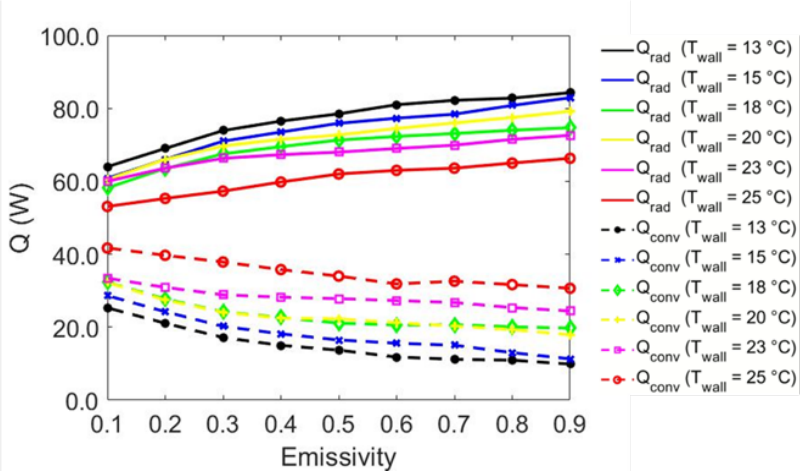

Figure 4.8 Radiative and convective heat loss in six different wall temperature scenarios

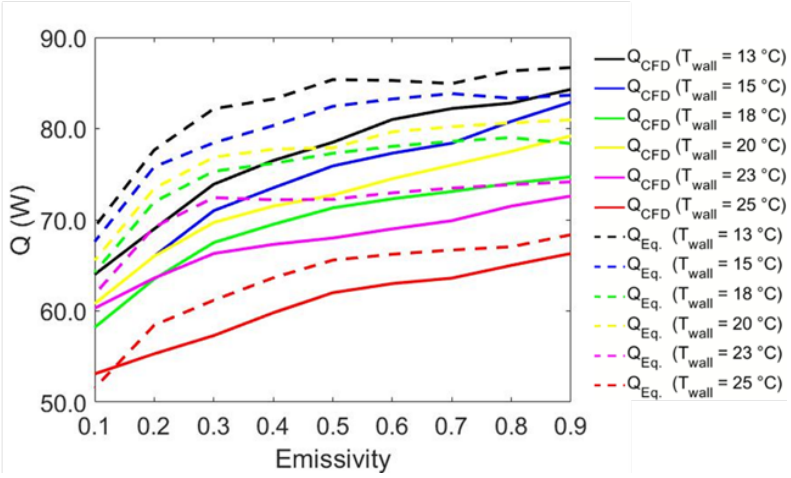

Figure 4.9 Radiative heat loss calculated both from CFD model and Equation 4.2 in six different wall temperature scenarios

The above simulations where the wall temperature is set to be constant (which can be reasonable when the wall is thin) are meant to simplify the model and emphasize the correlation between the variation of the emissivity of the walls and the average air temperature change in the room.

In the following simulations, we assume an outside air temperature of 5℃ in winter and 27℃ in summer, with the wall temperatures determined by both the external and internal environment (walls have the thickness of 0.37m and the conductivity of 0.77W/(m·K)[S1] and the external surfaces have a mixed boundary taking both convection (heat transfer coefficient of 21.6W/(m^2·K)[S2] and free stream temperature of 5℃ and 27℃ respectively) and radiation (radiation temperature of 5℃ and 27℃ respectively and external emissivity of 0.9) into consideration as schematically shown in Figure 4.10 (a)). We can see in winter as the indoor temperature decreases, the interior wall temperature also decreases (1.9℃ drop in winter as the emissivity varies), the set point change in winter can reach 3.8℃ when the emissivity of the wall changes to 0.1 from 0.9. 3.8℃ is a smaller change compared with our initial calculation which is meant to be a guidance of the highest potential set point change. However, a 3.8℃ set point change is quite impactful in terms of energy savings. In summer, the temperature change is smaller due to the smaller difference between indoor and outdoor temperature, but still shows the same trend as before: a higher emissivity is preferred in the summer to reduce cooling energy needs.

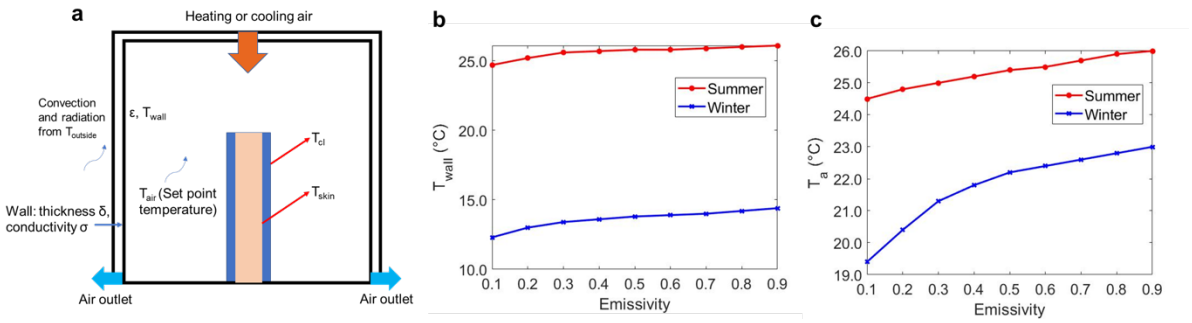

Figure 4.10. Coupling internal and external environment. (a) Schematic description of the settings in the model, (b) Wall temperature varies with emissivity for both summer and winter conditions, and (c) average air temperature (set point) varies with the emissivity of the walls as well

We conducted an additional CFD calculation for the person standing at a different location in the room. The results are shown in the supplementary information Figure 4.11. Because of the uniform air distribution, the location of the occupant does not have a significant effect on the result.

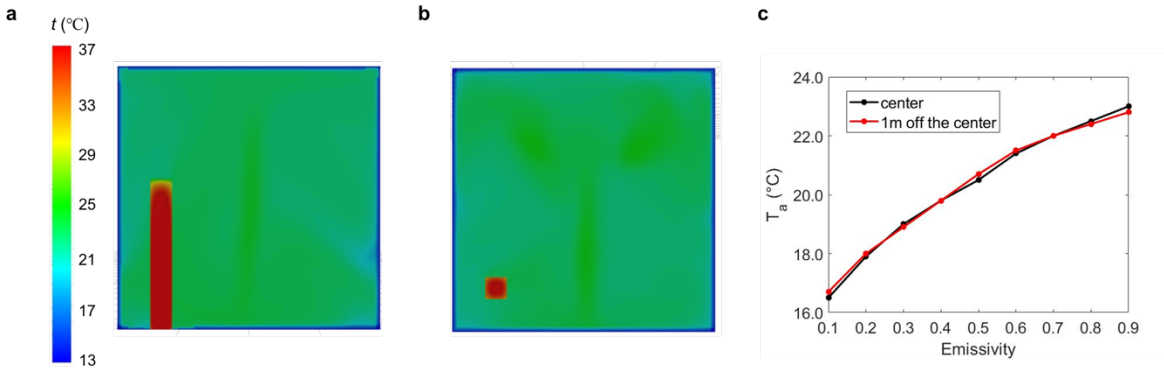

Figure 4.11. Effect of occupant location on CFD results. (a) Temperature distribution in the x = 0.5m plane when the wall temperature is 13°C and the occupant located 1 m off the center, (b) Temperature distribution in the z = 1.5m plane when the wall temperature is 13°C and the occupant

located at 1m off the center, (c) Average air temperature in the room varies with the emissivity of the walls in the center located and off center located case respectively when the wall temperature is 13°C

4.3.3 Set-point change for multiple occupant scenario

Next, we investigated a common scenario in most buildings: the presence of more than one occupant in an interior space (Figure 4.12 (a)), or more generically multiple heat sources. The pathlines in Figure 4.12 (a) indicate the heating/cooling air enters from the inlet and shows a mean air velocity in the room is 0.1 m/s (see Figure 4.13 for temperature and velocity distribution at different planes). We implemented this scenario numerically in both cold weather (wall temperature 13°C) and warm weather (wall temperature 25°C) scenarios. When there is more than one occupant in the same room, the heat source is effectively multiplied and there is not only heat transfer between occupant and surroundings, but also between occupants. In typical cases, such as a classroom or movie theater, the space between different occupants is quite narrow. If we treat the multiple occupants a single, larger heat source, the emissivity effect will be enhanced according to Eq. (4.2) because the area of the hot object increases. Extending this analysis when multiple occupants are in the same room, the low emissivity walls will not only reflect their own heat back but also others' heat to them, which makes them feel warmer than the single occupant case. On the other hand, in summer, if the walls reflect part of the radiative heat back, the multiple occupants will result in a significant cooling load for the air conditioner. However, if the walls can absorb most of the heat, the energy used in cooling will be substantially decreased.

The radiative heat flux and set point change resulting from varying emissivity in both winter and summer are shown in Figure 4.12. In the cold weather case, Figure 4.12 (b) shows the average radiative heat loss of each occupant decreases from 81.1W to 48.9W when the emissivity decreases from 0.9 to 0.1. There is also an acceleration of change after emissivity goes below than 0.3. This leads to a sharp set point temperature decrease of 8.2°C when the emissivity is 0.1 (shown in Figure 4.12 (c)). Similarly, in the warm weather case, the radiative heat loss of each occupant is increased from 38.4 W to 60.5 W when the emissivity increases from 0.1 to 0.9 (Figure 4.12 (b)). There is also an acceleration in the heat transfer reduction as emissivity goes below than 0.3. This leads to a sharp set point temperature decrease of up to 3.2°C when the emissivity is 0.1 (Figure 4.12 (c)), necessitating substantially more cooling. These results highlight that in dense spaces like classrooms, theaters and indoor stadiums, a significant amount of energy can be saved by implementing a tunable emissivity surface on the walls, ceilings, and floors.

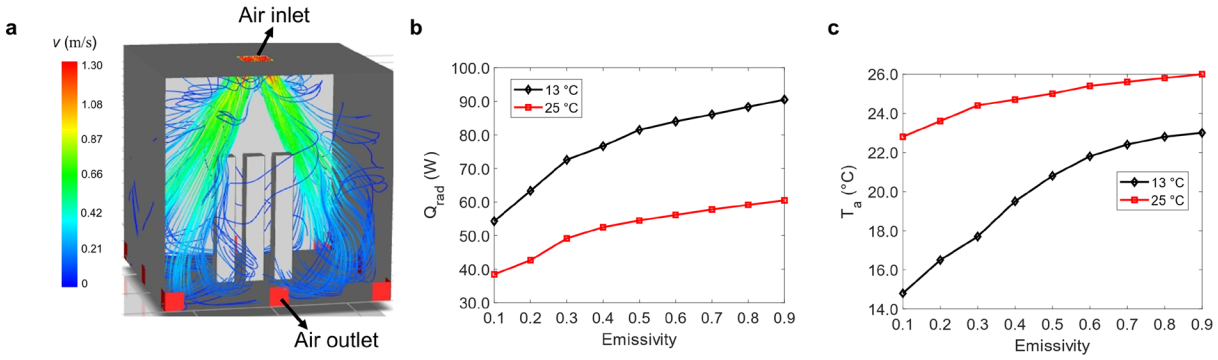

Figure 4.12: Multiple occupant scenario: (a) Computational model for multiple occupants in a conditioned space. (b) Radiative heat loss as a function of emissivity in both cold weather (black line) and warm weather (red line) conditions (c) The heating set point decreases from 23° to 14.8°C when the emissivity varying from 0.9 to 0.1 (black line), while the cooling set point increases from 22.8°C to 26°C as the emissivity increases from 0.1 to 0.9

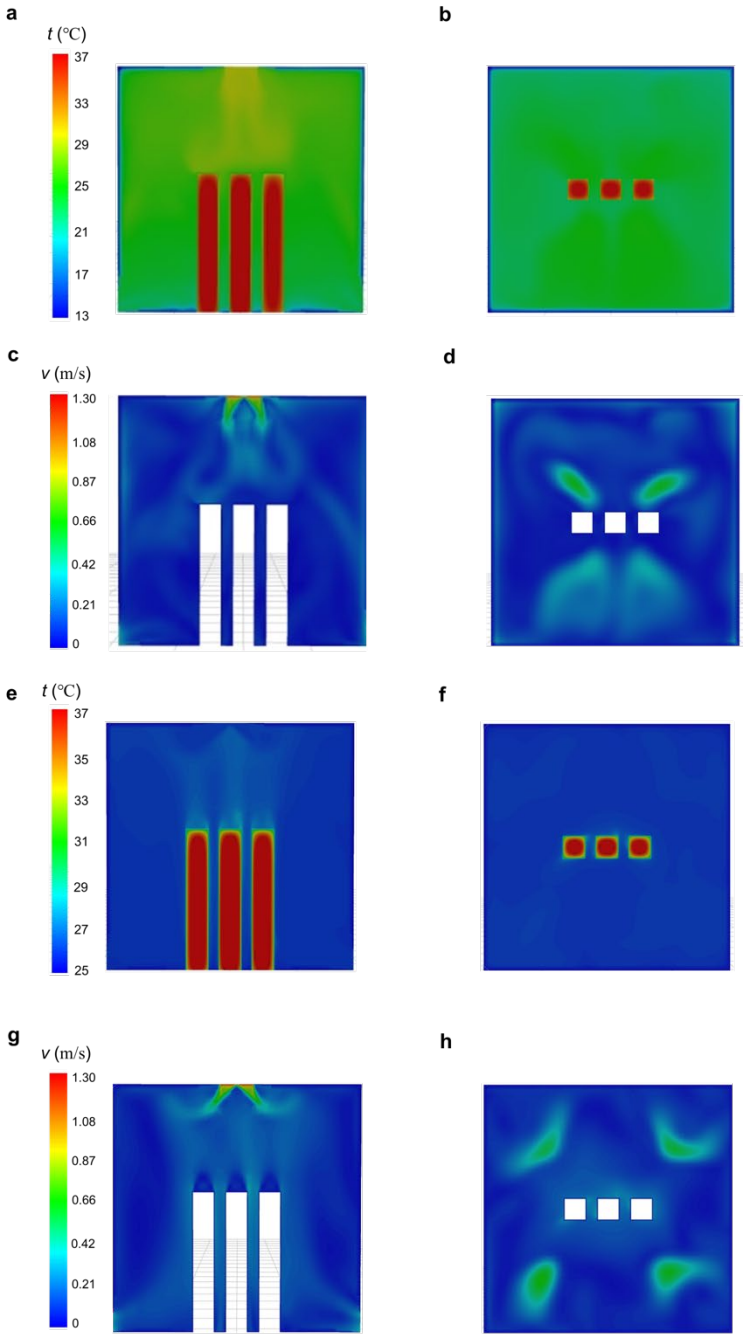

Figure 4.13. Temperature and velocity distribution in multiple occupants scenario. (a) and (e) Temperature distribution on central x-z plane in winter (t_{wall}=13°C, ε=0.9) and summer (t_{wall}=25°C, ε=0.9), (b) and (f) Temperature distribution on central x-y plane in winter (t_{wall}=13°C, ε=0.9) and

summer (t_{wall}=25°C, ε=0.9), (c) and (g) velocity distribution on central x-z plane in winter (t_{wall}=13°C, ε=0.9) and summer (t_{wall}=25°C, ε=0.9), (d) and (h) velocity distribution on central x-y plane in winter (t_{wall}=13°C, ε=0.9) and summer (t_{wall}=25°C, ε=0.9)

After obtaining the potential set point change as we vary the emissivity of the interiors at different wall temperatures, we next evaluated how this change could affect the thermal comfort level of the occupants.

4.4 Thermal comfort analysis

Thermal comfort is essential for human health, well-being as well as productivity. A lack of thermal comfort can cause stress among occupants in a building [161]. Although thermal sensitivity varies from one person to another, six variables can be used to model a person's thermal comfort level: air temperature, mean radiant temperature, air velocity, air humidity, clothing resistance, and activity level [129,161]. To qualitatively assess the thermal comfort level, the predicted mean vote (PMV) model is the most widely used method in thermal comfort standards today [119,162,163]. PMV is an index that aims to predict the mean value of votes of a group of occupants on a seven-point thermal sensation scale. Within the PMV index, +3, +2, +1 represent hot, warm, slightly warm respectively while -3, -2, -1 represents cold, cool, slightly cool respectively. A PMV that falls between -0.5~+0.5 is considered to represent the ideal thermal comfort status for a human being [163].

We adapt a thermal equilibrium approach to infer human thermal comfort [162,163] for a range of emissivity conditions by computing the PMV:

$$PMV = (0.028 + 0.3033e^{-0.036M}) \times L \quad (4.3)$$

$$L = (M - W) - 3.05 \times 10^{-3}(5733 - 6.99(M - W) - P_a) - 0.42(M - W - 58.15) - 1.7 \times 10^{-5}(5867 - P_a) - 0.0014M(34 - t_a) - f_{cl}h_c(t_{cl} - t_a) - 3.96 \times 10^{-8}f_{cl}[(t_{cl} + 273)^4 - (t_r + 273)^4] \quad (4.4)$$

Here L defines the overall heat transfer around an occupant in W/m^2, M is the metabolic rate in W/m^2, W is the work done by the occupant in W/m^2, P_a is the water vapor pressure in the air in Pa, t_r is the mean radiant temperature in °C, t_a is the air temperature in °C, f_{cl} is the clothing correction factor accounts for the actual surface area of the clothed body compared with the body surface area, I_{cl} is the clothing insulation in clo and h_c is the convective heat transfer coefficient in W/m^2.

Eq. (4.4) is obtained by balancing the total heat transfer components for the human occupant of the conditioned space: (1) heat generation due to metabolism and the work done to the environment $(M - W)$, (2) convective heat transfer by $f_{cl}h_c(t_{cl} - t_a)$, (3) heat transfer through the skin $3.05 \times 10^{-3}(5733 - 6.99(M - W) - P_a)$, (4) heat transfer through latent respiration $1.7 \times 10^{-5}(5867 - P_a)$, (5) heat transfer by dry respiration $0.0014M(34 - t_a)$, and (6) heat transfer by radiation $3.96 \times 10^{-8}f_{cl}[(t_{cl} + 273)^4 - (t_r + 273)^4]$. In our evaluation, the relative humidity is set to 50% for all scenarios [164] (for different relative humidity PMV results, see Figure 4.15). The temperature t_{cl} and t_a are obtained from our CFD calculation.

As shown in eq. (4.4), mean radiant temperature t_r is a key variable in thermal comfort for the human body. In prior work [120,128,129,162,163] and even in the ASHRAE standard 55 [161], the mean radiant temperature is calculated based on an assumption that all the building materials have high emissivity (assumed to be ~1). Since in our analysis the emissivity of the building materials is changing dramatically, we must calculate the mean radiant temperature from its initial definitions:

$$Q_{rad} = \sigma(T_{cl}^4 - T_r^4) \tag{4.5}$$

$$T_r = \sqrt[4]{T_{cl}^4 - \frac{Q_{rad}}{\sigma}} \tag{4.6}$$

Here Q_{rad} is the radiative heat transferred between the occupant and the interior walls which is obtained from the CFD calculation, T_r is the mean radiant temperature t_r in degrees Kelvin, T_{cl} is the temperature of the surface of clothing in degrees Kelvin. Figure 4.14 (a) shows how the calculated mean radiant temperature t_r changes as the emissivity of the wall varies for different wall temperatures. We can see that t_r is increased as we decrease the emissivity of the wall. Since the surface temperature of the clothing is always higher than the wall temperature, t_r in all six different wall temperature scenarios is increased as the occupant loses less radiative heat to the surroundings (meaning that the occupant sees a warmer "object"). When the temperature difference between the surrounding walls and the surface of the clothing is larger in colder weather, the mean radiant temperature t_r increase is more significant (2.3°C when wall temperature is 13 °C and 2.2°C when it is 15°C). However, when the wall temperature is closer to the clothing surface temperature the mean radiant temperature change t_r is less than 1°C.

From the above analysis, we obtained the thermal comfort index (PMV) for different wall temperatures with the emissivity of the building interior surfaces varying from 0.9 to 0.1. As shown in Figure 4.14 (b), the PMV remains in the -0.5 to +0.5 comfort zone. This result highlights that decreasing set point temperature in colder weather or increasing the set point in warm weather by changing the emissivity of the walls, will not compromise the thermal comfort of the human occupants.

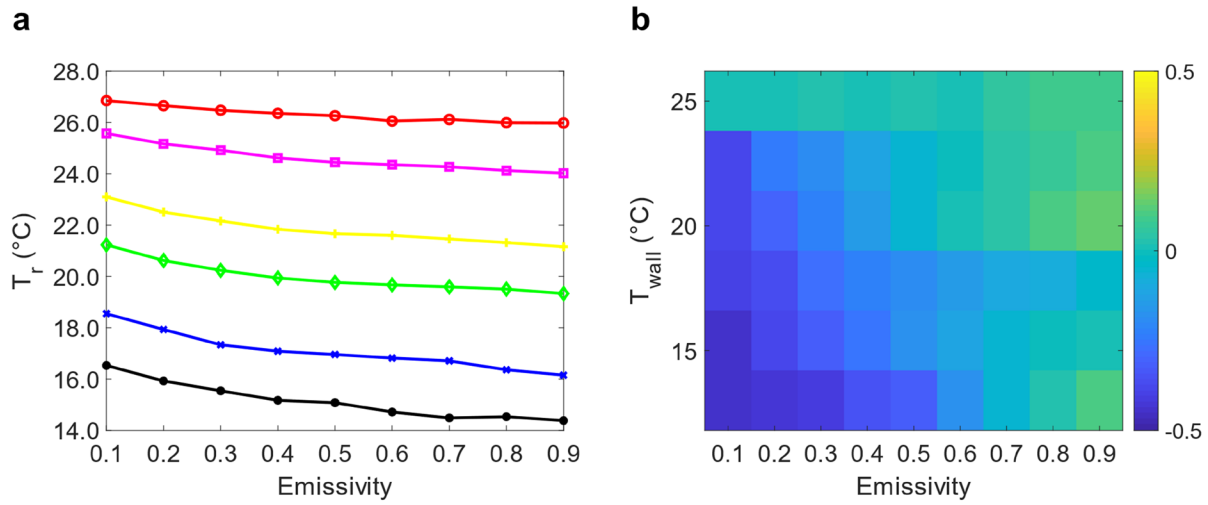

Figure 4.14: Thermal comfort evaluation (a) Mean radiant temperature t_r changes as the emissivity of the wall varies at different wall temperatures, (b) PMV for different wall temperatures with the emissivity of the building interiors varies from 0.9 to 0.1

We calculated two more PMV evaluations where the humidity is set to 30% and 60% respectively. As shown below in Figure 4.15, the PMV range changes from "-0.4-0.4" at 50% humidity to "-0.6-0.3" at 30% humidity and "-0.5-0.5" at 60% humidity range.

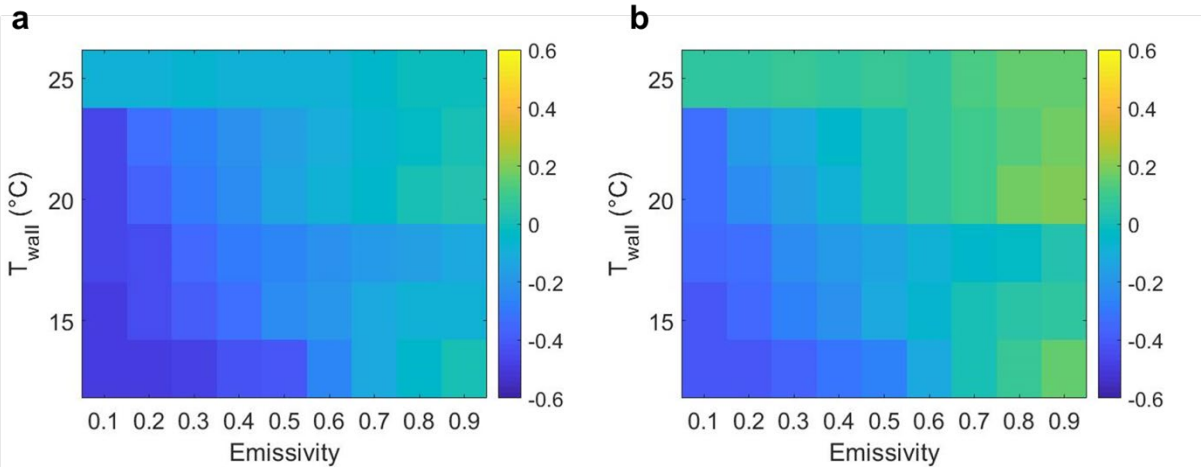

Figure 4.15. PMV values at different relative humidity levels. (a) PMV values as a function of wall temperature and emissivity when the relative humidity is 30%, (b) PMV values as a function of wall temperature and emissivity when the relative humidity is 60%

4.5 Energy savings analysis

To assess the building-level energy savings possible from our proposed approach, we use EnergyPlus, a widely used building energy analysis tool [165]. We use the changes in setpoint predicted by our CFD simulation results and apply them in EnergyPlus to estimate the energy savings for heating and cooling in a commercial building. For this preliminary analysis, we chose a small hotel reference building [166] as our model building. The building has a low window/ wall ratio (184.2 m^2/ 1,695 m^2) making it similar overall to the structure simulated in our CFD analysis [166]. We chose two locations, Ancona, Italy [167] and Minneapolis, USA, to represent two types of climates with strong seasonal temperature variations: humid subtropical (also known as warm temperature) and continental climate respectively. We first used the baseline setpoint previously mentioned (26°C in summer and 23°C in winter) to calculate the average internal surface wall temperature of all the guest rooms in this building. We then used the average internal surface temperature obtained from EnergyPlus and found the corresponding predicted set point change from our CFD calculations for that wall temperature. For example, if the average internal surface temperature is 18°C, we will use a 3.7°C set point decrease for heating, which is the value obtained according to the CFD calculation when the emissivity of interior surfaces is changed from 0.9 to 0.1.

Table 4.2 and Table 4.3 show the average internal surface wall temperature of all the guest rooms in the small hotel throughout the year in Minneapolis and Ancona, respectively. We then adjusted the set point used for each month according to the average wall temperature for that month and the corresponding CFD-based prediction for setpoint change. This then allows us to obtain a preliminary estimate of the whole year heating energy saving and cooling energy penalty for low emissivity (0.1) surfaces in the two chosen locations.

Table 4.2: Average room internal surface temperature (°C), Minneapolis, USA

Jan	Feb	Mar	Apr	May	Jun	Jul	Aug	Sep	Oct	Nov	Dec
12.7	15.3	16.1	20.6	22.9	23.1	24.8	23.1	22.9	20.2	18.4	15.5

Table 4.3: Average room internal surface temperature (°C), Ancona, Italy

Jan	Feb	Mar	Apr	May	Jun	Jul	Aug	Sep	Oct	Nov	Dec
18.2	18.7	19.6	21.2	22.0	23.2	24.1	24.3	23.7	22.1	20.4	19.2

Figure 4.16 shows the potential energy savings at the two locations throughout the year due to modified setpoints made possible by tuning the interior surface emissivity values to 0.1 during the heating season, and 0.9 during the cooling season. We find that in Figure 5, the energy used for heating in Minneapolis decreases from 379,930 kWh to 242,539 kWh when we switch from a high emissivity interior ($\varepsilon = 0.9$) to a low emissivity interior ($\varepsilon = 0.1$), corresponding to a 36.8% savings in heating energy throughout a year. The heating energy consumption in Ancona

decreases from 88,020 kWh to 58,183 kWh when we use a low emissivity interior (ε = 0.1), corresponding to a 34.1%. Conversely, for cooling, the energy use in this hotel increases from 72,470 kWh to 97,367 kWh when the emissivity changes from 0.9 to 0.1, which leads to a 34.7% energy penalty if the low emissivity interior surfaces are not tuned back to high emissivity in Minneapolis during the cooling season. In Ancona, because of a longer cooling season, the cooling penalty due to low emissivity surfaces is even larger with cooling energy consumption increasing from 104,845 kWh to 139,996 kWh (a 33.5% energy penalty). While this is a preliminary, first-order analysis of energy savings, we observe that the tunable emissivity of the internal surface in a building holds the potential to deliver significant energy savings. For more detailed modeling, EnergyPlus will need to be modified to accurately account for the effect of changing the long-wave infrared emissivity of interior surfaces on occupant thermal comfort, and thus the set-point.

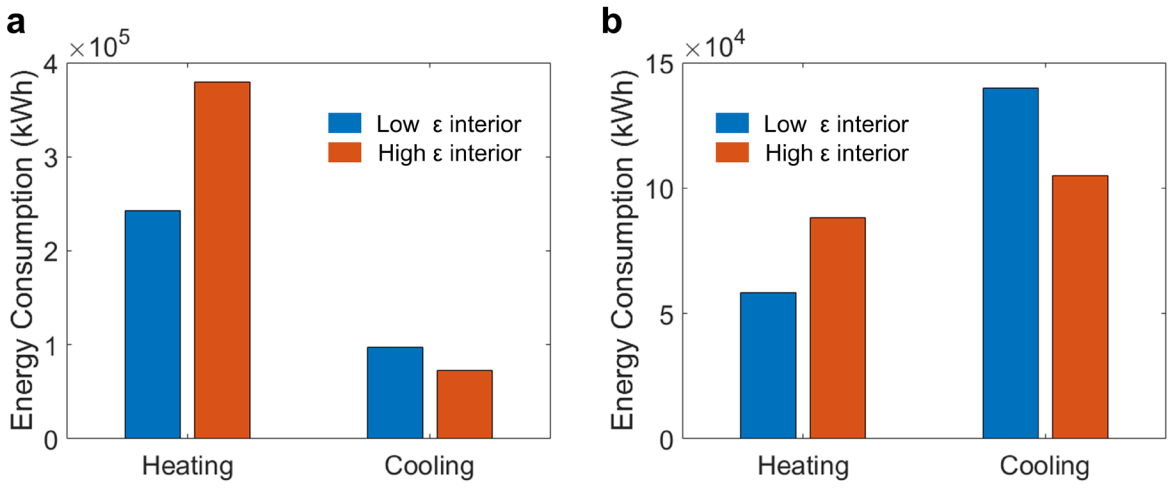

Figure 4.16: Potential energy savings throughout the year due to modified setpoints made possible by specific interior surface emissivity values: Annual energy use from a preliminary analysis for (a) heating and cooling by using high emissivity (ε = 0.9) and low emissivity (ε = 0.1)

interior in a small hotel reference building located in Minneapolis, USA (continental climate) and (b) in a small hotel reference building located in Ancona, Italy (humid subtropical climate).

4.6 Summary

Our results indicate that tuning the emissivity of interior surfaces holds to the potential to deliver meaningful remarkable energy savings, particularly for heating. In recent years, a range of materials have shown the ability to tune their thermal emissivity [147,148]. While these preliminary works indicate that tunable emissivity in the long-wave infrared part of the spectrum is in fact possible, our results highlight the need for further investigation of tunable emissivity materials that can meet the cost and performance targets suitable for large-area application in interior spaces. In the broader context of decarbonizing our built environment, the approach proposed and evaluated here represents a distinctive strategy that can complement a range of existing strategies, including radiant heating, and cooling, electrochromic windows and building integrated photovoltaics. Intriguing opportunities exist to combine the capabilities highlighted here with advances in smart building systems to develop interior spaces that dynamically respond to changing heat loads and occupants, to maximize both comfort and efficiency. More broadly, our results highlight an untapped degree of freedom for energy efficiency that lies in controlling the ubiquitous flows of heat that surround us every day.

This study presents and analyzes a mechanism for energy savings enabled by controlling the emissivity of the interior surfaces in a building. The analysis undertaken here is analytical and simulation-based and is thus a model of representative scenarios in the built environment. The actual impact on real-world building energy use will depend on the building's location, the climate, and the number of human occupants inside, necessitating experimental testing and validation.

Chapter 5 Conclusion and Outlook

In this dissertation, four different fields related to lossy photonic materials were explored. In Chapter 1, we experimentally demonstrated a broadband directional thermal emitter using gradient ENZ films. This approach uses conventional oxides to realize the emitter which makes it immediately useful for large-area heat transfer applications for near-room temperature applications. More broadly, these results highlight that by decoupling angular and spectral response in photonic nanostructures, and different capabilities can emerge for how materials emit and absorb light.

For future work, higher radiance in the s-polarization can be achieved through broadband angular selectivity using effective mu-near-zero (MNZ) materials which could be developed using a metamaterial approach.

In Chapter 2, we use the Si doped InAs realized a broadband directional thermal emitter in the infrared wavelength range using the gradient ENZ thin film framework we put forward in Chapter 1. The emissivity spectrum we obtained is more continuous than using different polariton materials and it is easier to shift to another functional wavelength range by simply changing the doping level in the semiconductor.

Future work may investigate dynamic tunability of the emissivity of doped semiconductors using electrical bias. Specifically, by leveraging the rectification property of a Schottky contact between the metal and the semiconductor, carrier accumulation and depletion can happen which will lead to a plasma frequency change and eventually a permittivity variation.

In Chapter 3, we investigated a type of non-Hermitian photonic system where only contains loss and the lossy material has the same real part of permittivity as the lossless material. We discovered a quasi-bandgap purely induce by introducing a small amount of loss in a lossless

photonic crystal in both 1D and 2D systems. Leveraging this quasi-bandgap phenomenon, we designed a selective reflector which not only can reflect light of certain wavelength but also can absorb the rest. Ultimately, our analysis opens a distinctive area of non-Hermitian photonic crystal system.

In Chapter 4, we show that meaningful building energy savings, particularly for heating can be potentially achieved by tuning the emissivity of interior surfaces. Since analysis undertaken in this thesis is analytical and simulation-based and is thus a model of representative scenarios in the built environment. The actual impact on real-world building energy use will depend on the building's location, the climate, and the number of human occupants inside, necessitating experimental testing and validation as future work.

Appendix A Emissivity results in s polarization of the doped InAs film

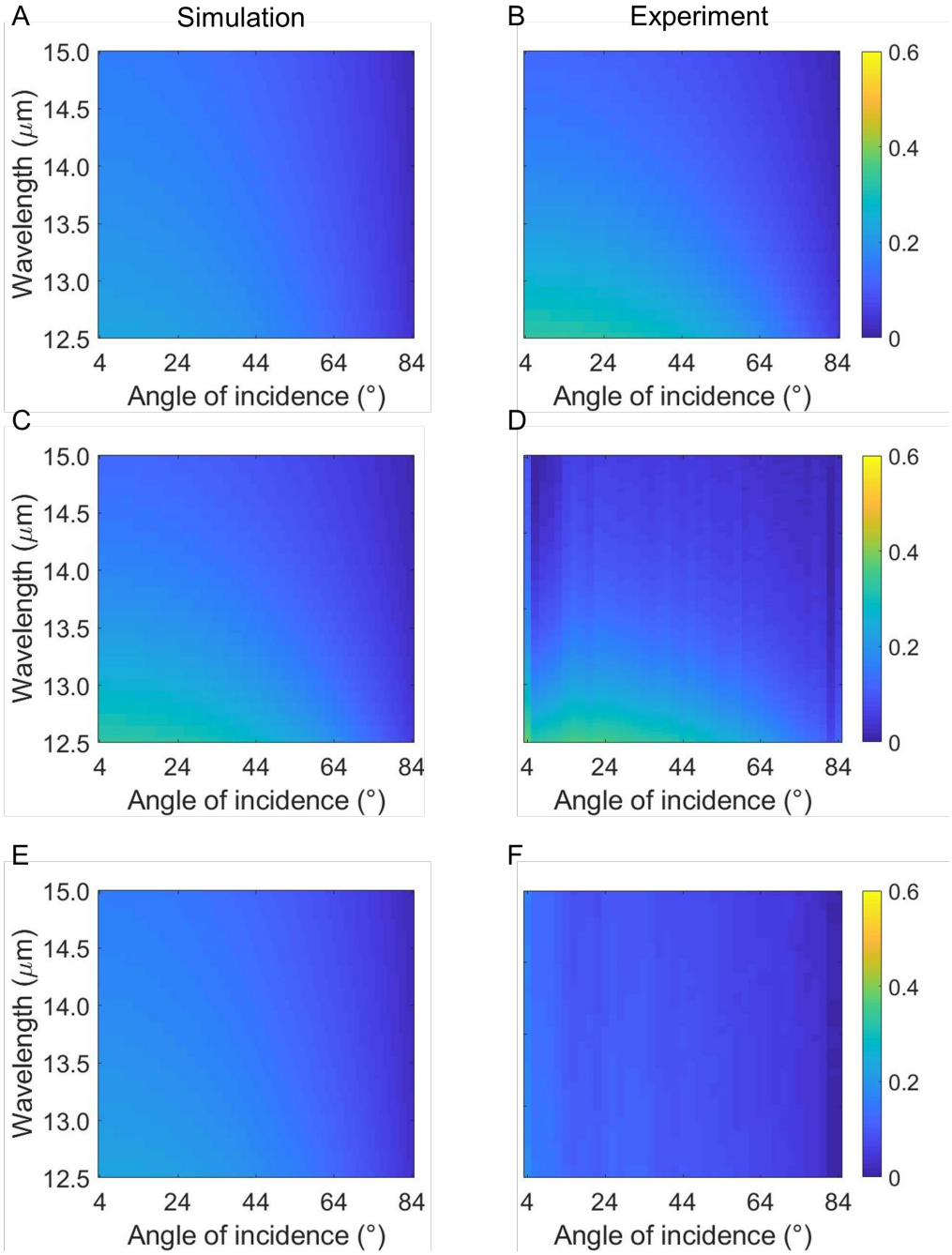

Figure A.2. Emissivity spectra varying with angle and wavelength of the three fabricated gradient doped InAs films for the s polarization. (A), (C) and (E) simulation results of

emissivity in s-polarization using transfer matrix method. (B), (D) and (F) Measured emissivity spectra for s-polarization. The results show that in the s polarization, low emissivity is exhibited by all films regardless of angle of incidence, and that experimental results match well with simulations.

Appendix B 1st and 2nd order perturbation theory for a generalized eigenvalue problem

B.1 Generalized eigen value problem and perturbation

Electric field in a medium follows the equation,

$$\nabla \times \nabla \times \mathbf{E}(r) = \left(\frac{\omega}{c}\right)^2 \epsilon(r)\mathbf{E}(r) \tag{1}$$

Above equation can be treated as a generalized eigen value problem: $\hat{A}\phi = \lambda\hat{B}\phi$, where operators, $\hat{A} = (\nabla \times \nabla \times)$, $\hat{B} = \epsilon(r)$, eigen value $\lambda = \left(\frac{\omega}{c}\right)^2$, and eigen states $\phi = \mathbf{E}(r)$.

Perturbation in permitivity can be applied as, $\epsilon = \epsilon_0 + \gamma\epsilon'$. This will perturb the eigen values and eigen states as,

$$\begin{aligned} \lambda &= \lambda^{(0)} + \gamma\lambda^{(1)} + \gamma^2\lambda^{(2)} + \dots \\ \mathbf{E} &= \mathbf{E}^{(0)} + \gamma\mathbf{E}^{(1)} + \gamma^2\mathbf{E}^{(2)} + \dots \end{aligned} \tag{2}$$

such that $(\nabla \times \nabla \times)\mathbf{E} = \lambda(\epsilon_0 + \gamma\epsilon')\mathbf{E}$. Applying this perturbation in the governing equation,

$$\begin{aligned} \hat{A}(\mathbf{E}^{(0)} + \gamma\mathbf{E}^{(1)} + \gamma^2\mathbf{E}^{(2)} + \dots) = \quad & (\lambda^{(0)} + \gamma\lambda^{(1)} + \gamma^2\lambda^{(2)} + \dots) \\ & (\epsilon_0 + \gamma\epsilon')(\mathbf{E}^{(0)} + \gamma\mathbf{E}^{(1)} + \gamma^2\mathbf{E}^{(2)} + \dots) \end{aligned} \tag{3}$$

Multiplying all the terms and ignoring terms higher than γ^2,

$$\begin{aligned}\hat{A}+\mathbf{E}^{(0)}+\gamma\hat{A}\mathbf{E}^{(1)}+\gamma^2\hat{A}\mathbf{E}^{(2)} \quad &= \lambda^{(0)}\epsilon_0\mathbf{E}^{(0)} \\ &+\gamma\left(\lambda^{(0)}\epsilon_0\mathbf{E}^{(1)}+\lambda^{(0)}\epsilon'\mathbf{E}^{(0)}+\lambda^{(1)}\epsilon_0\mathbf{E}^{(0)}\right) \\ &+\gamma^2\left(\lambda^{(0)}\epsilon_0\mathbf{E}^{(2)}+\lambda^{(0)}\epsilon'\mathbf{E}^{(1)}+\lambda^{(1)}\epsilon_0\mathbf{E}^{(1)}\right. \\ &\left.+\lambda^{(1)}\epsilon'\mathbf{E}^{(0)}+\lambda^{(2)}\epsilon_0\mathbf{E}^{(0)}\right)\end{aligned} \tag{4}$$

Since γ is arbitrary, the coefficients of γ must sum up to 0. Using the *braket* notation for the nth eigen state, the coefficients of γ^0, γ^1, and γ^2 are shown below,

$$\hat{A}\mathbf{E}_n^{(0)} = \lambda^{(0)}\epsilon_0\mathbf{E}_n^{(0)} \quad \text{(unperturbedstate)} \tag{5}$$

$$\hat{A}\mathbf{E}_n^{(1)} = \left(\lambda^{(1)}\epsilon_0+\lambda^{(0)}\epsilon'\right)\mathbf{E}_n^{(0)}+\lambda^{(0)}\epsilon_0\mathbf{E}_n^{(1)} \tag{6}$$

$$\begin{aligned}\hat{A}\mathbf{E}_n^{(2)} \quad &= \left(\lambda^{(1)}\epsilon'+\lambda^{(2)}\epsilon_0\right)\mathbf{E}_n^{(0)} \\ &+\left(\lambda^{(0)}\epsilon'+\lambda^{(1)}\epsilon_0\right)\mathbf{E}_n^{(1)} \\ &+\left(\lambda^{(0)}\epsilon_0\right)\mathbf{E}_n^{(2)}\end{aligned} \tag{7}$$

B.2 1st order perturbation

Multiplying equation (6) by $\mathbf{E}_n^{(0)}$,

$$\begin{aligned}\mathbf{E}_n^{(0)}|\hat{A}|\mathbf{E}_n^{(1)} \quad &= \lambda^{(1)}\mathbf{E}_n^{(0)}|\epsilon_0|\mathbf{E}_n^{(0)}+\lambda^{(0)}\mathbf{E}_n^{(0)}|\epsilon'|\mathbf{E}_n^{(0)}+\lambda^{(0)}\mathbf{E}_n^{(0)}|\epsilon_0|\mathbf{E}_n^{(1)} \\ \lambda^{(0)}\mathbf{E}_n^{(0)}|\epsilon_0|\mathbf{E}_n^{(1)} \quad &= \lambda^{(1)}\mathbf{E}_n^{(0)}|\epsilon_0|\mathbf{E}_n^{(0)}+\lambda^{(0)}\mathbf{E}_n^{(0)}|\epsilon'|\mathbf{E}_n^{(0)}+\lambda^{(0)}\mathbf{E}_n^{(0)}|\epsilon_0|\mathbf{E}_n^{(1)} \\ &\lambda^{(1)} = -\lambda^{(0)}\frac{\mathbf{E}_n^{(0)}|\epsilon'|\mathbf{E}_n^{(0)}}{\mathbf{E}_n^{(0)}|\epsilon_0|\mathbf{E}_n^{(0)}}\end{aligned} \tag{8}$$

Furthermore, $\epsilon = \epsilon_0+\gamma\epsilon'\Delta\epsilon = \epsilon-\epsilon_0 = \gamma\epsilon'$. Similarly, $\Delta\lambda = \lambda-\lambda^{(0)} = \gamma\lambda^{(1)}$ (ignoring γ^2 and higher terms). Using error analysis for the eigen value,

$$\begin{aligned} \lambda^{(0)} &= \left(\frac{\omega^{(0)}}{c}\right)^2 \frac{\Delta\lambda}{\lambda^{(0)}} = 2\frac{\Delta\omega}{\omega^{(0)}} \\ \Delta\omega &= \left(\frac{1}{2}\frac{\omega^{(0)}}{\lambda^{(0)}}\right)\Delta\lambda \end{aligned} \tag{9}$$

Using equations (8) and (9),

$$\Delta\omega = -\frac{\omega^{(0)}}{2}\frac{\mathbf{E}_n^{(0)}|\Delta\epsilon|\mathbf{E}_n^{(0)}}{\mathbf{E}_n^{(0)}|\epsilon_0|\mathbf{E}_n^{(0)}} + O(\gamma^2) \tag{10}$$

Since the unperturbed states are orthogonal, we use them as basis,

$$\mathbf{E}_n^{(1)} = \sum_{j=1}^{N} c_{nj}\mathbf{E}_j^{(0)} \tag{11}$$

plug (11) into (6),

$$\hat{A}\sum_{j=1}^{N} c_{nj}\mathbf{E}_j^{(0)} = \lambda_n^{(0)}\epsilon^{(0)}\sum_{j=1}^{N} c_{nj}\mathbf{E}_j^{(0)} + \lambda_n^{(1)}\epsilon^{(0)}\mathbf{E}_n^{(0)} + \lambda_n^{(0)}\epsilon'\mathbf{E}_n^{(0)} \tag{12}$$

we multiply by $\mathbf{E}_k^{(0)}$ and get

$$\sum_{j=1}^{N} c_{nj}\lambda_j^{(0)}\mathbf{E}_k^{(0)}|\epsilon^{(0)}|\mathbf{E}_j^{(0)} = \lambda_n^{(0)}\sum_{j=1}^{N} c_{nj}\mathbf{E}_k^{(0)}|\epsilon^{(0)}|\mathbf{E}_j^{(0)} + \lambda_n^{(1)}\mathbf{E}_k^{(0)}|\epsilon^{(0)}|\mathbf{E}_n^{(0)} + \lambda_n^{(0)}\mathbf{E}_k^{(0)}|\epsilon'|\mathbf{E}_n^{(0)} \tag{13}$$

then we get

$$c_{nk} = \left(\frac{\lambda_n^{(0)}}{\lambda_k^{(0)} - \lambda_n^{(0)}}\right)\frac{\mathbf{E}_k^{(0)}|\epsilon'|\mathbf{E}_n^{(0)}}{\mathbf{E}_k^{(0)}|\epsilon_0|\mathbf{E}_k^{(0)}} \qquad (k \neq n) \tag{14}$$

Since, perturbed state is orthogonal to the original state $\mathbf{E}_n^{(1)}|\mathbf{E}_n^{(0)} = 0$, we get $c_{nn} = 0$, so

$$\mathbf{E}_n^{(1)} = \sum_{\substack{j=1 \\ j\neq n}}^{N}\left(\frac{\lambda_n^{(0)}}{\lambda_j^{(0)} - \lambda_n^{(0)}}\right)\frac{\mathbf{E}_j^{(0)}|\epsilon'|\mathbf{E}_n^{(0)}}{\mathbf{E}_j^{(0)}|\epsilon_0|\mathbf{E}_j^{(0)}}\mathbf{E}_j^{(0)} \tag{15}$$

B.3 2nd order perturbation

Now we already see in the 1st order Perturbation theory that the imaginary part of the eigen frequency will have an imaginary part change when the permitivity is imaginary, we will continue to see what the 2nd order perturbation can tell us: multiply eq.(7) by $\mathbf{E}^{(0)}$

$$\mathbf{E}^{(0)}|\hat{A}|\mathbf{E}^{(2)} = \mathbf{E}^{(0)}|(\lambda^{(1)}\epsilon' + \lambda^{(2)}\epsilon^{(0)})|\mathbf{E}^{(0)} + \mathbf{E}^{(0)}|(\lambda^{(0)}\epsilon' + \lambda^{(1)}\epsilon^{(0)})|\mathbf{E}^{(1)} + \mathbf{E}^{(0)}|(\lambda^{(0)}\epsilon_0)|\mathbf{E}^{(2)} \quad (16)$$

$$\lambda_n^{(1)}\mathbf{E}_n^{(0)}|\epsilon'|\mathbf{E}_n^{(0)} + \lambda_n^{(2)}\mathbf{E}_n^{(0)}|\epsilon_0|\mathbf{E}_n^{(0)} + \lambda_n^{(0)}\mathbf{E}_n^{(0)}|\epsilon'|\mathbf{E}_n^{(1)} + \lambda_n^{(1)}\mathbf{E}_n^{(0)}|\epsilon_0|\mathbf{E}_n^{(1)} = 0 \quad (17)$$

Using result for $\lambda^{(1)}$ from equation (8), we get

$$\lambda_n^{(2)} = \lambda_n^{(0)}\left(\frac{\mathbf{E}_n^{(0)}|\epsilon'|\mathbf{E}_n^{(0)}}{\mathbf{E}_n^{(0)}|\epsilon_0|\mathbf{E}_n^{(0)}}\right)^2 + \lambda_n^{(0)}\sum_{\substack{j=1 \\ j\neq n}}^{N}\left[\left(\frac{\lambda_n^{(0)}}{\lambda_n^{(0)}-\lambda_j^{(0)}}\right)\frac{\mathbf{E}_j^{(0)}|\epsilon'|\mathbf{E}_n^{(0)}}{\mathbf{E}_j^{(0)}|\epsilon_0|\mathbf{E}_j^{(0)}}\frac{\mathbf{E}_n^{(0)}|\epsilon'|\mathbf{E}_j^{(0)}}{\mathbf{E}_n^{(0)}|\epsilon_0|\mathbf{E}_n^{(0)}}\right] \quad (18)$$

The correction in eigen state can be calculated as,

$$\lambda = \lambda^{(0)} + \gamma\lambda^{(1)} + \gamma^2\lambda^{(2)} \quad (19)$$

$$\Delta\lambda = \gamma\lambda^{(1)} + \gamma^2\lambda^{(2)} \quad (20)$$

Furthermore, using $\gamma = 1$

$$\begin{aligned} \frac{\Delta\lambda}{\lambda^{(0)}} &= 2\frac{\Delta\omega}{\omega^{(0)}} \\ \Delta\omega &= \frac{1}{2}\frac{\omega^{(0)}}{\lambda^{(0)}}\left(\lambda^{(1)} + \lambda^{(2)}\right) \end{aligned} \quad (21)$$

Finally using $\Delta\epsilon = \epsilon'$, we get:

$$\Delta\omega^{(2)} = \frac{\omega^{(0)}}{2}\left[-\frac{\langle \boldsymbol{E_n^{(0)}}|\Delta\epsilon|\boldsymbol{E_n^{(0)}}\rangle}{\langle \boldsymbol{E_n^{(0)}}|\epsilon_0|\boldsymbol{E_n^{(0)}}\rangle} + \left(\frac{\langle \boldsymbol{E_n^{(0)}}|\Delta\epsilon|\boldsymbol{E_n^{(0)}}\rangle}{\langle \boldsymbol{E_n^{(0)}}|\epsilon_0|\boldsymbol{E_n^{(0)}}\rangle}\right)^2 + \sum_{\substack{j=1 \\ j\neq n}}^{N} \frac{\lambda_n^{(0)}}{\lambda_n^{(0)} - \lambda_j^{(0)}} \frac{\langle \boldsymbol{E_j^{(0)}}|\Delta\epsilon|\boldsymbol{E_n^{(0)}}\rangle}{\langle \boldsymbol{E_j^{(0)}}|\epsilon_0|\boldsymbol{E_j^{(0)}}\rangle} \frac{\langle \boldsymbol{E_n^{(0)}}|\Delta\epsilon|\boldsymbol{E_j^{(0)}}\rangle}{\langle \boldsymbol{E_n^{(0)}}|\epsilon_0|\boldsymbol{E_n^{(0)}}\rangle}\right]$$

Then we assume the electric field is $\mathbf{E}^{(0)} = \cos(\pi x/a)$ and $\mathbf{E}^{(0)} = \sin(\pi x/a)$ for any two sequential bands and we plug this expression in to Eq. 3.5 to calculate the eigenfrequency change at the the band edges:

First order perturbation:

When $\mathbf{E}^{(0)} = \cos(\pi x/a)$,

$$\Delta\omega^{(1)} = -\frac{\omega^{(0)}}{2}\frac{\int_0^a \Delta\epsilon\cos^2(\pi x/a)\,dx}{\int_0^a \epsilon_0\cos^2(\pi x/a)\,dx} \tag{22}$$

because

$$\Delta\epsilon(z) = \begin{cases}\epsilon' & 0 \le x \le d \\ 0 & d < x \le a\end{cases}$$

$$\Delta\omega^{(1)} = -\frac{\omega^{(0)}}{2}\frac{\Delta\epsilon}{\epsilon_0}\frac{\int_0^d \Delta\epsilon\cos^2(\pi x/a)\,dx}{\int_0^a \epsilon_0\cos^2(\pi x/a)\,dx} \tag{23}$$

$$\Delta\omega^{(1)} = -\frac{\omega^{(0)}}{2}\frac{\Delta\epsilon}{\epsilon_0}\left[\frac{d}{a} + \frac{1}{2\pi}sin\left(\frac{2\pi d}{a}\right)\right] \tag{24}$$

When $\mathbf{E}^{(0)} = \sin(\pi x/a)$,

$$\Delta\omega^{(1)} = -\frac{\omega^{(0)}}{2}\frac{\int_0^a \Delta\epsilon\sin^2(\pi x/a)\,dx}{\int_0^a \epsilon_0\sin^2(\pi x/a)\,dx} \tag{25}$$

$$\Delta\omega^{(1)} = -\frac{\omega^{(0)}}{2}\frac{\Delta\epsilon}{\epsilon_0}\frac{\int_0^d \Delta\epsilon \sin^2(\pi x/a)\, dx}{\int_0^a \epsilon_0 \sin^2(\pi x/a)\, dx} \tag{26}$$

$$\Delta\omega^{(1)} = -\frac{\omega^{(0)}}{2}\frac{\Delta\epsilon}{\epsilon_0}\left[\frac{d}{a} - \frac{1}{2\pi}\sin\left(\frac{2\pi d}{a}\right)\right] \tag{27}$$

Second order perturbation:

When $\mathbf{E}^{(0)} = \cos(\pi x/a)$,

$$\Delta\omega^{(2)} = \frac{\omega^{(0)}}{2}\left[\frac{\int_0^a \Delta\epsilon \cos^2(\pi x/a)\, dx}{\int_0^a \epsilon_0 \cos^2(\pi x/a)\, dx}\right]^2 \tag{28}$$

$$\Delta\omega^{(2)} = \frac{\omega^{(0)}}{2}\left[\frac{\Delta\epsilon}{\epsilon_0}\frac{\int_0^d \Delta\epsilon \cos^2(\pi x/a)\, dx}{\int_0^a \epsilon_0 \cos^2(\pi x/a)\, dx}\right]^2 \tag{29}$$

$$\Delta\omega^{(2)} = \frac{\omega^{(0)}}{2}\left[\frac{\Delta\epsilon}{\epsilon_0}\left(\frac{d}{a} + \frac{1}{2\pi} sin\left(\frac{2\pi d}{a}\right)\right)\right]^2 \tag{30}$$

When $\mathbf{E}^{(0)} = \sin(\pi x/a)$,

$$\Delta\omega^{(2)} = \frac{\omega^{(0)}}{2}\left[\frac{\int_0^a \Delta\epsilon \sin^2(\pi x/a)\, dx}{\int_0^a \epsilon_0 \sin^2(\pi x/a)\, dx}\right]^2 \tag{31}$$

$$\Delta\omega^{(2)} = \frac{\omega^{(0)}}{2}\left[\frac{\Delta\epsilon}{\epsilon_0}\frac{\int_0^d \Delta\epsilon \sin^2(\pi x/a)\, dx}{\int_0^a \epsilon_0 \sin^2(\pi x/a)\, dx}\right]^2 \tag{32}$$

$$\Delta\omega^{(2)} = \frac{\omega^{(0)}}{2}\left[\frac{\Delta\epsilon}{\epsilon_0}\left(\frac{d}{a} - \frac{1}{2\pi} sin\left(\frac{2\pi d}{a}\right)\right)\right]^2 \tag{33}$$

Appendix C Boundary conditions and variables obtained from the CFD simulation

Tinlet: ℃

$\varepsilon \backslash T_{wall}$	13℃	15℃	18℃	20℃	23℃	25℃
0.9	25.2	24.8	23.8	27.4	26.9	25.8
0.8	24.6	24.0	23.6	26.9	26.7	25.5
0.7	24.1	23.9	23.3	26.4	26.4	25.3
0.6	22.9	23.4	23.1	25.9	26.2	25.1
0.5	22.0	22.7	22.8	25.4	25.9	24.8
0.4	21.1	21.9	22.3	24.9	25.4	24.3
0.3	20.2	20.9	21.8	24.4	24.8	23.8
0.2	18.5	19.5	20.7	23.4	24.4	23.3
0.1	16.8	18.0	19.3	21.9	23.9	22.8

T_{cl}: ℃

T_{wall} \ ε	0.9	0.8	0.7	0.6	0.5	0.4	0.3	0.2	0.1
13℃	24.1	24.1	24.1	24.2	24.1	24.1	24.2	24.1	24.1
15℃	24.6	24.6	24.6	24.6	24.5	24.7	24.6	24.6	24.7
18℃	26.3	26.4	26.4	26.4	26.4	26.4	26.5	26.5	26.6
20℃	28.4	28.4	28.4	28.4	28.3	28.4	28.5	28.5	28.6
23℃	30.5	30.5	30.5	30.5	30.5	30.6	30.8	30.8	30.9
25℃	31.8	31.7	31.7	31.7	31.7	31.6	31.5	31.5	31.5

T_a:

T_{wall} \ ε	0.9	0.8	0.7	0.6	0.5	0.4	0.3	0.2	0.1
13℃	23.0	22.5	22.0	21.4	20.5	19.9	19.0	17.9	16.5
15℃	23.0	22.7	22.3	21.9	21.5	20.7	19.8	18.7	17.3
18℃	23.0	22.8	22.6	22.4	22.1	21.7	21.3	20.3	19.3
20℃	26.0	25.7	25.2	24.9	24.3	23.9	23.4	22.5	21.5
23℃	26.0	25.8	25.3	25.0	24.6	24.3	24.0	23.4	22.4
25℃	26.0	25.7	25.4	25.2	25.0	24.6	24.3	24.0	23.7

Q_{rad}:

T_{wall} \ ε	0.1	0.2	0.3	0.4	0.5	0.6	0.7	0.8	0.9
13°C	46.2	45.4	45.0	44.4	43.0	41.9	40.5	37.8	35.1
15°C	45.4	44.3	43.0	42.4	41.6	40.3	38.9	36.2	33.3
18°C	40.9	40.5	40.1	39.6	39.1	38.1	37.0	34.8	31.9
20°C	43.4	42.5	41.6	40.8	39.8	39.5	38.2	36.2	33.3
23°C	39.8	39.2	38.3	37.8	37.3	36.9	36.3	34.8	33.0
25°C	36.3	35.6	34.8	35.2	34.0	32.8	31.4	30.3	29.1

Pa:

T_{wall} \ ε	0.1	0.2	0.3	0.4	0.5	0.6	0.7	0.8	0.9
13°C	1360	1320	1285	1225	1170	1100	1065	970	910
15°C	1360	1320	1285	1225	1170	1100	1065	970	910
18°C	1405	1370	1335	1225	1170	1150	1100	1070	1010
20°C	1680	1650	1600	1525	1450	1390	1320	1300	1285
23°C	1680	1665	1650	1610	1560	1530	1490	1425	1350
25°C	1680	1650	1600	1595	1585	1545	1500	1490	1475

f_{cl}:

T_{wall} \ ε	0.1	0.2	0.3	0.4	0.5	0.6	0.7	0.8	0.9
13°C	1.45	1.45	1.45	1.45	1.45	1.45	1.45	1.45	1.45
15°C	1.38	1.38	1.38	1.38	1.38	1.38	1.38	1.38	1.38
18°C	1.32	1.32	1.32	1.32	1.32	1.32	1.32	1.32	1.32
20°C	1.24	1.24	1.24	1.24	1.24	1.24	1.24	1.24	1.24
23°C	1.15	1.15	1.15	1.15	1.15	1.15	1.15	1.15	1.15
25°C	1.12	1.12	1.12	1.12	1.12	1.12	1.12	1.12	1.12

References

1. Inoue, T., De Zoysa, M., Asano, T. & Noda, S. Realization of dynamic thermal emission control. *Nat. Mater.* **13**, 928 (2014).

2. Coppens, Z. J. & Valentine, J. G. Spatial and temporal modulation of thermal emission. *Adv. Mater.* **29**, 1701275 (2017).

3. Beenakker, C. W. J. Thermal radiation and amplified spontaneous emission from a random medium. *Phys. Rev. Lett.* **81**, 1829 (1998).

4. Luo, C., Narayanaswamy, A., Chen, G. & Joannopoulos, J. D. Thermal radiation from photonic crystals: a direct calculation. *Phys. Rev. Lett.* **93**, 213905 (2004).

5. Vollmer, M. & Möllmann, K.-P. *Infrared thermal imaging: fundamentals, research and applications*. (John Wiley & Sons, 2017).

6. Mason, J. A., Smith, S. & Wasserman, D. Strong absorption and selective thermal emission from a midinfrared metamaterial. *Appl. Phys. Lett.* **98**, 241105 (2011).

7. Jung, D., Bank, S., Lee, M. L. & Wasserman, D. Next-generation mid-infrared sources. *J. Opt.* **19**, 123001 (2017).

8. Hulley, G. C. *et al.* High spatial resolution imaging of methane and other trace gases with the airborne Hyperspectral Thermal Emission Spectrometer (HyTES). *Atmos. Meas. Tech.* **9**, 2393–2408 (2016).

9. Gong, Y., Oh, S. S., Huffaker, D. L. & Copner, N. Novel Mid-Infrared Metamaterial Thermal Emitters for Optical Gas Sensing. in *Frontiers in Optics* JTu3A-89 (Optical Society of America, 2018).

10. Pan, Z. *et al.* Sensing properties of a novel temperature sensor based on field assisted thermal emission. *Sensors* **17**, 473 (2017).

11. Palchetti, L., Di Natale, G. & Bianchini, G. Remote sensing of cirrus cloud microphysical properties using spectral measurements over the full range of their thermal emission. *J. Geophys. Res. Atmos.* **121**, 10–804 (2016).

12. Costantini, D. *et al.* Plasmonic metasurface for directional and frequency-selective thermal emission. *Phys. Rev. Appl.* **4**, 14023 (2015).

13. Shen, Y., Hsu, C. W., Yeng, Y. X., Joannopoulos, J. D. & Soljačić, M. Broadband angular selectivity of light at the nanoscale: Progress, applications, and outlook. *Appl. Phys. Rev.* **3**, 11103 (2016).

14. Laroche, M. *et al.* Highly directional radiation generated by a tungsten thermal source. *Opt. Lett.* **30**, 2623–2625 (2005).

15. Wang, T. K. & Zemel, J. N. Polarized spectral emittance from periodic micromachined surfaces—III. Undoped silicon: the normal direction in shallow lamellar gratings. *Infrared Phys.* **32**, 477–488 (1991).

16. Hesketh, P. J., Zemel, J. N. & Gebhart, B. Organ pipe radiant modes of periodic micromachined silicon surfaces. *Nature* **324**, 549–551 (1986).

17. Hesketh, P. J., Zemel, J. N. & Gebhart, B. Polarized spectral emittance from periodic micromachined surfaces. II. Doped silicon: Angular variation. *Phys. Rev. B* **37**, 10803 (1988).

18. Greffet, J.-J. *et al.* Coherent emission of light by thermal sources. *Nature* **416**, 61 (2002).

19. Barbillon, G., Sakat, E., Hugonin, J.-P., Biehs, S.-A. & Ben-Abdallah, P. True thermal antenna with hyperbolic metamaterials. *Opt. Express* **25**, 23356–23363 (2017).

20. Lucchi, E. Applications of the infrared thermography in the energy audit of buildings: A review. *Renew. Sustain. Energy Rev.* **82**, 3077–3090 (2018).

21. Sakr, E. & Bermel, P. Thermophotovoltaics with spectral and angular selective doped-oxide thermal emitters. *Opt. Express* **25**, A880–A895 (2017).

22. Sakakibara, R. *et al.* Practical emitters for thermophotovoltaics: a review. *J. Photonics Energy* **9**, 32713 (2019).

23. Raman, A. P., Li, W. & Fan, S. Generating Light from Darkness. *Joule* (2019).

24. Raman, A. P., Anoma, M. A., Zhu, L., Rephaeli, E. & Fan, S. Passive radiative cooling below ambient air temperature under direct sunlight. *Nature* **515**, 540 (2014).

25. Yin, X., Yang, R., Tan, G. & Fan, S. Terrestrial radiative cooling: Using the cold universe as a renewable and sustainable energy source. *Science (80-.).* **370**, 786–791 (2020).

26. Shen, Y. *et al.* Optical broadband angular selectivity. *Science (80-.).* **343**, 1499–1501 (2014).

27. Qu, Y. *et al.* Polarization-Independent Optical Broadband Angular Selectivity. *Acs Photonics* **5**, 4125–4131 (2018).

28. Argyropoulos, C., Le, K. Q., Mattiucci, N., D'Aguanno, G. & Alu, A. Broadband absorbers and selective emitters based on plasmonic Brewster metasurfaces. *Phys. Rev. B* **87**, 205112 (2013).

29. Vulis, D. I., Reshef, O., Camayd-mu, P. & Mazur, E. Manipulating the flow of light using Dirac-cone zero-index metamaterials. (2019).

30. Liberal, I. & Engheta, N. The rise of near-zero-index technologies. *Science (80-.).* **358**, 1540–1541 (2017).

31. Rensberg, J. *et al.* Epsilon-near-zero substrate engineering for ultrathin-film perfect absorbers. *Phys. Rev. Appl.* **8**, 14009 (2017).

32. Yoon, J., Zhou, M., Badsha, A., Kim, T. Y. & Jun, Y. C. Broadband Epsilon-Near-Zero Perfect Absorption in the. *Nat. Publ. Gr.* 1–8 (2015). doi:10.1038/srep12788

33. Shaykhutdinov, T., Furchner, A., Rappich, J. & Hinrichs, K. Mid-infrared nanospectroscopy of Berreman mode and epsilon-near-zero local field confinement in thin

films. *Opt. Mater. Express* **7**, 3706 (2017).

34. Streyer, W. *et al.* Engineering absorption and blackbody radiation in the far-infrared with surface phonon polaritons on gallium phosphide. *Appl. Phys. Lett.* **104**, 131105 (2014).

35. Newman, W. D. *et al.* Ferrell–Berreman modes in plasmonic epsilon-near-zero media. *Acs Photonics* **2**, 2–7 (2015).

36. Badsha, A., Jun, Y. C. & Kwon, C. Admittance matching analysis of perfect absorption in unpatterned thin fi lms. *Opt. Commun.* **332**, 206–213 (2014).

37. Wang, Z., Zhou, P. & Zheng, G. Electrically switchable highly efficient epsilon-near-zero metasurfaces absorber with broadband response. *Results Phys.* **14**, 102376 (2019).

38. Krayer, L. J., Kim, J., Garrett, J. L. & Munday, J. N. Optoelectronic devices on index-near-zero substrates. *ACS Photonics* **6**, 2238–2244 (2019).

39. Guo, Y. *et al.* Tunable broadband, wide angle and lithography-free absorber in the near-infrared using an ultrathin VO 2 film. *Appl. Phys. Express* (2019).

40. Ane, J. M. & Huetz-Aubert, M. Stratified media theory interpretation of measurements of the spectral polarized directional emissivity of some oxidized metals. *Int. J. Thermophys.* **7**, 1191–1208 (1986).

41. Kischkat, J. *et al.* Mid-infrared optical properties of thin films of aluminum oxide, titanium dioxide, silicon dioxide, aluminum nitride, and silicon nitride. *Appl. Opt.* **51**, 6789–6798 (2012).

42. Hass, G. & Salzberg, C. D. Optical properties of silicon monoxide in the wavelength region from 0.24 to 14.0 microns. *JOSA* **44**, 181–187 (1954).

43. Bright, T. J. *et al.* Infrared optical properties of amorphous and nanocrystalline Ta 2O5 thin films. *J. Appl. Phys.* **114**, 1–10 (2013).

44. Hofmeister, A. M., Keppel, E. & Speck, A. K. Absorption and reflection infrared spectra of MgO and other diatomic compounds. *Mon. Not. R. Astron. Soc.* **345**, 16–38 (2003).

45. Liberal, I. & Engheta, N. Near-zero refractive index photonics. *Nat. Photonics* **11**, 149 (2017).

46. Liberal, I., Mahmoud, A. M., Li, Y., Edwards, B. & Engheta, N. Photonic doping of epsilon-near-zero media. *Science (80-.).* **355**, 1058–1062 (2017).

47. Horiuchi, N. Efficient thermophotovoltaics. *Nat. Photonics* **14**, 66 (2020).

48. Davids, P. S. *et al.* Electrical power generation from moderate-temperature radiative thermal sources. *Science (80-.).* **367**, 1341–1345 (2020).

49. Tredicucci, A. *et al.* Single-mode surface-plasmon laser. *Appl. Phys. Lett.* **76**, 2164–2166 (2000).

50. Marquier, F., Joulain, K., Mulet, J.-P., Carminati, R. & Greffet, J.-J. Engineering infrared emission properties of silicon in the near field and the far field. *Opt. Commun.* **237**, 379–

388 (2004).

51. Ginn, J. C., Jarecki Jr, R. L., Shaner, E. A. & Davids, P. S. Infrared plasmons on heavily-doped silicon. *J. Appl. Phys.* **110**, 43110 (2011).

52. Shahzad, M. *et al.* Infrared surface plasmons on heavily doped silicon. *J. Appl. Phys.* **110**, 123105 (2011).

53. Vassant, S. *et al.* Electrical modulation of emissivity. *Appl. Phys. Lett.* **102**, 81125 (2013).

54. Vassant, S. *et al.* Epsilon-near-zero mode for active optoelectronic devices. *Phys. Rev. Lett.* **109**, 237401 (2012).

55. Liu, R. *et al.* Mid-infrared emission from In (Ga) Sb layers on InAs (Sb). *Opt. Express* **22**, 24466–24477 (2014).

56. Dong, Z. *et al.* Electrical modulation of degenerate semiconductor plasmonic interfaces. *J. Appl. Phys.* **126**, (2019).

57. Park, J. *et al.* Dynamic thermal emission control with InAs-based plasmonic metasurfaces. *Sci. Adv.* **4**, 1–8 (2018).

58. Dunkelberger, A. D. *et al.* Ultrafast Active Tuning of the Berreman Mode. *ACS Photonics* **7**, 279–287 (2020).

59. Naik, G. V, Kim, J. & Boltasseva, A. Oxides and nitrides as alternative plasmonic materials in the optical range. *Opt. Mater. Express* **1**, 1090–1099 (2011).

60. Law, S., Adams, D. C., Taylor, A. M. & Wasserman, D. Mid-infrared designer metals. *2012 IEEE Photonics Conf. IPC 2012* **20**, 786–787 (2012).

61. Cho, A. Y. & Arthur, J. R. Molecular beam epitaxy. *Prog. solid state Chem.* **10**, 157–191 (1975).

62. Cho, A. Y. Film deposition by molecular-beam techniques. *J. Vac. Sci. Technol.* **8**, S31–S38 (1971).

63. Herman, M. A. & Sitter, H. *Molecular beam epitaxy: fundamentals and current status*. **7**, (Springer Science & Business Media, 2012).

64. Joannopoulos, J. D., Johnson, S. G., Winn, J. N. & Meade, R. D. Molding the flow of light. *Princet. Univ. Press. Princeton, NJ [ua]* (2008).

65. Raman, A. & Fan, S. Photonic band structure of dispersive metamaterials formulated as a Hermitian eigenvalue problem. *Phys. Rev. Lett.* **104**, 87401 (2010).

66. Fan, S. & Joannopoulos, J. D. Analysis of guided resonances in photonic crystal slabs. *Phys. Rev. B* **65**, 235112 (2002).

67. Karabchevsky, A., Katiyi, A., Ang, A. S. & Hazan, A. On-chip nanophotonics and future challenges. *Nanophotonics* **9**, 3733–3753 (2020).

68. Zhang, T. *et al.* A review of photonic crystal fiber sensor applications for different physical

quantities. *Appl. Spectrosc. Rev.* **53**, 486–502 (2018).

69. Dutta, H. S., Goyal, A. K., Srivastava, V. & Pal, S. Coupling light in photonic crystal waveguides: A review. *Photonics Nanostructures-Fundamentals Appl.* **20**, 41–58 (2016).

70. Pinto, A. M. R. & Lopez-Amo, M. Photonic crystal fibers for sensing applications. *J. Sensors* **2012**, (2012).

71. Soukoulis, C. M. *Photonic crystals and light localization in the 21st century*. **563**, (Springer Science & Business Media, 2012).

72. Johnson, S. G. *et al.* Perturbation theory for Maxwell's equations with shifting material boundaries. *Phys. Rev. E* **65**, 66611 (2002).

73. Takata, K. *et al.* Observing exceptional point degeneracy of radiation with electrically pumped photonic crystal coupled-nanocavity lasers. *Optica* **8**, 184–192 (2021).

74. Hodaei, H., Miri, M.-A., Heinrich, M., Christodoulides, D. N. & Khajavikhan, M. Parity-time–symmetric microring lasers. *Science (80-.).* **346**, 975–978 (2014).

75. Feng, L., El-Ganainy, R. & Ge, L. Non-Hermitian photonics based on parity–time symmetry. *Nat. Photonics* **11**, 752–762 (2017).

76. Longhi, S. Parity-time symmetry meets photonics: A new twist in non-Hermitian optics. *EPL (Europhysics Lett.* **120**, 64001 (2018).

77. Robinson, A. J. A thermal model for energy loss through walls behind radiators. *Energy Build.* **127**, 370–381 (2016).

78. Shortall, R., Davidsdottir, B. & Axelsson, G. A sustainability assessment framework for geothermal energy projects: Development in Iceland, New Zealand and Kenya. *Renew. Sustain. Energy Rev.* **50**, 372–407 (2015).

79. Yu, Z., Haghighat, F., Fung, B. C. M. & Yoshino, H. A decision tree method for building energy demand modeling. *Energy Build.* **42**, 1637–1646 (2010).

80. Lodwick, W. A. & David Jamison, K. A Constraint Fuzzy Interval Analysis approach to fuzzy optimization. *Inf. Sci. (Ny).* **426**, 38–49 (2018).

81. Chimklai, P., Hagishima, A. & Tanimoto, J. A computer system to support Albedo Calculation in urban areas. *Build. Environ.* **39**, 1213–1221 (2004).

82. Zhang, Q., Hu, S. & Chen, D. A comparison between coal-to-olefins and oil-based ethylene in China: An economic and environmental prospective. *J. Clean. Prod.* **165**, 1351–1360 (2017).

83. Burman, E., Hong, S. M., Paterson, G., Kimpian, J. & Mumovic, D. A comparative study of benchmarking approaches for non-domestic buildings: Part 2 – Bottom-up approach. *Int. J. Sustain. Built Environ.* **3**, 247–261 (2014).

84. Alison, L. *et al.* 3D printing of sacrificial templates into hierarchical porous materials. *Sci. Rep.* **9**, (2019).

85. Deng, B., Zhang, Y. & Long, F. A superficial density method to describe the diffuser boundary condition in CFD simulation of indoor airflow. *Build. Environ.* **135**, 280–285 (2018).

86. Delgado, A. & Herzog, H. J. A simple model to help understand water use at power plants. *Work. Pap.* 1–21 (2012).

87. Deb, C., Zhang, F., Yang, J., Lee, S. E. & Shah, K. W. A review on time series forecasting techniques for building energy consumption. *Renew. Sustain. Energy Rev.* **74**, 902–924 (2017).

88. Angelakoglou, K. & Gaidajis, G. A review of methods contributing to the assessment of the environmental sustainability of industrial systems. *J. Clean. Prod.* **108**, 725–747 (2015).

89. Martín-Gamboa, M., Iribarren, D., García-Gusano, D. & Dufour, J. A review of life-cycle approaches coupled with data envelopment analysis within multi-criteria decision analysis for sustainability assessment of energy systems. *J. Clean. Prod.* **150**, 164–174 (2017).

90. Zhang, Y., Zhao, Y. & Lv, R. A review for optical sensors based on photonic crystal cavities. *Sensors Actuators A Phys.* **233**, 374–389 (2015).

91. Mu, E. *et al.* A novel self-powering ultrathin TEG device based on micro/nano emitter for radiative cooling. *NANO ENERGY* **55**, 494–500 (2019).

92. Li, T. A Life Cycle Approach to Sustainability Assessment on Community Energy Projects in the UK. 1–12 (2016).

93. Feng, L., Wong, Z. J., Ma, R.-M., Wang, Y. & Zhang, X. Single-mode laser by parity-time symmetry breaking. *Science (80-.).* **346**, 972–975 (2014).

94. Zhao, H. *et al.* Metawaveguide for asymmetric interferometric light-light switching. *Phys. Rev. Lett.* **117**, 193901 (2016).

95. Xu, Y.-L. *et al.* Experimental realization of Bloch oscillations in a parity-time synthetic silicon photonic lattice. *Nat. Commun.* **7**, 1–6 (2016).

96. Lawrence, M. *et al.* Manifestation of P T Symmetry Breaking in Polarization Space with Terahertz Metasurfaces. *Phys. Rev. Lett.* **113**, 93901 (2014).

97. Peng, B. *et al.* Parity–time-symmetric whispering-gallery microcavities. *Nat. Phys.* **10**, 394–398 (2014).

98. Guo, A. *et al.* Observation of P T-symmetry breaking in complex optical potentials. *Phys. Rev. Lett.* **103**, 93902 (2009).

99. Regensburger, A. *et al.* Parity–time synthetic photonic lattices. *Nature* **488**, 167–171 (2012).

100. Wen, J. *et al.* Experimental demonstration of a digital quantum simulation of a general PT-symmetric system. *Phys. Rev. A* **99**, 62122 (2019).

101. Kremer, M., Biesenthal, T., Heinrich, M., Thomale, R. & Szameit, A. Demonstration of a two-dimensional PT-symmetric crystal: bulk dynamics, topology, and edge states. *arXiv*

Prepr. arXiv1809.00041 (2018).

102. Biesenthal, T., Kremer, M., Heinrich, M. & Szameit, A. Experimental Realization of P T-Symmetric Flat Bands. *Phys. Rev. Lett.* **123**, 183601 (2019).

103. Huang, K. C. *et al.* Nature of lossy Bloch states in polaritonic photonic crystals. *Phys. Rev. B* **69**, 195111 (2004).

104. Davanço, M., Urzhumov, Y. & Shvets, G. The complex Bloch bands of a 2D plasmonic crystal displaying isotropic negative refraction. *Opt. Express* **15**, 9681–9691 (2007).

105. Naito, T., Sakai, O. & Tachibana, K. Experimental verification of complex dispersion relation in lossy photonic crystals. *Appl. Phys. express* **1**, 66003 (2008).

106. Lucarini, V., Saarinen, J. J., Peiponen, K.-E. & Vartiainen, E. M. *Kramers-Kronig relations in optical materials research*. **110**, (Springer Science & Business Media, 2005).

107. Zollner, S., Lin, C., Schönherr, E., Böhringer, A. & Cardona, M. The dielectric function of AlSb from 1.4 to 5.8 eV determined by spectroscopic ellipsometry. *J. Appl. Phys.* **66**, 383–387 (1989).

108. Aspnes, D. E. & Studna, A. A. Dielectric functions and optical parameters of si, ge, gap, gaas, gasb, inp, inas, and insb from 1.5 to 6.0 ev. *Phys. Rev. B* **27**, 985 (1983).

109. Threm, D., Nazirizadeh, Y. & Gerken, M. Photonic crystal biosensors towards on-chip integration. *J. Biophotonics* **5**, 601–616 (2012).

110. Bock, W. J., Gannot, I. & Tanev, S. *Optical waveguide sensing and imaging*. (Springer Science & Business Media, 2007).

111. Nair, R. V & Vijaya, R. Photonic crystal sensors: An overview. *Prog. Quantum Electron.* **34**, 89–134 (2010).

112. Pitruzzello, G. & Krauss, T. F. Photonic crystal resonances for sensing and imaging. *J. Opt.* **20**, 73004 (2018).

113. Griffiths, D. J. & Schroeter, D. F. *Introduction to quantum mechanics*. (Cambridge University Press, 2018).

114. Zhuo, Y. & Cunningham, B. T. Label-free biosensor imaging on photonic crystal surfaces. *Sensors* **15**, 21613–21635 (2015).

115. Kingma, B. & van Marken Lichtenbelt, W. Energy consumption in buildings and female thermal demand. *Nat. Clim. Chang.* **5**, 1054–1056 (2015).

116. Pérez-Lombard, L., Ortiz, J. & Pout, C. A review on buildings energy consumption information. *Energy Build.* **40**, 394–398 (2008).

117. The heat is on. *Nat. Energy* **1**, 16193 (2016).

118. Ürge-Vorsatz, D., Cabeza, L. F., Serrano, S., Barreneche, C. & Petrichenko, K. Heating and cooling energy trends and drivers in buildings. *Renew. Sustain. Energy Rev.* **41**, 85–98 (2015).

119. FANGER, P. O. *Thermal comfort. Analysis and applications in environmental engineering.* (Copenhagen: Danish Technical Press., 1970).

120. Hensen, J. L. M. Literature review on thermal comfort in transient conditions. *Build. Environ.* **25**, 309–316 (1990).

121. Moon, J. H., Lee, J. W., Jeong, C. H. & Lee, S. H. Thermal comfort analysis in a passenger compartment considering the solar radiation effect. *Int. J. Therm. Sci.* **107**, 77–88 (2016).

122. Cheng, Y., Niu, J., Liu, X. & Gao, N. Experimental and numerical investigations on stratified air distribution systems with special configuration: Thermal comfort and energy saving. *Energy Build.* **64**, 154–161 (2013).

123. Liu, Y., Wang, L., Liu, J. & Di, Y. A study of human skin and surface temperatures in stable and unstable thermal environments. *J. Therm. Biol.* **38**, 440–448 (2013).

124. Liu, W., Lian, Z., Deng, Q. & Liu, Y. Evaluation of calculation methods of mean skin temperature for use in thermal comfort study. *Build. Environ.* **46**, 478–488 (2011).

125. ANSI/ASHRAE. *ASHRAE Handbook—Fundamentals*. (2017).

126. Okamoto, T., Tamura, K., Miyamoto, N., Tanaka, S. & Futaeda, T. Physiological activity in calm thermal indoor environments. *Sci. Rep.* **7**, 11519 (2017).

127. Coutts, A. M., White, E. C., Tapper, N. J., Beringer, J. & Livesley, S. J. Temperature and human thermal comfort effects of street trees across three contrasting street canyon environments. *Theor. Appl. Climatol.* **124**, 55–68 (2016).

128. Yang, L., Yan, H. & Lam, J. C. Thermal comfort and building energy consumption implications – A review. *Appl. Energy* **115**, 164–173 (2014).

129. Rupp, R. F., Vásquez, N. G. & Lamberts, R. A review of human thermal comfort in the built environment. *Energy Build.* **105**, 178–205 (2015).

130. Hoyt, T., Lee, K. H., Zhang, H., Arens, E. & Webster, T. Energy savings from extended air temperature setpoints and reductions in room air mixing. (2005).

131. Arslanoglu, N. & Yigit, A. Experimental and theoretical investigation of the effect of radiation heat flux on human thermal comfort. *Energy Build.* **113**, 23–29 (2016).

132. Teitelbaum, E. *et al.* Membrane-assisted radiant cooling for expanding thermal comfort zones globally without air conditioning. *Proc. Natl. Acad. Sci.* **117**, 21162–21169 (2020).

133. Schiavoni, S., Bianchi, F. & Asdrubali, F. Insulation materials for the building sector: A review and comparative analysis. *Renew. Sustain. Energy Rev.* **62**, 988–1011 (2016).

134. Wang, H. *et al.* Application of wall and insulation materials on Green building: A review. *Sustainability* **10**, 3331 (2018).

135. Dickson, T. & Pavía, S. Energy performance, environmental impact and cost of a range of insulation materials. *Renew. Sustain. Energy Rev.* **140**, 110752 (2021).

136. Cai, L. *et al.* Warming up human body by nanoporous metallized polyethylene textile. *Nat.*

Commun. **8**, 496 (2017).

137. Winslow, C.-E., Gagge, Ap. & Herrington, L. P. The influence of air movement upon heat losses from the clothed human body. *Am. J. Physiol. Content* **127**, 505–518 (1939).

138. Qiu, Q. *et al.* Highly flexible, breathable, tailorable and washable power generation fabrics for wearable electronics. *Nano Energy* **58**, 750–758 (2019).

139. Cai, L. *et al.* Temperature Regulation in Colored Infrared-Transparent Polyethylene Textiles. *Joule* (2019).

140. Zhou, H. *et al.* Fabrication of flexible and superhydrophobic melamine sponge with aligned copper nanoparticle coating for self-cleaning and dual thermal management properties. *Ind. Eng. Chem. Res.* (2019).

141. Yue, X. *et al.* Ag nanoparticles coated cellulose membrane with high infrared reflection, breathability and antibacterial property for human thermal insulation. *J. Colloid Interface Sci.* **535**, 363–370 (2019).

142. Hsu, P.-C. *et al.* Radiative human body cooling by nanoporous polyethylene textile. *Science (80-.).* **353**, 1019 LP – 1023 (2016).

143. Guo, Y. *et al.* Fluoroalkylsilane-Modified Textile-Based Personal Energy Management Device for Multifunctional Wearable Applications. *ACS Appl. Mater. Interfaces* **8**, 4676–4683 (2016).

144. Hsu, P.-C. *et al.* Personal Thermal Management by Metallic Nanowire-Coated Textile. *Nano Lett.* **15**, 365–371 (2015).

145. Tong, J. K. *et al.* Infrared-Transparent Visible-Opaque Fabrics for Wearable Personal Thermal Management. *ACS Photonics* **2**, 769–778 (2015).

146. Robinson, A. J. A thermal model for energy loss through walls behind radiators. *Energy Build.* **127**, 370–381 (2016).

147. Mulford, R. B., Dwivedi, V. H., Jones, M. R. & Iverson, B. D. Control of Net Radiative Heat Transfer With a Variable-Emissivity Accordion Tessellation. *J. Heat Transfer* **141**, 32702 (2019).

148. Zhang, X. *et al.* Preparation and performances of all-solid-state variable infrared emittance devices based on amorphous and crystalline WO3 electrochromic thin films. *Sol. Energy Mater. Sol. Cells* **200**, 109916 (2019).

149. Brooke, R. *et al.* Infrared electrochromic conducting polymer devices. *J. Mater. Chem. C* **5**, 5824–5830 (2017).

150. Zhang, L. *et al.* Further understanding of the mechanisms of electrochromic devices with variable infrared emissivity based on polyaniline conducting polymers. *J. Mater. Chem. C* **7**, 9878–9891 (2019).

151. Xu, J. W. *et al. Electrochromic Smart Materials: Fabrication and Applications*. (Royal Society of Chemistry, 2019).

152. Kant, K., Shukla, A., Sharma, A. & Sharma, A. Advances in simulation studies for developing energy-efficient buildings. *Sustain. through energy-efficient Build.* 209–233 (2018).

153. Yu, Y., Megri, A. C. & Jiang, S. A review of the development of airflow models used in building load calculation and energy simulation. in *Building Simulation* **12**, 347–363 (Springer, 2019).

154. Shen, P., Dai, M., Xu, P. & Dong, W. Building heating and cooling load under different neighbourhood forms: Assessing the effect of external convective heat transfer. *Energy* **173**, 75–91 (2019).

155. Defraeye, T., Blocken, B. & Carmeliet, J. Convective heat transfer coefficients for exterior building surfaces: Existing correlations and CFD modelling. *Energy Convers. Manag.* **52**, 512–522 (2011).

156. Wijeysundera, N. E. *Principles of heating, ventilation and air conditioning with Worked Examples*. (World Scientific, 2015).

157. Chafi, F. Z. & Hallé, S. Three dimensional study for evaluating of air flow movements and thermal comfort in a model room: Experimental validation. *Energy Build.* **43**, 2156–2166 (2011).

158. Takada, S., Sasaki, A. & Kimura, R. Fundamental study of ventilation in air layer in clothing considering real shape of the human body based on CFD analysis. *Build. Environ.* **99**, 210–220 (2016).

159. Oğulata, R. T. The effect of thermal insulation of clothing on human thermal comfort. *Fibres Text. East. Eur.* **15**, 61 (2007).

160. Lienhard, J. H. *A heat transfer textbook*. (Courier Corporation, 2011).

161. ASHRAE, A. H. Fundamentals, SI ed., American Society of Heating Refrigeration and Air-conditioning Engineers. *Inc., USA* (2013).

162. Hasan, M. H., Alsaleem, F. & Rafaie, M. Sensitivity study for the PMV thermal comfort model and the use of wearable devices biometric data for metabolic rate estimation. *Build. Environ.* **110**, 173–183 (2016).

163. Pourshaghaghy, A. & Omidvari, M. Examination of thermal comfort in a hospital using PMV–PPD model. *Appl. Ergon.* **43**, 1089–1095 (2012).

164. ANSI/ASHRAE. Thermal Environmental Conditions for Human Occupancy Standard 55-2013. *Ashrae ASHRAE Stand. 55* (2013).

165. Fumo, N., Mago, P. & Luck, R. Methodology to estimate building energy consumption using EnergyPlus Benchmark Models. *Energy and Buildings* **42**, 2331–2337 (2010).

166. Commercial reference buildings. Available at: https://www.energy.gov/eere/buildings/commercial-reference-buildings. (2008).

167. Stazi, F., Vegliò, A., Di Perna, C. & Munafò, P. Experimental comparison between 3

different traditional wall constructions and dynamic simulations to identify optimal thermal insulation strategies. *Energy Build.* **60**, 429–441 (2013).